

ABSTRACT

ALKUHAYLI, ABDULAZIZ ABDULLAH G. Control and Utilization of PV Inverters in Distributed Generation for Reactive Power Management and Voltage Regulation. (Under the direction of Dr. Iqbal Husain).

Supplying loads directly from renewable distributed energy resources (DERs), such as photovoltaic (PV), contributes to clean energy and releases the power system's capacity. Nevertheless, PV resources are highly variable and non-dispatchable in the current power system infrastructure. In addition, the PV resource production profile does not follow the demand profile, which results in more bidirectional power flow between distribution networks and the main grid. To gain the most benefits from integrating PV, developing the controller algorithm should take into account the network limitations and provide some features such as active power curtailment, reactive power control, and the capability to ride through voltage or frequency disturbances.

Fast and accurate synchronization of power electronics interfaced distributed generation (DG) to the grid or a microgrid is an important step in the management and utilization of the DERs. Several synchronization algorithms have been proposed to improve the phase tracking of the grid voltage. However, when the grid is weak or distorted, the synchronization process may suffer from poor frequency regulation. Therefore, Sliding Discrete Fourier Transform Phase-locked-loop (SDFT-PLL) algorithm has been developed to extract an accurate phase angle of the fundamental voltage while rejecting the harmonics in a distorted or weak grid. The SDFT-PLL algorithm and simulation results to validate this method are presented.

High levels of PV penetration is accompanied by voltage violations and reverse power flow, especially in residential distribution networks where the PV's maximum output power tends to occur before the peak time in a typical load profile. In this research, a Volt/Var control

strategy in distribution networks with high PV penetration considering inverter thermal model is presented. This strategy considers a central distribution control to schedule active power and reactive power to deal with solar power generation intermittency. The objective is to provide voltage regulation control while solving for optimal power flow to minimize both distribution system losses and inverter losses. Simulation results verify the effectiveness of the proposed strategy in regulating voltage within limits while allowing optimal reactive power allocation among distributed generation (DG) units to relieve the stress on some inverters especially those at the end of the feeder. An estimation of power loss considering the junction temperature of power devices can be applied directly to assess the lifetime of these PV inverters using the rainflow algorithm.

The distribution network control needs to manage the intermittent changes in PV power production. This research investigates the effectiveness of combining local and central schemes in distribution networks. Using minimum communication, the distribution system operator (DSO) collects loads and DGs measurements every hour to optimize reactive power set-point of DG units to keep voltages within allowable limits. In addition, the central control uses a scenario-based approach to optimize local control parameters. This proposed strategy considers the uncertainty related to PV systems, and has been applied to a radial distribution feeder with high PV penetration.

At a high penetration level of distributed PV, a portion of the conventional generation would be displaced, resulting in the loss of the main sources of dynamic reactive power in the transmission networks. Consequently, power systems may become more vulnerable to voltage instability events. This research focuses on long-term voltage stability assessment and enhancement in power systems with a high penetration of distributed PVs. Distributed PVs,

when properly controlled, can provide ancillary services that are traditionally delivered by spinning generators and voltage regulators to support the bulk power system. A case study is presented that provide dynamic reactive power reserves by distributed PV units to support the bulk power system.

© Copyright 2018 Abdulaziz Alkuhayli

All Rights Reserved

Control and Utilization of PV Inverters in Distributed Generation for Reactive Power
Management and Voltage Regulation

by
Abdulaziz Abdullah G Alkuhayli

A dissertation submitted to the Graduate Faculty of
North Carolina State University
in partial fulfillment of the
requirements for the degree of
Doctor of Philosophy

Electrical Engineering

Raleigh, North Carolina
2018

APPROVED BY:

Dr. Iqbal Husain
Committee Chair

Dr. Mesut Baran

Dr. Ning Lu

Dr. Tarek Echehki

DEDICATION

Dedicated to my family. Thank you for all your support and encouragement.

BIOGRAPHY

Abdulaziz Alkuhayli received his bachelor's degree in Electrical Engineering from King Saud University, Riyadh, Saudi Arabia in 2006. He joined Saudi Electricity Company in 2006 as an operating engineer at the national control center. In 2009, he joined King Saud University as a teaching assistance. He received his master's degree in Electrical Engineering from Missouri University of Science and Technology, Rolla, Missouri, in 2013. He received his Ph.D. degree from the Department of Electrical and Computer Engineering at North Carolina State University, Raleigh, NC in 2018.

ACKNOWLEDGMENTS

I would like to express my sincere gratitude to my advisor, Dr. Iqbal Husain, for his guidance, and encouragement throughout my doctoral studies and for giving me the opportunity to work with him.

Special thanks to my committee members Dr. Mesut Baran, Dr. Tarek Echehki, and Dr. Ning Lu for their time and considering being on my supervisory committee.

I would like to express my gratitude to all friends at NC State who have been helpful and have encouraged me during this period.

I would like to thank King Saud University for sponsoring me and giving me the opportunity to complete my study in the US.

Lastly, my deepest and most gratitude goes to my wife and my children who have always been supportive and patient during this period. This work would not have been possible without your companionship and encouragement.

TABLE OF CONTENTS

LIST OF TABLES	vii
LIST OF FIGURES	viii
1 Introduction.....	1
1.1 Overview	1
1.2 Motivation	1
1.3 Research Objectives	7
1.4 Dissertation Outline	8
2 PV Inverter Control and Reliability	11
2.1 PV Inverter Control	11
2.1.1 PV Inverter Architectures	12
2.1.2 Inverter Topology	13
2.1.3 Inverter Control	14
2.2 PV Inverter Reliability.....	22
2.2.1 Cycle Counting.....	28
2.3 Simulation Results.....	33
2.4 Conclusion.....	39
3 Distributed Generation Synchronization with a Distorted or Weak Grid	40
3.1 Introduction	40
3.2 Phase-Locked Loop Technique	42
3.3 Sliding Discrete Fourier Transform Phase-Locked-Loop	45
3.4 Simulation Results.....	49
3.5 Contribution.....	57
3.6 Conclusion.....	57
4 Volt/Var Control in Distribution Networks Considering Inverter Utilization	59
4.1 Introduction	59
4.2 System Model.....	64
4.2.1 Distribution Network Model	64
4.2.2 Distributed PV Model.....	66
4.3 Control Strategy.....	67
4.4 Simulation Results.....	70
4.4.1 Volt/Var Control Results.....	70
4.4.2 Reliability Analysis	76
4.5 Contribution.....	78
4.6 Conclusion.....	78
5 Reactive Power Management in Distribution Networks with Intermittent Renewables	80
5.1 Introduction	80

5.2	System Operation and Control	83
5.2.1	Local Control.....	84
5.2.2	Centralized Control.....	86
5.3	Voltage Sensitivity Analysis	87
5.4	Stochastic Optimization.....	89
5.4.1	PV Stochastic Model	89
5.4.2	Scenario Reduction.....	90
5.4.3	Stochastic Optimization.....	91
5.5	Case Study	93
5.5.1	Volt/Var Control Results	94
5.5.2	Reliability Analysis	102
5.6	Contribution.....	104
5.7	Conclusion.....	104
6	Reactive Power Reserves Management by DGs for Voltage Stability Enhancement: A Case Study.....	106
6.1	Introduction	106
6.2	Voltage Stability Assessment.....	108
6.2.1	Static Voltage Stability Analysis.....	109
6.2.2	Dynamic Voltage Stability Analysis	112
6.3	Models in Voltage Stability Analysis.....	113
6.3.1	Generator Model.....	113
6.3.2	PV Model.....	113
6.3.3	Excitation System Model.....	116
6.3.4	Transformer On-load Tap Changer Model	117
6.3.5	Load Model.....	117
6.4	Grid Control Architecture.....	118
6.5	Case Study	120
6.5.1	Q-V Curve Simulation.....	120
6.5.2	Dynamic Simulation	124
6.6	Conclusion.....	128
7	Summary and Future Work	130
7.1	Summary.....	130
7.2	Future Work.....	132
	REFERENCES.....	134

LIST OF TABLES

Table 1.1	Cycle information from the rainflow counting algorithm applied to the temperature profile in Fig. 2.15	31
Table 2.2	Electrical and thermal parameters of the inverter	33
Table 3.1	System parameters	50
Table 3.2	Performance comparison between the SRF-PLL and SDFT-PLL.....	56
Table 4.1	Average daily losses of feeder and PV inverters	75
Table 5.1	Energy losses of PV inverters and feeder, and maximum voltage violation	102
Table 6.1	PV Generation Data for 10% Penetration.....	123
Table 6.2	Reactive Power Margin at Bus 1042	123

LIST OF FIGURES

Figure 1.1	Block diagram of multilevel control structure for DG	3
Figure 1.2	The impact of high level of PV penetration on feeder voltage profile under low load condition	4
Figure 1.3	A graphic representation of the research aspects in this study	8
Figure 2.1	The impact of high level of PV penetration on feeder voltage profile under low load condition	11
Figure 2.2	Micro inverter architecture	12
Figure 2.3	String inverter architecture	13
Figure 2.4	Grid-tied three-phase VSI inverter	14
Figure 2.5	Graphic representations of a dq transformation: (a) balanced three-phase voltages, (b) voltages in a $\alpha\text{-}\beta$ coordinate, and (c) voltages in a $d\text{-}q$ coordinate	17
Figure 2.6	Power stage of the VSI	19
Figure 2.7	Block diagram of a dq current controller.....	21
Figure 2.8	Scheme of a current-controlled inverter in the synchronous reference frame	21
Figure 2.9	Cross-sectional structure of a conventional IGBT.....	23
Figure 2.10	Thermal model of a power semiconductor device.....	25
Figure 2.11	Typical performance characteristics of an IGBT [57]	27
Figure 2.12	Temperature profile and the corresponding closed stress-strain hysteresis loops.....	30
Figure 2.13	Temperature profile	30
Figure 2.14	Rainflow cycles extracted from the temperature profile in Fig. 2.13	31
Figure 2.15	Reliability analysis of a power electronic devices flowchart	32
Figure 2.16	Lookup table of the IGBT device thermal performance with active and reactive Power supplies at $T_a= 25^\circ\text{C}$: (a) total losses, and (b) junction temperature	35
Figure 2.17	Yearly mission profiles (15 min per sample): (a) solar irradiance, and (b) ambient temperature	36

Figure 2.18	Yearly profiles from the thermal model of the IGBT device in a PV inverter: (a) power loss, and (b) junction temperature	37
Figure 2.19	Rainflow counting of the junction temperature profile	38
Figure 3.1	Grid-connected microgrid and the control overview	43
Figure 3.2	Synchronous reference frame PLL	44
Figure 3.3	SDFT filter structure	46
Figure 3.4	Window signal sampling for a 10-point SDFT	47
Figure 3.5	Frequency response of the SDFT filter for $N=18$	47
Figure 3.6	SDFT filter for fundamental component extraction	48
Figure 3.7	Pole-zero plot for the SDFT filter for $k=1$, $N=18$	49
Figure 3.8	Voltage signal before and after harmonic elimination by the SDFT filter	50
Figure 3.9	Dynamic performance of the SDFT-PLL	51
Figure 3.10	Dynamic performance of the SRF-PLL	52
Figure 3.11	Simulation results for the harmonic elimination effect on the frequency and phase error estimation (SDFT prefilter, enabled at $t = 0.6$)	53
Figure 3.12	Harmonic components of the phase error for the SRF-PLL	53
Figure 3.13	Simple distribution feeder with fault at node F	54
Figure 3.14	Voltage at the PCC with the grid in fault condition (fault applied at $t= 1.2$ s and cleared at $t= 1.4$ s)	54
Figure 3.15	Frequency and phase error estimation from the SDFT-PLL in the fault condition	55
Figure 3.16	Frequency and phase error estimation from the SRF-PLL in the fault condition	56
Figure 4.1	Schematic diagram of a radial distribution feeder with n nodes	65
Figure 4.2	PV Inverter capability curve	66
Figure 4.3	Volt/Var control strategy in a distribution network	68
Figure 4.4	18-node test system	70

Figure 4.5	Scaled load profile (15 minute per sample)	71
Figure 4.6	Voltage profile of node 18	73
Figure 4.7	Modified boxplot for the reactive power support by PV inverter for different control methods. The whiskers are extended to cover the minimum and maximum values	74
Figure 4.8	Modified boxplot for the junction temperature (T_j) of IGBT devices in PV inverters for different control methods	75
Figure 4.9	Temperature cycle-counting results from the rainflow algorithm for IGBT devices in PV inverters at node 2 for Cases 2 and 3: (a) mean junction temperature (T_m), and (b) junction temperature cycle amplitude (ΔT_j)	76
Figure 4.10	Accumulated damage of IGBT devices in PV inverters for different control methods (cases).....	77
Figure 5.1	Distribution control architecture.....	84
Figure 5.2	V-Q control characteristic.....	85
Figure 5.3	Current control block diagram for reactive power control	85
Figure 5.4	Schematic diagram of a distribution feeder	88
Figure 5.5	Flowchart of optimal local control parameters	92
Figure 5.6	Scaled PV active profile (1 minute per sample)	93
Figure 5.7	Ambient temperature profile (1 minute per sample)	94
Figure 5.8	Scaled load profile (1 minute per sample).....	94
Figure 5.9	Voltage profile at node 18 (Case 1).....	95
Figure 5.10	Empirical CDF curves of the voltage at node 18 for different control methods	96
Figure 5.11	Voltage profile at node 18 (Case 2).....	97
Figure 5.12	Voltage profile at node 18 (Case 3).....	97
Figure 5.13	Voltage profile at node 18 (Case 4).....	98
Figure 5.14	Modified box plot for the reactive power support by the PV inverter for different control methods.....	99
Figure 5.15	Modified box plot for the junction temperature (T_j) of IGBT devices in PV inverters for different control methods	101

Figure 5.16	Accumulated damage of IGBT devices in PV inverters for different control methods.....	103
Figure 6.1	Time response of acting equipment in major disturbances [148].....	110
Figure 6.2	A simple power system.....	111
Figure 6.3	Q-V curves for the base case and $N-1$ contingency.....	112
Figure 6.4	WECC-recommended representation of a high penetration of PV units in bulk power system studies [144].....	114
Figure 6.5	PV model diagram in PSS/E [143].....	114
Figure 6.6	Converter control module (PVEU) diagram in PSS/E [143].....	115
Figure 6.7	Converter module (PVGU) diagram in PSS/E [143].....	116
Figure 6.8	Voltage stability assessment flowchart.....	119
Figure 6.9	Modified Nordic test system.....	121
Figure 6.10	Q-V curves at Bus 1042.....	122
Figure 6.11	Case 1: Voltage at Buses 2 and 1042.....	124
Figure 6.12	Case 2: Voltage at Buses 2 and 1042.....	125
Figure 6.13	Case 2: Field current of G7 and G15.....	126
Figure 6.14	Case 3: Voltage at Buses 2 and 1042.....	127
Figure 6.15	Case 3: Reactive power produced by PV302 (System base: 100 MVA).....	127
Figure 6.16	Case 3: Field current of G7 and G15.....	128

1 Introduction

1.1 Overview

As the capacity of distributed energy resources (DERs) continues to grow to replace conventional centralized generation, technical and operating challenges are expected to increase in both local and bulk power systems. Supplying loads directly from distributed resources, such as solar photovoltaic (PV), will contribute to clean energy and expand the capacity of the power system. However, PV resources are highly variable and non-dispatchable in the current power system infrastructure. In addition, the PV resource production profile does not follow the demand profile, resulting in more bidirectional power between the distribution network and the main grid. Therefore, the transformation towards distributed PV sources in power systems must be evaluated, and systems planners must identify these challenges to ensure system reliability with a high penetration of PVs.

1.2 Motivation

Grid integration of solar PV has become a major area of interest for researchers in power systems engineering. This interest is driven by the rapid advance and cost reduction of power electronics and solar PV panels [1]. In addition, generating electricity using renewable energy resources allows for a reduction in greenhouse gas emissions. While the main goal of using PV energy is to generate active power, researchers have proposed different applications for PV, especially to support grid stability [2]–[4]. The integration of PV can provide ancillary services to support secure and cost-efficient operation.

High level of PV deployment in real power systems is relatively new making it difficult to identify all of the challenges it would face. However, researchers and planners in the field of power systems have analyzed the anticipated impacts of distributed PV on transmission and distribution systems [5]. To investigate the effect of high PV penetration on that power system, the following operating challenges were identified from a system operator's perspective:

- Aggregated load and PV forecast availability.
- Communication channels and central control availability.
- Coordination between aggregated PV generation and centralized power plants within the grid.
- Flexible Volt/Var control availability.
- Coordination between systems elements during restoration.
- Adaptive protection settings to accommodate PV generation.
- Ability to ride through voltage and frequency disturbances.
- Creation of a spinning reserve adequacy evaluation.

Some of the distributed PVs with a larger capacity will be connected to medium (i.e., utility-scale) voltage feeders. However, a large portion will be installed behind the meter (residential rooftop) where power system operators have no access to control these PVs [6]. High penetration of rooftop PV units in the distribution networks would lead to decentralization of the power grid and make the distribution network more vulnerable to challenging operational issues such as voltage-sag, overvoltage, frequency variations, and power quality issues. Therefore, a multilevel control structure can be considered for managing the output power of distributed PVs to mitigate operational challenges as shown in Fig. 1.1.

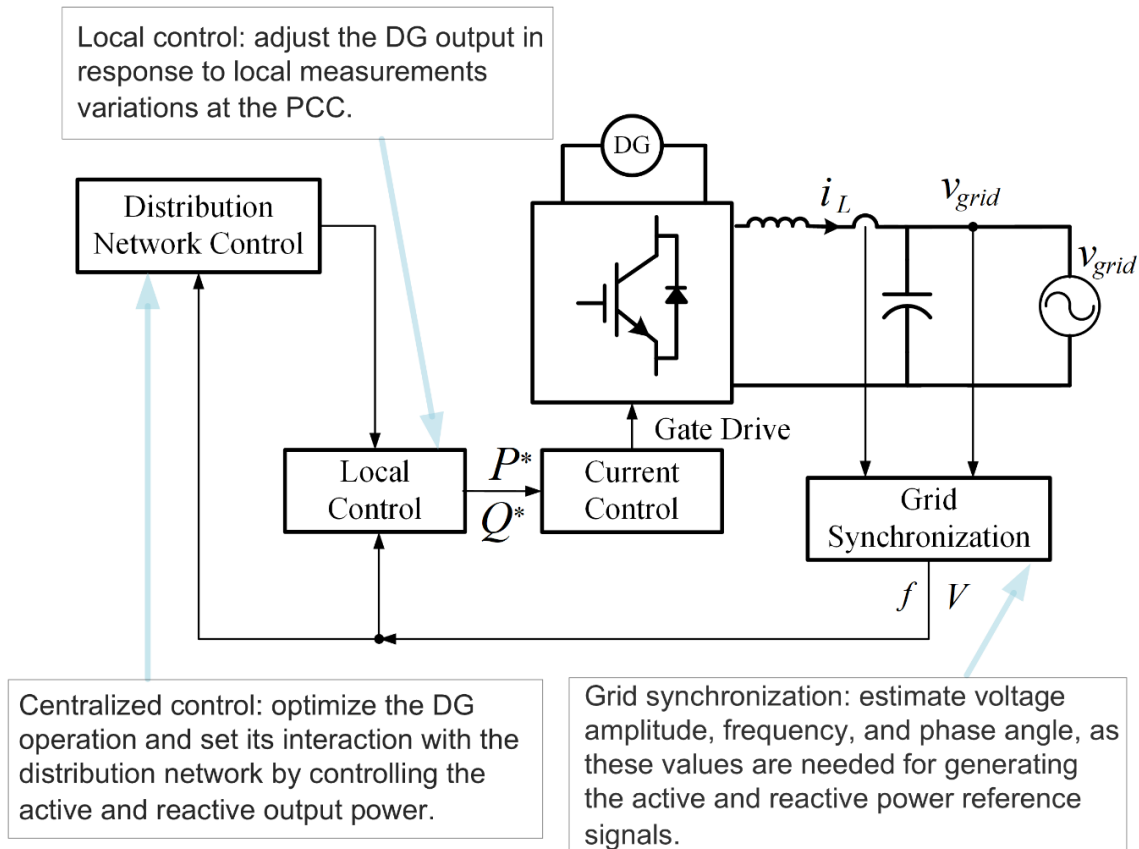


Figure 1.1. Block diagram of multilevel control structure for DG.

The synchronization of the PV inverter with the grid requires proper tracking of the phase and the amplitude of the voltage. The phase-locked loop (PLL) method is widely used for several applications, such as power electronics, communications systems, and microprocessors. The synchronous reference frame (SRF-PLL) is the common technique for grid synchronization because it inherently tracks the phase and amplitude of the voltage grid, while transforming the measured current and voltage to DC quantities along with the Park transformation. In weak grids, conventional SRF-PLL does not perform well, so it may fail in tracking the phase of the voltage and rejecting harmonics due to the high steady state error. By

reducing the bandwidth of the PLL, the steady-state error can be reduced, which is helpful in rejecting the harmonics and noise. Pre-filter delayed signal cancelation (DSC)-based techniques, along with the PLL, have been proposed to extract the fundamental component from the distorted voltage signal [7]–[9]. These techniques require knowledge of the harmonic components. Fast and accurate tracking of the phase and the amplitude of the voltage can improve the ride-through capability of the DER to remain synchronized with the grid during disturbances. SDFT-PLL algorithm has been proposed to extract an accurate phase angle of the fundamental voltage while rejecting the harmonics in a distorted or weak grid.

At high penetration levels of PV, high feed-in and reverse power occur under light load conditions. This high reverse power could lead to overvoltage at the end of the distribution feeder as shown in Fig. 1.2, resulting in voltage violation, which is limited to within ± 0.05 p.u. under normal operating conditions [10]. PV inverters conventionally operate at unity power

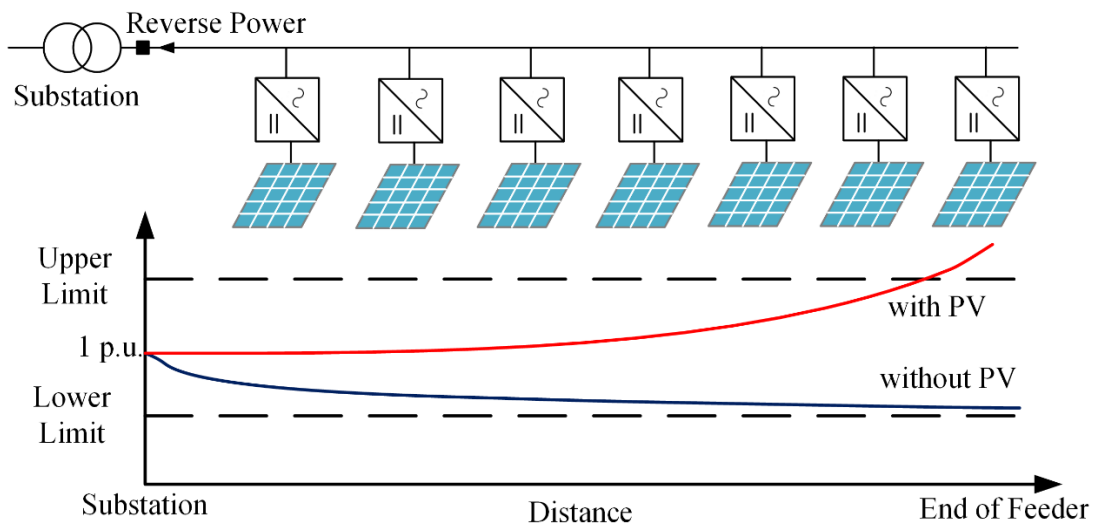


Figure 1.2. The impact of high level of PV penetration on feeder voltage profile under low load condition.

factor as they were not allowed to exchange reactive power with the grid to avoid conflicting operations with the other devices in the network due the lack of coordination as stated in IEEE 1547 Standard for Interconnecting Distributed Resources with Electric Power Systems. However, the IEEE 1547 first amendment and the recent revised grid codes in some countries allow DERs to regulate the voltage [11], [12].

Several approaches have been proposed to address the voltage rise issue and online voltage regulation in distribution networks. These approaches focus mainly on using PV inverters because they have the capability of supplying and absorbing reactive power to regulate the voltage [13]–[15]. In addition, some works have proposed utilizing conventional voltage regulation devices, such as an on-load tap changer and a step voltage regulator, along with PV inverters [16], [17]. The literature examines effective methods to regulate the voltage [18], [19]. However, overusing PV inverters for Volt/Var control causes additional losses in inverter switches that result in a temperature increase within these devices. The overutilization of inverters could negatively influence their reliability and decrease their lifetime [20]. This research presents a voltage regulation control strategy that includes solving for optimal power flow to minimize both distribution system losses and additional losses in the PV inverter caused by voltage regulation to relieve the thermal stress on inverters.

Distribution networks on-line Volt/Var control architectures can be classified into two main categories: decentralized and centralized. In decentralized approach, local measurements only required to perform the voltage control strategy. Droop-based control is applied extensively in decentralized approaches because of the simplicity [21], [22]. However, decentralized approaches require accurate forecast to tune local controller's parameters which is challenging because of the uncertain nature of solar PV. Therefore, Communication-based

centralized control for voltage regulation in distribution network can be considered to optimize DGs reactive power allocation [23], [24]. The real-time implementation of centralized control requires fast and reliable communication between DGs and the distribution system operator (DSO). This would rise the complexity of operating the distribution networks with high penetration level of PV units. This research investigates the effectiveness of combining local and central schemes for voltage regulation in distribution networks considering the integration of intermittent renewables. Using minimum communication, the DSO collects load and DG measurements every hour to optimize reactive power set-point of DG units to keep voltages within allowable limits. In addition, the central control uses a scenario-based approach to optimize local control parameters. This proposed strategy considers the uncertainty related to PV systems, and has been applied to a radial distribution feeder with high PV penetration.

The literature discusses various aspects of the impact of high PV penetration levels on distribution networks. However, the ongoing increase in PV penetration could lead to fundamental changes in operating transmission systems, such as handling the fluctuation and the lack of controllability of PV generations. In addition, a portion of conventional generation would be displaced, resulting in the loss of the main sources of dynamic reactive power in transmission networks. Consequently, power systems may become more vulnerable to voltage instability events after being subjected to major disturbances. In [25], the authors studied the impact of utility-scale PV generation on voltage stability and angle stability. Reference [26] investigates the impact of various levels of PV penetration on the power system's small signal stability. The P-V curve method has been proposed to improve the short-term voltage stability during faults using reactive power compensation from PV inverters [27]. A high penetration level of distributed PVs may adversely affect the dynamic behavior and stability of power

systems. Distributed PVs, when properly controlled, can provide ancillary services that are traditionally delivered by spinning generators and voltage regulators to support the bulk power system. For example, supplying reactive power by DGs to loads can enhance the power system's capability to eliminate large-scale and long-term blackouts and service outages [4]. Operating a power system with a high level of distributed PV penetration requires close coordination between the independent system operator (ISO) and DSO. This research investigates the impact of high PV penetration on a power system's long-term voltage stability. A case study is presented that provide dynamic reactive power reserves by distributed PV units to support the bulk power system.

1.3 Research Objectives

The objective of this research work is to study various aspects of the impact of distributed PV generation on the operation of the grid with the focus on addressing voltage regulation. The controller tasks have been distinctly separated between the local and central levels as shown in Fig. 1.3. The specific objectives of the research work are as follows:

- To improve the phase-locked loop method to achieve an accurate synchronization of a PV based DER with a weak or distorted grid and to provide fast-tracking performance in the fault condition.
- To investigate the effect of temperature variations on inverters' lifetimes in Volt/Var control strategies.
- To propose a centralized Volt/Var control strategy that allows better reactive power allocation among DERs, considering inverter utilization.

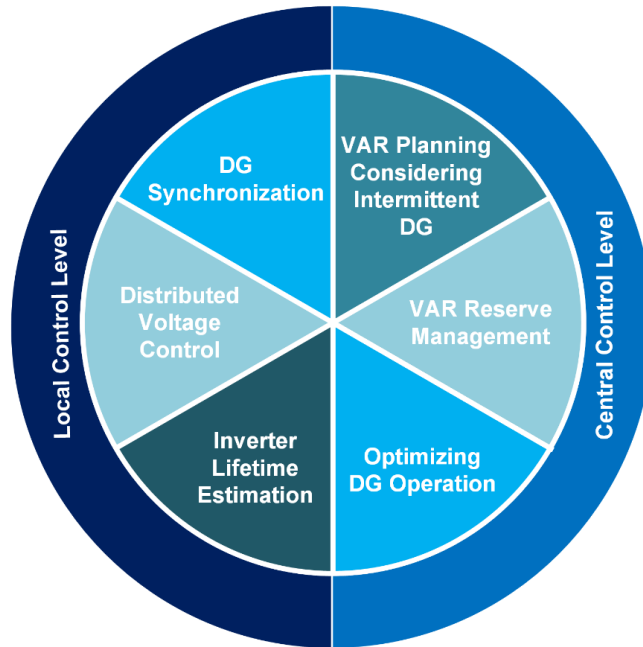


Figure 1.3. A graphic representation of the research aspects in this study.

- To propose a two-level Volt/Var control that accounting for the uncertainties associated with PV based DER systems.
- To study the impact on the bulk power system of scheduling PV based DERs to provide dynamic reactive power reserve.

1.4 Dissertation Outline

Chapter 2 describes the PV inverter control and lifetime estimation methods that will be used in this research, providing a detailed discussion of (1) the reliability of inverters, (2) the causes of inverter failure, and (3) the rainflow algorithm for inverter lifetime estimation.

This chapter includes a case study that investigates the effect of temperature variation on inverter lifetime.

Chapter 3 discusses the challenges of DER synchronization with the grid and presents an accurate DER synchronization method for use with a highly distorted grid. Simulation results in both steady-state and fault conditions are used to evaluate the performance of this method.

Chapter 4 discusses voltage regulation in distribution networks with high DER penetration. A radial distribution feeder with high DER penetration is considered for the analysis. This chapter presents the methods for providing reactive power by DER inverters to regulate the voltage throughout the distribution network. An optimal power flow method is employed to allocate reactive power among DER inverters. Using the inverter thermal model, a voltage regulation strategy in distribution networks with high DER penetration is proposed. The simulation results of the voltage control strategy are presented. Reliability analysis is conducted to determine the total damage of the inverters switches in the proposed approach.

Chapter 5 focuses on voltage regulation in the distribution network when integrating intermittent renewables. A combination of local and central control schemes is proposed to optimize the reactive power allocation to maintain voltage within the allowable limits. A scenario-based optimization approach is proposed to cover various scenarios to optimize DGs local control parameters. Based on the stochastic model of a PV system, the Monte Carlo Simulation (MCS) is used to generate the possible scenarios. To reduce the computational complexity of this strategy, the scenario reduction algorithm is applied to reduce the number of scenarios to a manageable set. The effectiveness of the approach is demonstrated through simulations.

Chapter 6 focuses on the impact of high PV penetration on the bulk power system and describes the role of a reactive power reserve in the voltage stability of the power system. Both a static power flow-based method and a dynamic simulation are used to assess the long-term voltage stability. Contingency analysis has been carried out to identify the most critical outages in the power system. This chapter investigates the impact of scheduling distributed PVs to provide dynamic reactive power compensation during contingencies.

Chapter 7 summarizes the work in this dissertation. In addition, this chapter lists the tasks that need further study.

2 PV Inverter Control and Reliability

2.1 PV Inverter Control

To connect PV modules to the grid, two stages are needed to achieve efficient power conversion and accurate synchronism with a utility. Fig. 2.1 shows the block diagram of a PV system with two stages. The first stage includes a DC-DC converter to regulate the voltage across the DC-link and apply maximum power point tracking (MPPT), while the second stage includes a DC-AC inverter interface of a PV module to the grid through an LC filter. Both stages require a controller and pulse width modulation (PWM). This research mainly focuses on the inverter because it is the key element in exchanging reactive power with the grid.

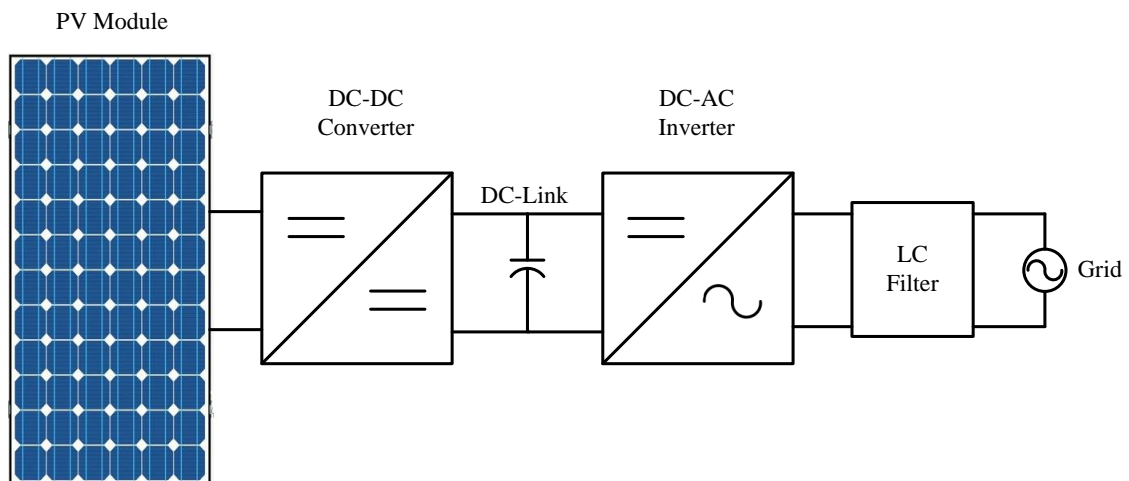


Figure 2.1. The impact of high level of PV penetration on feeder voltage profile under low load condition.

2.1.1 PV Inverter Architectures

Regarding the size and architecture of PV modules to the grid, inverters can be classified into two main types: micro inverters and string inverters. Micro inverters are used to interface with a single PV module, as shown in Fig. 2.2. This type of inverter is more highly efficient and reliable because when one component fails, the other micro inverters continue to work without interruption. However, using this type increases the cost of installation for the overall PV system and makes centralized control of the output production more complicated than with a string inverter [28].

String inverters are widely used for interfacing PV modules to the grid, where PV modules are series-connected to a single inverter, as shown in Fig. 2.3. String inverters offer a

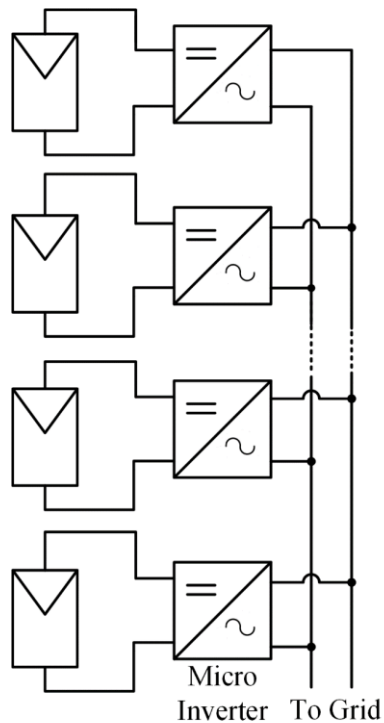


Figure 2.2. Micro inverter architecture.

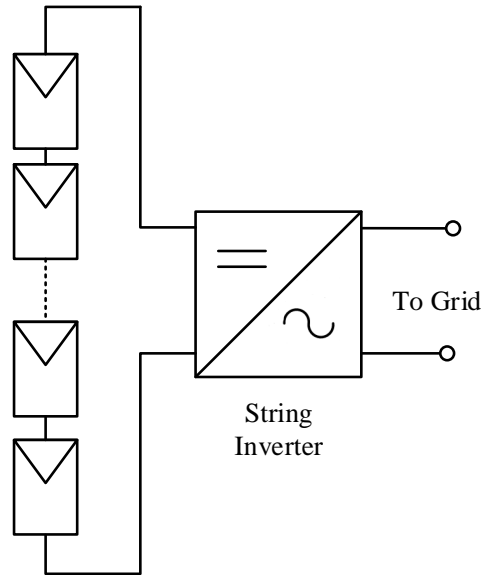


Figure 2.3. String inverter architecture.

broad range of output power from multiple kW to 2 MW and can be used to interface PVs with three-phase or single-phase systems. This type of inverter technology is mature and fully accepted by the industry due to its ease of control and simple architecture with fewer components. However, string inverters suffer from short lifespans, and most manufacturers' warranties only cover five to 10 years [29].

2.1.2 Inverter Topology

Recently, several PV grid-tied inverter topologies have been proposed to mitigate connection issues and to improve power conversion efficiency [30]–[32]. Nonetheless, two-level voltage source inverters (VSIs) are still widely used in connecting PV systems to medium- and low-voltage distribution networks. This is due to the simplicity of the inverter structure, where fewer components are needed for this topology, leading to higher reliability [33]. In addition, the ease of controllability is the main reason for implementing two-level VSIs

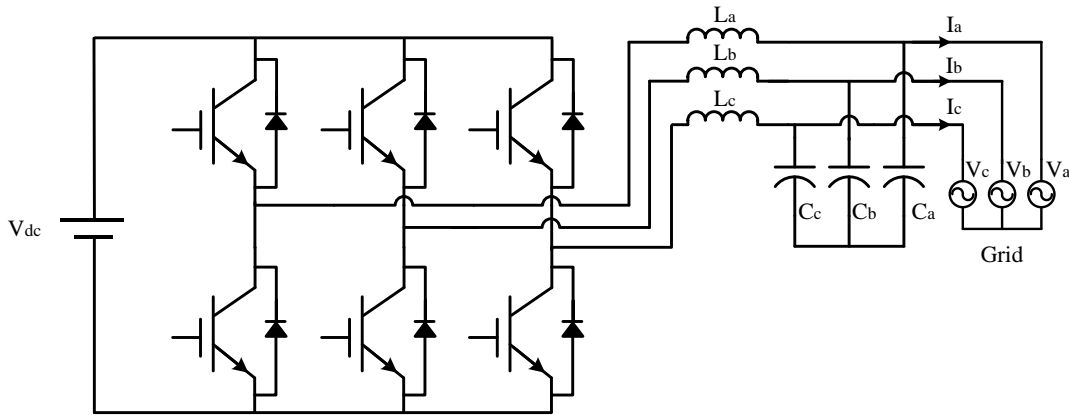


Figure 2.4. Grid-tied three-phase VSI inverter.

in PV systems. In this work, a two-level voltage source inverter (VSI) employing insulated-gate bipolar transistor (IGBT) switch inverters and diodes was considered due to its ease of controllability. Fig. 2.4 shows a three-phase VSI inverter with an LC filter for the grid-tied application.

2.1.3 Inverter Control

In grid-connected mode, a current-control method (CCM) for VSI (CCM-VSI) is widely used. This controlling strategy is responsible for performing three main tasks: (1) controlling the amount of output active power production, (2) controlling the amount of exchanged reactive power between the inverter and the grid, and (3) synchronizing the inverter by tracking the grid frequency and voltage.

Since a grid-tied PV system uses an MPPT algorithm to maximize the harvested energy from solar cells, CCM-VSI allows maximum active power production. However, active power curtailment can be applied to limit power production if the distribution network cannot tolerate excess power or due to any operating constraints. As the installed VSI capacity is measured by its real power rating, a VSI can exchange reactive power with the grid by acting as a shunt

reactor or capacitor. CCM-VSI dictates the available capacity of reactive power after performing MPPT because the main priority is to harvest active power in PV systems.

In the recent past, IEEE 1547 did not recommend using distributed energy resources (DER) in actively reactive power management. IEEE Standard 1547a-2014 includes an amendment that allows for active voltage regulation and reactive power management using DER [11]. However, this requires a coordinated effort between the power system and DER operators to prevent voltage violations at other locations within the grid. This active coordination between system operators in regulating voltage can lead to higher penetrations of DER in the power system, especially in relation to renewable-based DER, such as PV. In Chapters 4 and 5, voltage regulation in distribution networks with a high penetration of PV will be addressed.

Synchronizing the PV inverter to the utility network requires matching its voltage amplitude, voltage phase, and frequency with the grid. In addition, fast-tracking frequency drifts and voltage variations are essential to maintain this synchronism since power systems are vulnerable to transient events. In Chapter 3, improving PV inverter synchronization in distorted grid conditions will be addressed.

Several control algorithms have been proposed to regulate the output of real power [34]–[37], with the inner-outer loop structure being commonly cited in the literature. The outer loop is responsible for passing real power commands to the inner loop, which compensates for the inverter current command error. Inner loop compensation strategies can be classified based upon the reference frame into three main types: natural frame, stationary reference frame, and synchronous reference frame. In natural reference control, the controller is designed to deal with voltage and current measurements without the transformation required by the other two

methods. Hysteresis control was very common in analog control systems and was used extensively in the last century [38], [39]. However, its major drawback is the difficulty of controlling the switching frequency. However, by reducing the bandwidth between the two reference signals (i.e., the upper and lower bands), the switching frequency can be kept almost constant [39]. Stationary reference frame control based on α - β transformation is well-known in the power electronics control field. Under α - β coordinates, a proportional resonant (PR) controller was proposed to regulate the VSI output current [40]. The PR current controller can remove the steady-state error when controlling sinusoidal waveforms. A modified PR control was proposed to compensate for any harmonics [41]. However, this controller is highly sensitive to the accuracy of system parameters, making it a challenging task to tune the PR controller [42].

Synchronous reference frame (SRF) control, known as dq transformation, which is based on the Park transformation, has been broadly used in the literature to regulate VSI current [43], [44]. In this approach, the three-phase voltage quantities in the natural reference frame abc are transformed into α - β coordinates. These new voltages are transformed into d - q coordinates rotates at the angular velocity (ω_e) of fundamental voltage in the natural reference frame. Fig. 2.5 shows the dq transformation steps graphically. For a mathematical representation, a set of balanced, three-phase voltage equations are considered:

$$v_a = V_m \cos \theta \quad (2.1a)$$

$$v_b = V_m \cos \left(\theta - \frac{2\pi}{3} \right) \quad (2.1b)$$

$$v_c = V_m \cos \left(\theta + \frac{2\pi}{3} \right) \quad (2.1c)$$

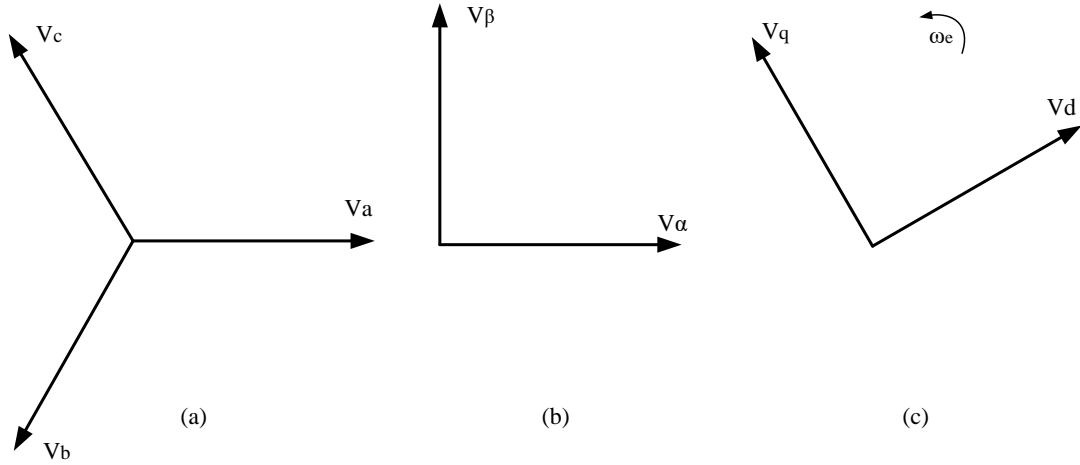


Figure 2.5. Graphic representations of a dq transformation: (a) balanced three-phase voltages, (b) voltages in a $\alpha\beta$ coordinate, and (c) voltages in a $d-q$ coordinate.

The abc voltages can be mapped into $\alpha\beta$ coordinates using the Clark transformation, as follows:

$$\begin{bmatrix} v_\alpha \\ v_\beta \end{bmatrix} = \frac{2}{3} \begin{bmatrix} 1 & -\frac{1}{2} & -\frac{1}{2} \\ 0 & \frac{\sqrt{3}}{2} & -\frac{\sqrt{3}}{2} \end{bmatrix} \begin{bmatrix} v_a \\ v_b \\ v_c \end{bmatrix} \quad (2.2)$$

In addition, v_α and v_β would be transformed into $d-q$ coordinates as follows:

$$\begin{bmatrix} v_d \\ v_q \end{bmatrix} = \begin{bmatrix} \cos \varphi & \sin \varphi \\ -\sin \varphi & \cos \varphi \end{bmatrix} \begin{bmatrix} v_\alpha \\ v_\beta \end{bmatrix} \quad (2.3)$$

where φ is the extracted angle from the PLL that allows the tracking system phase to perform the SRF transformation. Also, v_d and v_q are totally decoupled and can be simply represented as

$$v_d = V_m \cos(\theta - \varphi) \quad (2.4)$$

$$v_q = -V_m \sin(\theta - \varphi). \quad (2.5)$$

Considering accurate phase tracking under the steady-state condition, $(\theta - \varphi)$ becomes very small, allowing further simplification of v_d and v_q , as follows:

$$v_d \cong V_m \quad (2.6)$$

$$v_q \cong \theta - \varphi. \quad (2.7)$$

The dq -axis voltages are time-independent in SRF and can be represented by DC quantities. The previous equations hold for the current transformation. The power theory can be used to drive the instantaneous injected active and reactive power by the inverter as represented in the following equations:

$$p = \frac{3}{2}(v_d i_d + v_q i_q) \quad (2.8)$$

$$q = \frac{3}{2}(v_d i_q + v_q i_d) \quad (2.9)$$

The v_q component is small enough to be neglected when controlling the inverter output active and reactive power. The following conclusions can be drawn from the dq transformation and instantaneous power equations:

- 1) The d -axis voltage component v_d is transformed into a DC quantity and holds the peak value of the phase voltage.
- 2) The q -axis voltage component v_q is forced to be zero, allowing the decoupling inverter controller to manage active and reactive power separately.
- 3) The d -axis current component i_d contributes directly to the instantaneous active power.
- 4) The q -axis current component i_q contributes directly to the instantaneous reactive power.

5) The peak phase current of the inverter can be expressed as follows:

$$I_m = \sqrt{i_d^2 + i_q^2}. \quad (2.10)$$

A grid-tied, three-phase VSI with an LC filter was considered to design the current controller in the SRF. To drive the controller model, the power stage circuit for a single-phase was used, as shown in Fig. 2.6. The large-signal model per phase of the VSI dynamics is given as

$$v_o(t) = Ri_L(t) + L \frac{di_L}{dt} + u * V_{dc} \quad (2.11)$$

where R is an equivalent series resistance (ESR) of the inductor and u is the switch status, both of which can form different combinations based upon the type of controller.

To achieve good tracking, the dynamic model can be linearized at the operating point. For this purpose, the VSI average model can be obtained using the following equation:

$$\langle v_o(t) \rangle = R \langle i_L(t) \rangle + L \frac{d \langle i_L \rangle}{dt} + \langle v^* \rangle \quad (2.12)$$

where the new input v^* represents the control variable. The VSI dynamic model can be transformed into the dq reference frame at the angular speed ω and represented by the following equations:

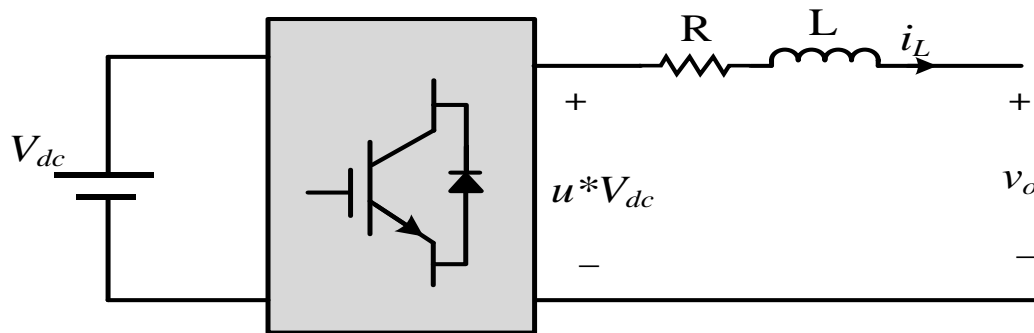


Figure 2.6. Power stage of the VSI.

$$v_d^* = Ri_{Ld} + L \frac{di_{Ld}}{dt} - \omega i_{Lq} + v_{od} \quad (2.13)$$

$$v_q^* = Ri_{Lq} + L \frac{di_{Lq}}{dt} + \omega i_{Ld} + v_{oq} \quad (2.14)$$

where v_{od} , v_{oq} , i_{Ld} , i_{Lq} are the dq -axis voltage and currents of the VSI. Additionally, v_d^* and v_q^* are the control signal that is obtained from the dq -axis to form the output voltage based on the current regulator. A cross-coupling term between the d and q coordinates was introduced in (2.13) and (2.14) because of the inductive term L . However, a decoupling term can be added within the controller itself to eliminate the coupling between the two coordinates. The dynamic plant model is represented by the following transfer function equation:

$$H(s) = \frac{1}{sL + R}. \quad (2.15)$$

It is obvious that the transfer function $H(S)$ is of the first order. A proportional-integral (PI) controller is a reasonable choice, especially after transforming the currents and voltages to DC quantities so that the steady-state error can be easily eliminated when using this type of controller. Two separate PI controllers are needed for the control structure, as follows:

$$G_{dq}(s) = K_p + \frac{K_I}{s} \quad (2.16)$$

where K_p is the proportional gain, and K_I is the integral gain. Fig. 2.7 shows the block diagram of the dq current control that is used to form the voltage reference based on the output current requirement. As such, v_d^* and v_q^* will be transformed into the abc frame using the inverse dq transformation and passed to pulse width modulation (PWM) to generate gate-drive signals. The overall current-controlled VSI scheme in the dq reference frame is shown in Figure 2.8.

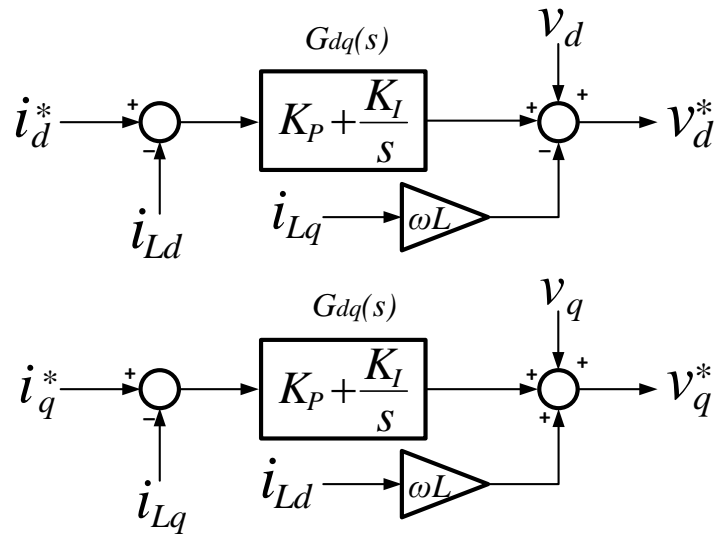


Figure 2.7. Block diagram of a dq current controller.

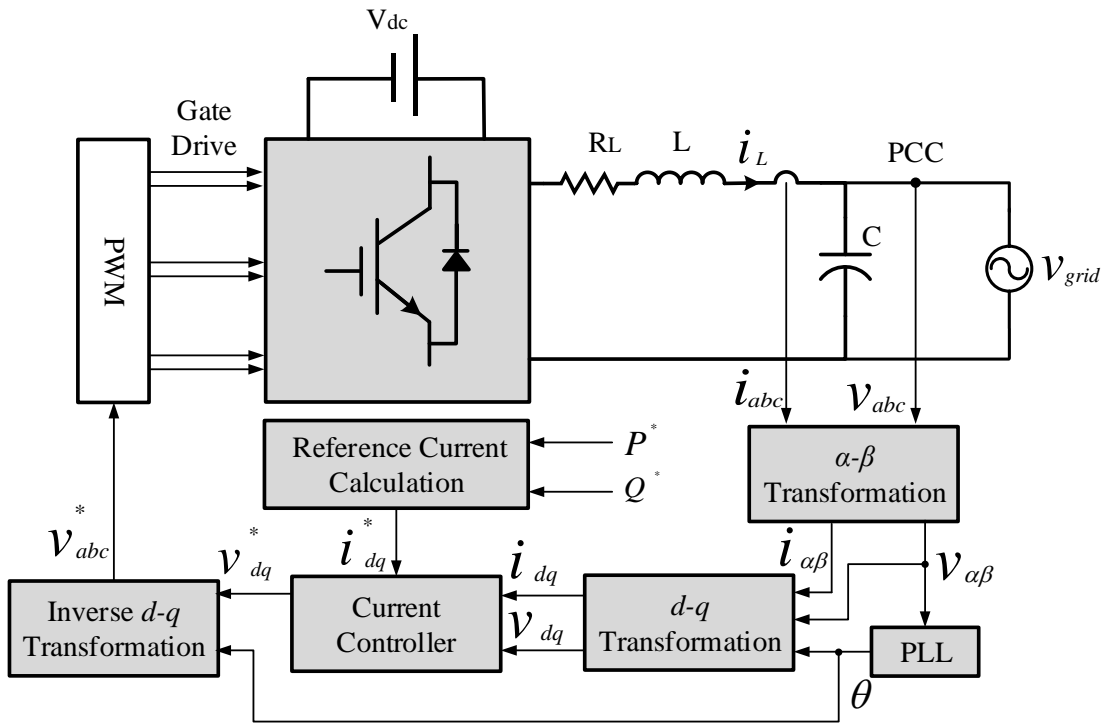


Figure 2.8. Scheme of a current-controlled inverter in the synchronous reference frame.

2.2 PV Inverter Reliability

In most inverter control strategies, ideal power electronic switches are considered, whereas the power consumption in these devices is neglected. To avoid switch destruction, only the maximum junction temperature is used to set the real power rating of the device. Therefore, the controller is responsible for maintaining real power output below the associated safe operating value with the junction temperature. Simply, a PV inverter can be oversized to ensure that it operates within the thermal limit because the active power production of PV modules can be easily estimated.

The upfront cost of PV systems is still high, regardless of the cost reductions in recent years [1]. Therefore, the long-term performance of a PV system needs to be well studied and a reliability evaluation of its components must be conducted. PV modules are well-known for their reliability, for which most manufacturers provide a 25-year warranty. The National Renewable Energy Laboratory (NREL) published a historical survey of the PV degradation rate for systems from around the globe during the last 40 years [45]. The historical data shows that the degradation rate of PV modules is less than 1% per year. This report concluded that PV modules allow reasonable performance even after 25 years. In [46], a reliability evaluation of 350 PV systems designed and operated by SunEdison, Inc. were investigated. This study included 3,500 tickets issued between January 2010 and March 2012 for PV systems. Only 2% of the tickets were associated with PV module failures. PV inverters were responsible for 43% of the issued tickets, which were the biggest cause of PV system outages compared to other components. According to a survey in [47], typical PV inverters come with a five-year warranty.

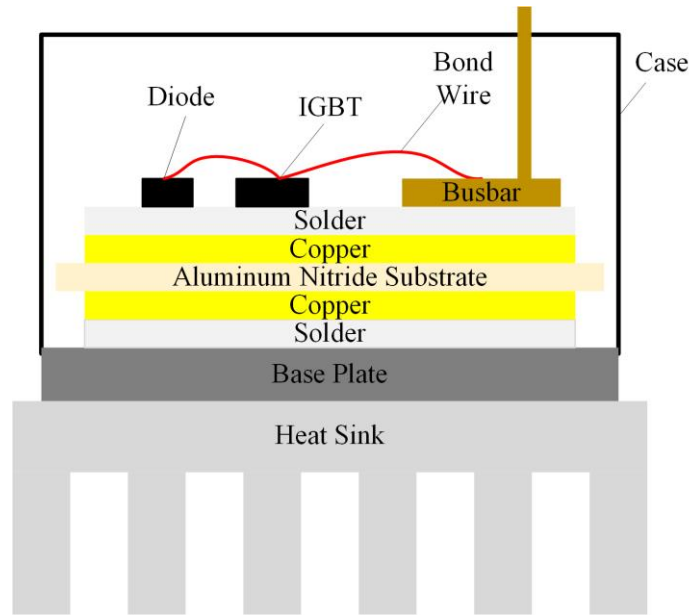


Figure 2.9. Cross-sectional structure of a conventional IGBT.

Several causes can lead inverters to fail, including control software, printed circuit boards (PCBs), internal fuses, contactors, surge protection, and IGBTs. The scope of this work focuses on the effect of using PV inverters in Volt/Var control, as will be presented in Chapter 4. Therefore, the reliability and lifetime estimation of power electronic switches will be considered. The most common cause of power electronics devices damage is packaging failures due to thermal-mechanical fatigue [48]. Fig. 2.9 shows a cross-sectional structure of a conventional IGBT module. The IGBT module consists of multiple layers of different materials, with silicon to solder the layers. Under thermal cycles, the solder layer suffers from a degradation resulting in increased thermal resistance between the layers. This degradation is caused by a thermal coefficient expansion (CTE) mismatch between the copper and silicon layers. A crack propagation might be developed due to cyclic, mechanical stress in the solder layer, ultimately resulting in IGBT failure [49]. Bond wire is another common mode of failure of an IGBT module. Bond wires are made from aluminum, which has a coefficient of thermal

expansion (CTE) higher than silicon, making bond wires vulnerable to thermal-mechanical fatigue due to thermal cycles. The cyclic expansion of the bond wires weakens the joint between the chip and the wire. This mode of failure is commonly known as bond wire lift-off [50].

Estimating the IGBT junction temperature involves analyzing the electrical and thermal properties of the module. In addition, the behaviors of the discrete switches are decided by pulse-width modulation (PWM) under a wide range of loading conditions. Therefore, this process is computationally extensive, and a computer-based method is needed for accurate estimation.

The finite element method (FEM) is commonly used in studying the thermal, electrical, electromagnetic, and mechanical behavior of power electronics modules during the design stage [51]–[53]. FEM-based simulations allow accurate and comprehensive analysis of thermal distribution because the IGBT module has more than one source of heat. A new Fourier series (FS) thermal model was proposed by Hudgins et al. [54], who found this method to be more computationally efficient compared to FEM, making it more suitable for the dynamic thermal characterization of power semiconductor switches. Numerical methods, such as FEM and FS, are essential in developing IGBT modules. However, these methods suffer from high computational and memory costs, making their use impractical in accelerated life testing applications.

To overcome the drawback of the aforementioned methods, thermal models based on Foster and Cauer networks are used extensively in the literature to develop accelerated life testing of IGBT modules [20], [50], [55]. Each layer in the IGBT module can be represented by its equivalent thermal impedance. The temperature at each node between the layers can be

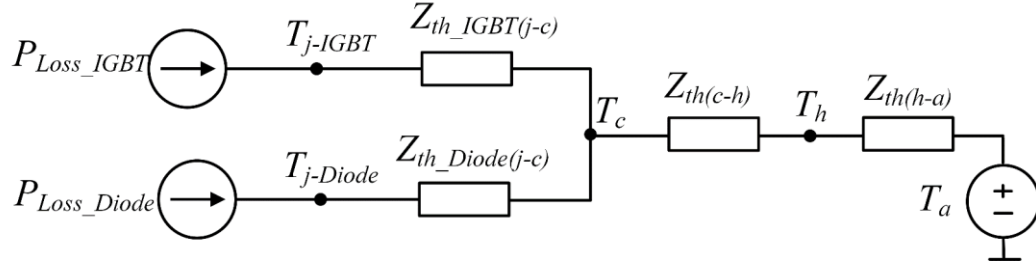


Figure 2.10. Thermal model of a power semiconductor device.

found by solving for the equivalent circuit of the thermal model. The ambient temperature is modeled as a voltage source. The thermal path from the ambient air to the device chip is shown in Fig. 2.10. The main advantages of this model are the low computational time and the ease of implementation in online control applications.

Losses in power electronic devices are a function of the voltage, current, frequency, and temperature. Typically, a manufacturer's data sheet specifies the electrical and thermal characteristics of power electronic devices in relation to operating conditions. The junction temperature T_j has a direct effect on the electrical performance and dissipated power of power devices.

The thermal model provides an estimate of the junction temperature T_j to be used in the PV inverter power loss calculation. T_j can be found from the thermal model as [56]

$$T_{j_IGBT} = P_{Loss_IGBT} Z_{th_IGBT(j-c)} + T_c \quad (2.17)$$

$$T_{j_Diode} = P_{Loss_Diode} Z_{th_Diode(j-c)} + T_c \quad (2.18)$$

$$T_c = T_a + [P_{Loss_IGBT} + P_{Loss_Diode}] \times [Z_{th(c-h)} + Z_{th(h-a)}] \quad (2.19)$$

where P_{Loss_IGBT} and P_{Loss_Diode} are the power losses in the IGBT and diode, respectively; T_{j_IGBT} and T_{j_Diode} are the junction temperatures in the IGBT and diode, respectively;

$Z_{th_IGBT(j-c)}$ and $Z_{th_Diode(j-c)}$ are the thermal impedance between the junction and the case for the IGBTs and diodes, respectively; and $Z_{th(c-h)}$ and $Z_{th(h-a)}$ are the thermal impedances from the case to the heat sink and from the heat sink to the ambient air, respectively. All of the thermal impedances can be found from the device data sheet.

The dissipated power in power electronic devices consists of conduction and switching losses. The average conduction loss or forward loss of the IGBT ($P_{C,IGBT}$) is the product of the collector current and the voltage across the switch divided by the on-state period and can be expressed as

$$P_{C,IGBT} = \frac{1}{T} \int_0^T (v_{ce}(t) \times i_c(t) \times D) dt \quad (2.20)$$

$$v_{ce}(t) = V_{ce0} + r_{ce} \times i_c(t) \quad (2.21)$$

where $v_{ce}(t)$ is the instantaneous collector-emitter voltage across the IGBT, $i_c(t)$ is the instantaneous collector current through the IGBT, D is the duty cycle over the time period (T), V_{ce0} is the threshold voltage, and r_{ce} is the on-resistance of the IGBT. Fig. 2.11(a) shows a typical output characteristic of an IGBT from a data sheet [57].

The switching losses associated with the turn-on and turn-off energy losses are caused by the switching delay time because the transitions between the two states do not occur instantaneously. The turn-on and turn-off energy losses of the IGBT are affected by the reverse recovery energy from the freewheeling diode and internal parasitic elements [58]. The switching power loss equation can be expressed as follows:

$$P_{IGBT_switching}(t) = (E_{IGBT-on} + E_{IGBT-off}) f_{sw} \quad (2.22)$$

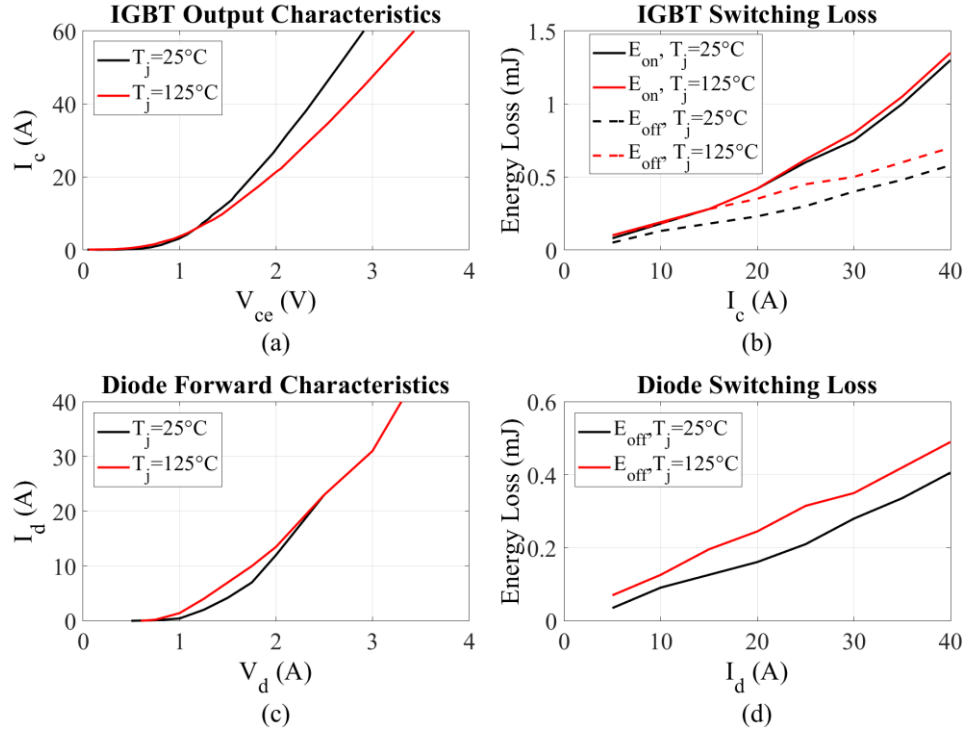


Figure 2.11. Typical performance characteristics of an IGBT [57].

where $E_{IGBT-on}$ and $E_{IGBT-off}$ are the switching energy loss during turn-on and turn-off, respectively; and f_{sw} is the switching frequency of the inverter. Fig. 2.11(b) shows graphs of the switching loss energy values in both states versus the collector current.

The dissipated power characteristics in the freewheeling diode are similar to the IGBT. The conduction loss in diodes ($P_{C,Diode}$) is a function of the voltage, current, and duty ratio.

$$P_{C,Diode} = \frac{1}{T} \int_0^T (v_d(t) \times i_d(t) \times (D - 1)) dt \quad (2.23)$$

$$v_d(t) = V_{d0} + r_d \times i_d(t) \quad (2.24)$$

where $v_d(t)$ is the instantaneous forward voltage drop across the diode, $i_d(t)$ is the instantaneous conduction through the diode, V_{d0} is the threshold voltage, and r_d is the forward resistance of the diode. Fig. 2.11(c) shows diode forward characteristics.

The diode turn-on energy loss is neglected because the charging time is very short. However, the discharge time or reverse recovery time of diodes requires a finite period of time. Therefore, only diode turn-off energy loss is considered in calculating the switching power loss:

$$P_{Diode_switching} = E_{Diode-off} \times f_{sw} \quad (2.25)$$

where $E_{Diode-off}$ is the diode switching energy loss during turn-off. Fig. 2.11(d) shows graphs of the switching loss energy values versus the conduction current.

2.2.1 Cycle Counting

A PV inverter is subjected to cyclic temperature variations due to loading and ambient conditions. The varying thermal loss imposed on the device ages the internal connections. To estimate a semiconductor's lifetime, a fast power-cycling test for the inverter module was developed by Held et al. [59]. Their analytical lifetime estimation approach is based on the Coffin-Manson-Arrhenius model, which has been widely used in similar studies to predict failures due to material fatigue [20], [50], [55]. The Coffin-Manson-Arrhenius model for cycles to fail (N_f) can be expressed as

$$N_f(\Delta T_j, T_m) = A \times \Delta T_j^{-\alpha} \times e^{\frac{Q}{RT_m}} \quad (2.26)$$

where R is the gas constant (8.314 J/mol.K), T_m is the mean junction temperature in Kelvin over one power cycle, Q is the internal energy (7.8×10^4 J.mol⁻¹), and ΔT_j is the range of junction temperature. A and α are module constants.

The power cycling profile depends on the loading conditions. Therefore, climate data, including historical tables of ambient temperature and solar radiation, are needed to create a

mission profile for this study. Junction temperature cycles do not follow specific patterns due to the random nature of solar radiation. For example, an annual power profile of a given inverter operated at 60 Hz would contain millions of power cycles, and testing every power and thermal cycle is a time-consuming and complicated process. To reduce the complexity of the thermal profile, several cycle-counting methods have been proposed [60]–[62]. Counting for temperature swings (i.e., rise and fall) is the basis of estimating the lifetime. A rainflow cycle-counting method was used in this study. The rainflow counting algorithm was first developed by Matsuishi and Endo in [63], and it has become the most accepted cycle-counting method in many fields and was included in ASTM E1049-85 “Standard Practices for Cycle Counting in Fatigue Analysis” [64]. Implementing this algorithm reduces the continuous thermal cycles to a sequence of peaks and valleys. Also, noise and very small cycles can be eliminated based on the application. The strain cycles between peaks and valleys can also be represented by closed stress-strain hysteresis loops, as shown in Fig. 2.12.

Strain ratio is related to a change in the dimensions of a material with respect to its original shape; this change is primarily due to temperature variations in power electronic devices. Therefore, temperature swings can be used instead of strain to estimate the total degradation for a given load profile. The rainflow algorithm is applied to count the peaks and valleys. A temperature profile is illustrated in Fig. 2.13 to explain the cycle-counting method. The rainflow algorithm starts by searching for local minima and maxima of temperature data to locate cycles. The next step is to identify the cycle time length, the amplitude range (ΔT), and the mean (T_m), based on closed stress-strain loop information. Fig. 2.14 shows the extracted cycles from the rainflow counting, while cycle information is listed in Table 2.1.

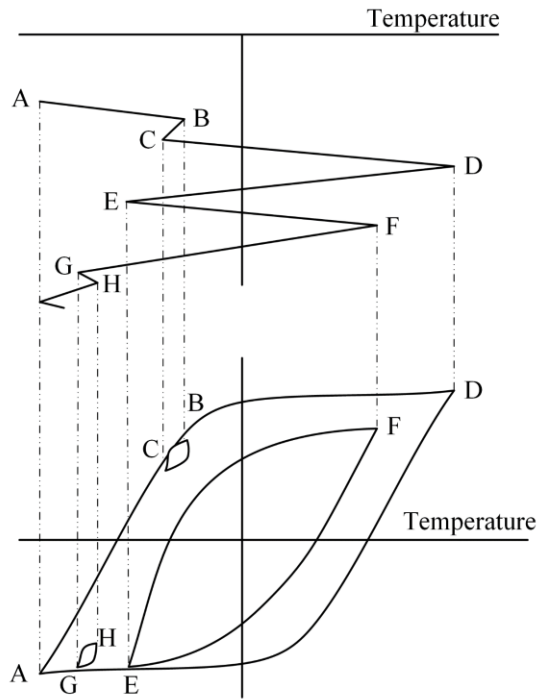


Figure 2.12. Temperature profile and the corresponding closed stress-strain hysteresis loops.

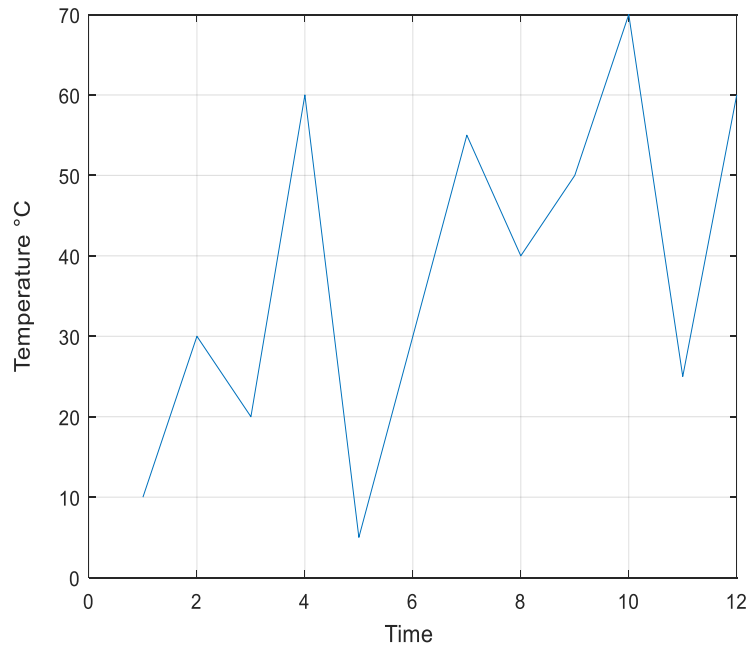


Figure 2.13. Temperature profile.

Table 2.1. Cycle information from the rainflow counting algorithm applied to the temperature profile in Fig. 2.15.

Counted Cycles	Extreme Points	Full or Half Cycle	Amplitude	Mean
1	30-20-30	1	5	25
2	10-60	0.5	25	35
3	55-40-50	1	7.5	48.3
4	60-5	0.5	27.5	32.5
5	5-70	0.5	32.5	37.5
6	70-25	0.5	22.5	47.5
7	25-60	0.5	17.5	42.5

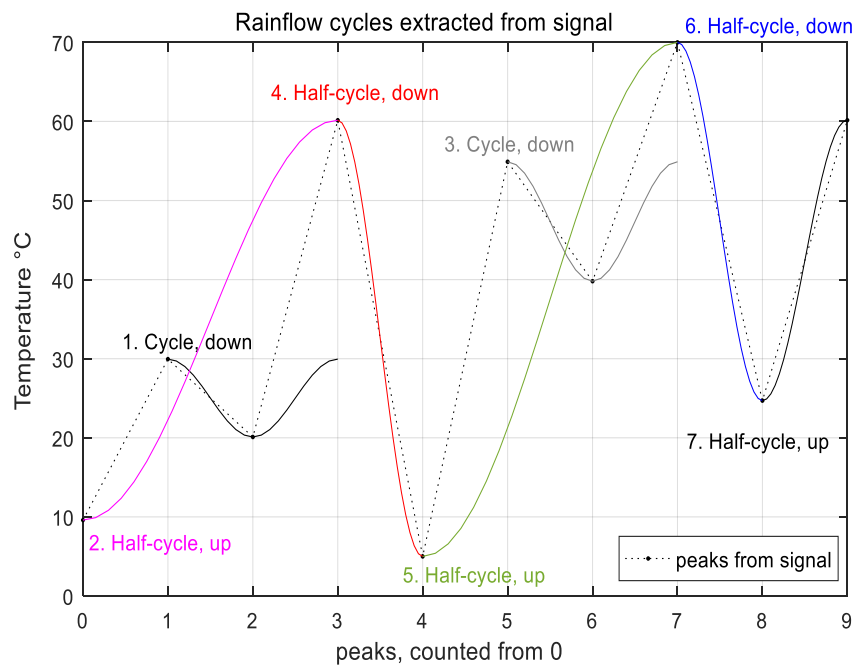


Figure 2.14. Rainflow cycles extracted from the temperature profile in Fig. 2.13.

The extracted information from the algorithm can be applied directly to the Coffin-Manson-Arrhenius model to determine the number of cycles to fail under a specific ΔT_j and T_m . To find the total damage for a given temperature profile, the Palmgren-Miner linear damage accumulation rule was used [65]. The accumulated damage due to temperature cycling is given by

$$D = \sum_i \frac{n_i(\Delta T_j, T_m)}{N_{f,i}(\Delta T_j, T_m)} \quad (2.27)$$

where n_i is the number of cycles extracted from the rainflow algorithm for a specific ΔT_j and T_m . The damage will occur when $D \approx 1$ for a given power loading cycle. However, an estimate of the partial degradation can be found for a specific period. The flowchart in Fig. 2.15 shows the steps of the reliability analysis in this study.

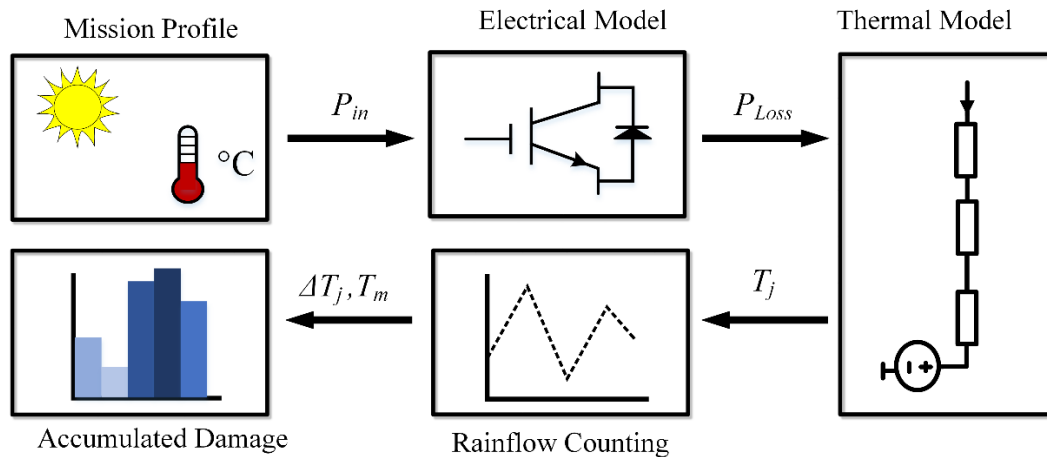


Figure 2.15. Reliability analysis of a power electronic devices flowchart.

2.3 Simulation Results

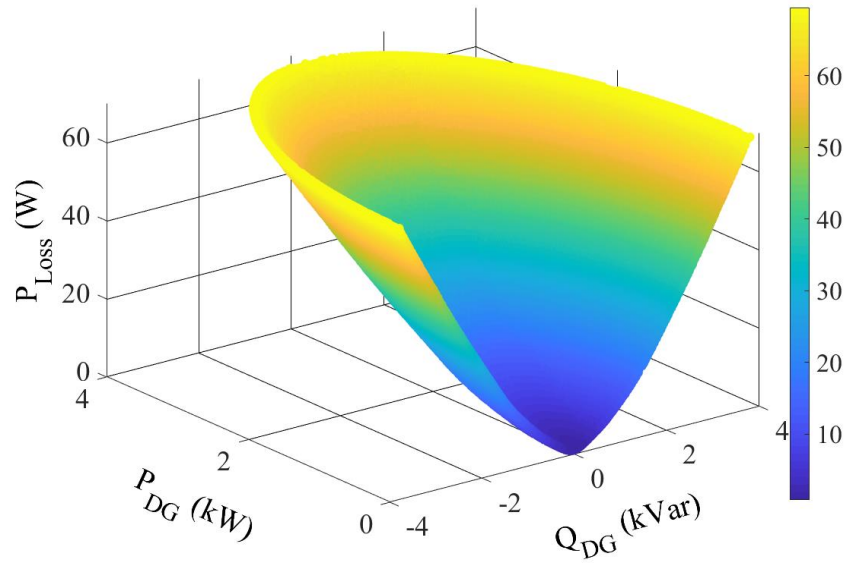
In this section, simulations were carried out using MATLAB/Simulink and PLECS® to investigate the thermal performance of the inverter switches. A three-phase inverter module from a leading manufacturer was selected for this purpose. The PV inverter was connected to a secondary distribution feeder of 240 V, as shown in Fig. 2.8. The electrical and thermal parameters of the PV inverter are summarized in Table 2.2.

Table 2.2. Electrical and thermal parameters of the inverter.

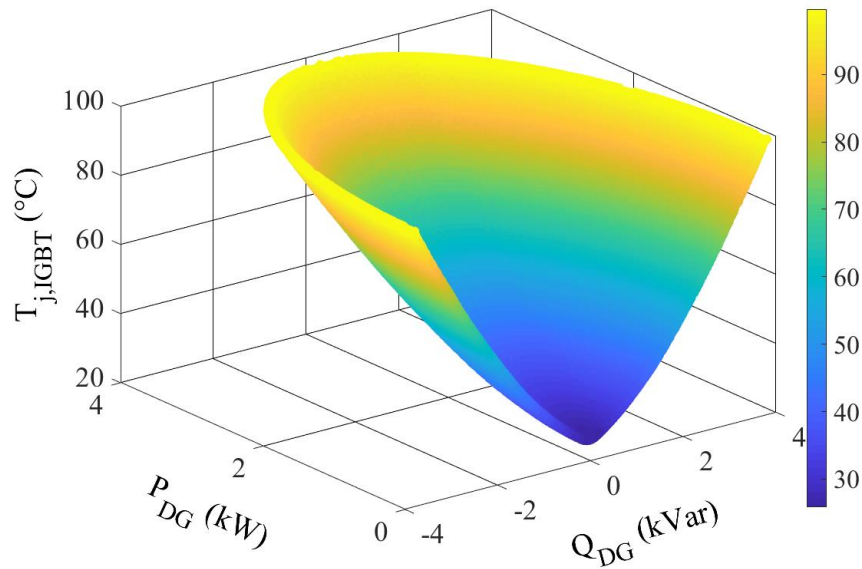
Inverter rated power		3.8 kVA
DC link voltage		500 V
Grid voltage		240 V
Grid frequency		60 Hz
Switching frequency		10 kHz
Output inverter filter	Inductor	5 mH
	Capacitor	10 μ F
Current controller	K_P (Proportional gain)	5
	K_I (Integral gain)	100
IGBT	$V_{ce(max)}$	600 V
	$I_c(max)@ T_c = 25^\circ C$	40 A
Diode	V_d	2 V
Thermal Impedance	$Z_{th_IGBT(j-c)}$	0.76°C/W
	$Z_{th_Diode(j-c)}$	1.51°C/W
	$Z_{th(c-h)}$	0.7°C/W
	$Z_{th(h-a)}$	0.61°C/W

The thermal model was used to calculate the losses and the junction temperature in the inverter for a wide range of loading conditions and ambient temperatures (T_a). The range of T_a was -5°C to 45°C , with 1°C increments. The inverter IGBT junction temperature and total losses were calculated over small increments of the output active and reactive power to cover the operating range of the inverter. Thus, lookup tables were created, consisting of the inverter thermal performance data, to simplify the process of estimating the inverter IGBT junction temperature and total losses at any given T_a , P_{DG} , and Q_{DG} . Fig. 2.16(a) shows the total losses in the PV inverter with active and reactive power supplies at $T_a = 25^{\circ}\text{C}$. It is obvious that exchanging reactive power with the grid, whether it is positive or negative, will lead to additional power losses in the inverter. Therefore, using the PV inverter to supply reactive power will result in elevating the junction temperature of the IGBT device, as shown in Fig. 2.16(b). Notably, the maximum total losses occur when the PV inverter operates at its rated apparent power of 3.8 kVA.

To evaluate the reliability of the PV inverters over a long time span, yearly mission profiles of the solar irradiance and ambient temperature were considered in the case study. The solar irradiance and ambient temperature data (15-min resolution) were obtained from the Solar Resources and Meteorological Assessment Project (SOLRMAP), developed by the National Renewable Energy Laboratory (NREL) [66]. Figs. 2.17(a) and (b) show the mission profiles of the solar irradiance and ambient temperature, respectively. All yearly mission profiles are from Phoenix, Arizona, collected in 2011, for the entire year.

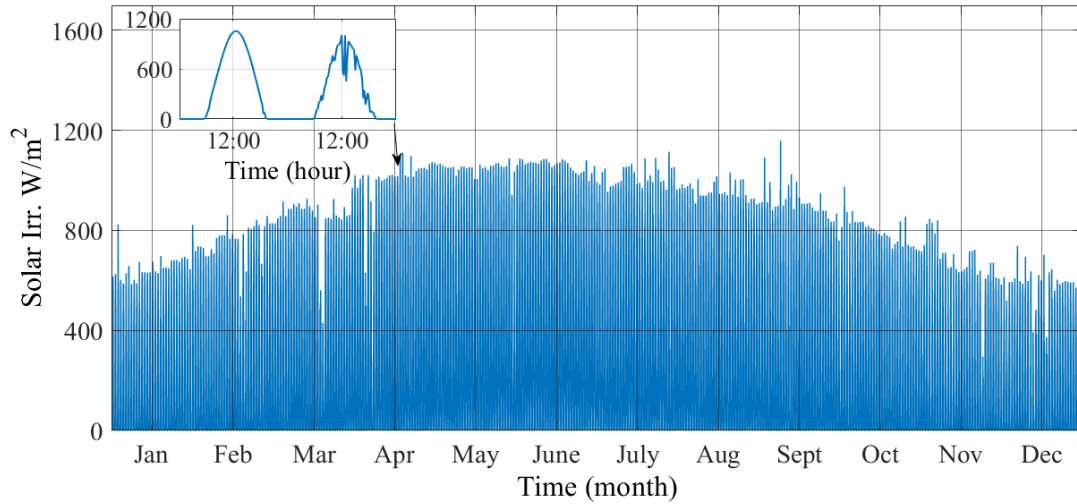


(a)

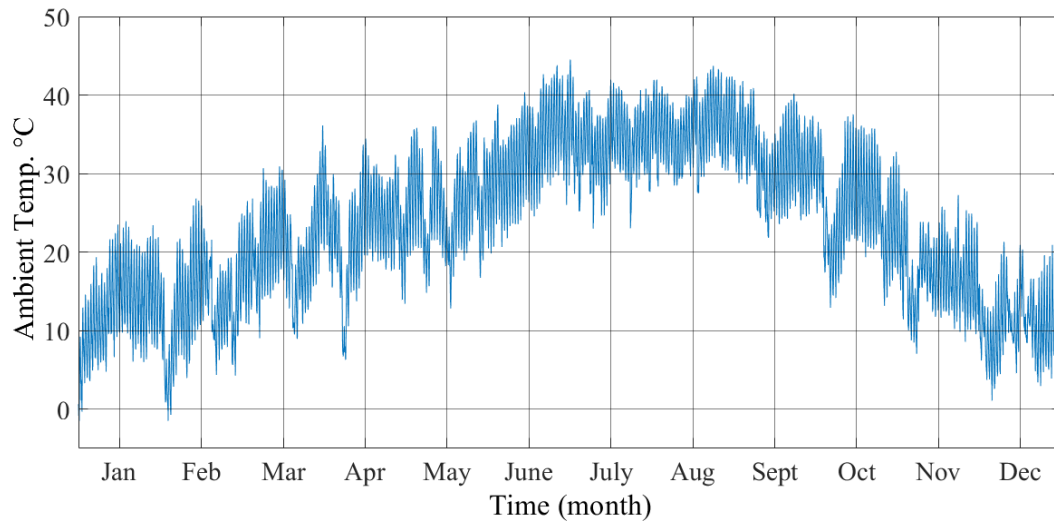


(b)

Figure 2.16. Lookup table of the IGBT device thermal performance with active and reactive power supplies at $T_a = 25^\circ\text{C}$: (a) total losses, and (b) junction temperature.



(a)

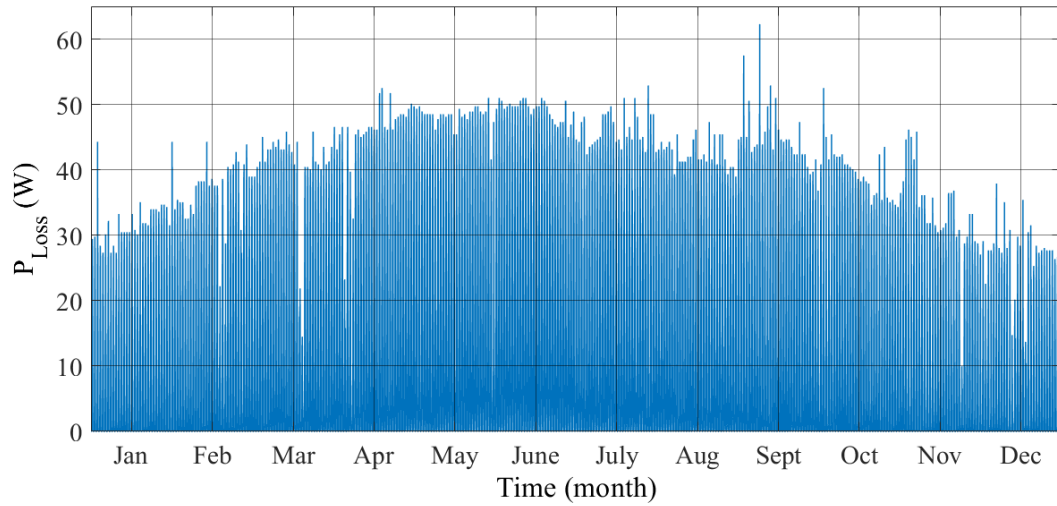


(b)

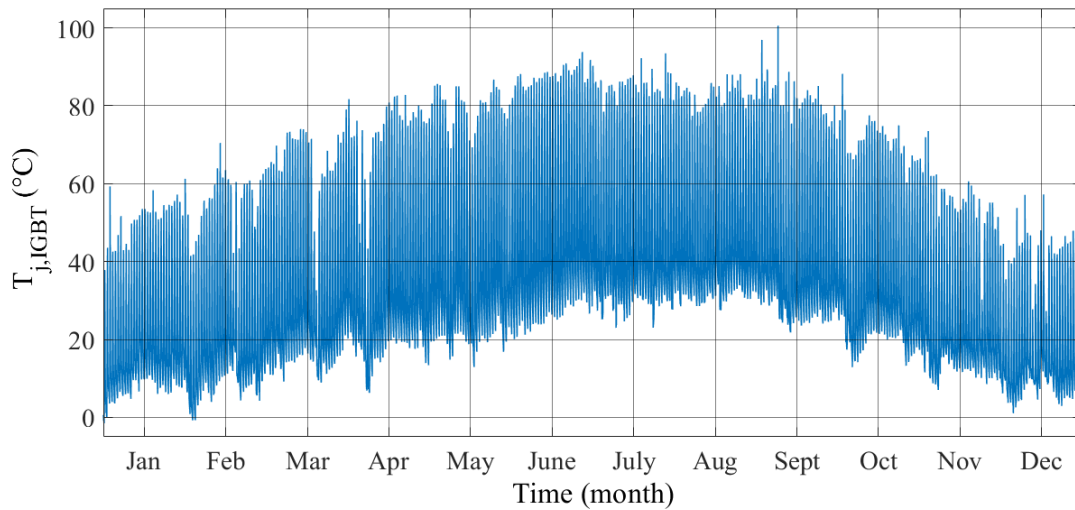
Figure 2.17. Yearly mission profiles (15 min per sample): (a) solar irradiance, and (b) ambient temperature.

The thermal model was used to calculate the loss and junction temperature in inverter switches. As previously mentioned, the PV inverter was not used to regulate the voltage and only supplied active power in this case. The amplitude of the power loss and junction temperature throughout the cycle are shown in Fig. 2.18. Both profiles follow the output active power of the PV inverter and the ambient temperature. In this chapter, the controller of the

inverter was based on nonreactive power compensation because the distribution system and load profile were not included. Therefore, the required amount of reactive power from the inverter was not known.



(a)



(b)

Figure 2.18. Yearly profiles from the thermal model of the IGBT device in a PV inverter: (a) power loss, and (b) junction temperature.

To investigate the effect of temperature variations on inverter lifetime, the rainflow algorithm was applied to extract the values for ΔT_j and T_m in the continuous temperature cycles to be used in the damage analysis. The distribution of the temperature cycles extracted from the rainflow algorithm is shown in Fig. 2.19. Most of the temperature cycles are concentrated in the range (ΔT_j) of 0-10°C. This is due to the loading profile resulting from the solar irradiance and ambient temperature variations. The Coffin-Manson-Arrhenius model was used to calculate the number of cycles to fail for each temperature cycle. According to the IGBT manufacture’s reliability data, the equivalent device hours are 1,900,000 [149]. This can be used to estimate the module parameters A and α as 10 and -4 respectively [150]. To find the accumulated damage of IGBT devices in the PV inverter for the given temperature profile, the

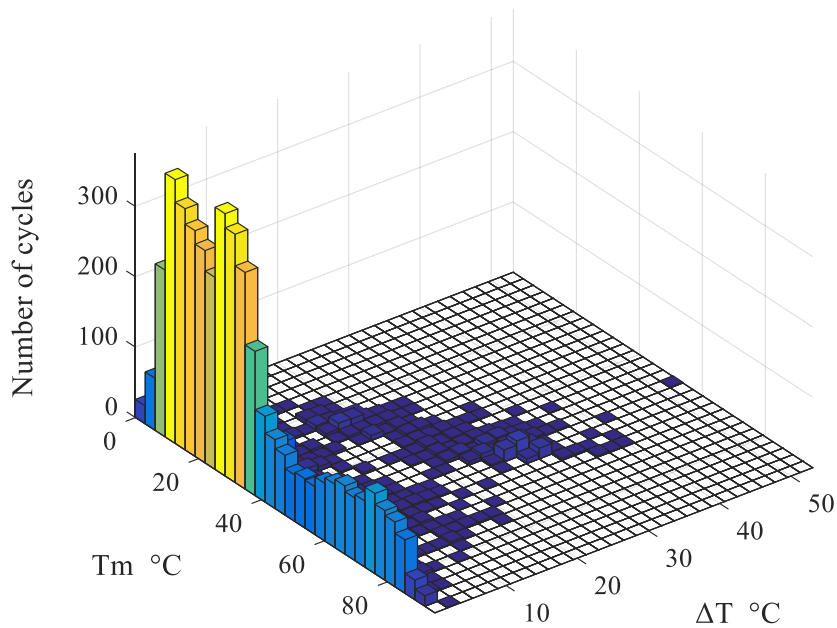


Figure 2.19. Rainflow counting of the junction temperature profile.

Palmgren-Miner linear rule was used. The accumulated damage to the inverter switches was 0.0045. In other words, the degradation rate was 0.45%/year in the given loading profile.

The inverter degradation rate was calculated in the case of supplying active power, which will be used in Chapter 4 in comparison with the case of supplying both active and reactive power. The lifetime of a PV inverter is affected by many other factors, such as cables and capacitors. However, this work only considers inverter packaging failure related to junction temperature variations.

2.4 Conclusion

This chapter described the PV inverter control and lifetime estimation methods used in this work, providing a detailed discussion of (1) inverter control, (2) the reliability of inverters, (3) the causes of inverter failure, and (4) the rainflow algorithm for inverter lifetime estimation. The current-control method for VSI in the grid-connected mode will be used in Chapters 3, 4, and 5. The inverter lifetime estimation method will be applied in Chapters 4 and 5. A case study was presented that investigated the effect of temperature variations on inverter lifetime.

3 Distributed Generation Synchronization with a Distorted or Weak Grid

3.1 Introduction

The operation of a DG requires knowing the voltage amplitude and phase to perform several control tasks, such as synchronization, islanding detection, and power flow control. In a weak grid, the voltage suffers from distortion and harmonics due to nonlinear loads that can corrupt the synchronization process. The operation of a power-electronics-interfaced DG system might be interrupted by transient disturbances in the power system. Therefore, fast and accurate tracking of the fundamental frequency and generating the reference signal are essential in the synchronization process. In addition, the controller of the DG should provide the capability to ride through faults to avoid tripping during transient events.

The phase-locked-loop (PLL) method is widely used to synchronize both conventional generators and power-electronics-interfaced DGs with the grid. The PLL-based method is used to track the angle of the fundamental voltage [67]. The PLL algorithm is simple and provides a superior performance at ideal conditions when the total harmonic distortion of the grid voltage is very low [68]. A significant amount of research has been conducted to address the potential limitations of the synchronization methods related to performance and the capability of rejecting undesired harmonics [8], [9], [69]. Some of these attempts have considered improving the performance of the synchronization methods in polluted networks without sacrificing the robustness of the PLL method against distorted voltages [37], [70].

The synchronous reference frame (SRF) phase-locked-loop (SRF-PLL) method is the most widely used in power-electronics-interfaced distributed generation systems [43], [71], [72]. In weak grids, however, a simple SRF-PLL may fail to extract the accurate angle of the fundamental voltage and rejecting harmonics. To overcome this problem, a prefilter stage can be used along with the PLL to provide a capability sufficient to reject harmonics [67]. Several prefilter delayed signal cancelation (DSC)-based techniques, along with the PLL, have been proposed to extract the fundamental component from a distorted voltage signal [68], [73], [74]. A DSC-PLL algorithm has been proposed to detect voltage variation [75]. Therefore, corrective action can be initiated to control the voltage by injecting or absorbing reactive power into the grid. A stationary reference frame PLL with a generalized delayed signal cancelation (GDSC) prefiltering algorithm for detecting the fundamental frequency component in unbalanced three-phase applications has been employed in [76]. The prefilter tightens the bandwidth of the PLL loop filter, which aids in rejecting the harmonics and noise but at the cost of a slow dynamic response. In addition, some of these methods work in attenuating harmonics without canceling them, especially, the odd harmonics.

The implementation of digital filtering methods along with the PLL is highly promising in the synchronization process. A recursive discrete Fourier transform (DFT) filter has been employed to extract the amplitude and frequency of the input signal [77]. However, recursive DFT requires high computational effort, which may not be suitable for the real-time implementation of the synchronization process. The sliding discrete Fourier transform (SDFT) has been used to calculate the spectrum of a signal [78]. The SDFT has lower computational complexity in comparison to either the recursive DFT or a fast Fourier transform (FFT).

In this chapter, the SDFT was developed to estimate the amplitude of the grid voltage accurately and to detect the phase for the ensuing synchronization. Section 3.2 reviews the structure of the single-phase microgrid, the control algorithm, and the performance of the conventional SRF-PLL in distorted conditions. Section 3.3 presents the proposed synchronization method. Simulation results are presented in Section 3.4. The contribution and conclusion of this study are included in Sections 3.5 and 3.6, respectively.

3.2 Phase-Locked Loop Technique

In this section, the structure of the single-phase microgrid and the control algorithm is reviewed before discussing the implementation of the SRF-PLL method for grid synchronization. In the interconnected mode, the main grid represents the stiff source and provides the reference voltage and frequency to the DG; the inverter is operated with a current control method (CCM) to control the output current of the DG, which ultimately results in controlling the output active and reactive power based on system requirements. Fig. 3.1 displays a single-phase inverter-interfaced DG with the grid and the control overview. A detailed description of the control scheme is given in Section 2.1.

The SRF-PLL is widely used for grid synchronization, especially in single-phase systems because the grid voltage (v_{grid}) can be transformed to a stationary reference frame ($\alpha\beta$) by creating an orthogonal signal to emulate the Clark transformation, as follows:

$$v_{\alpha} = v_{grid} = V_m \cos \theta \quad (3.1)$$

$$v_{\beta} = V_m \sin \theta \quad (3.2)$$

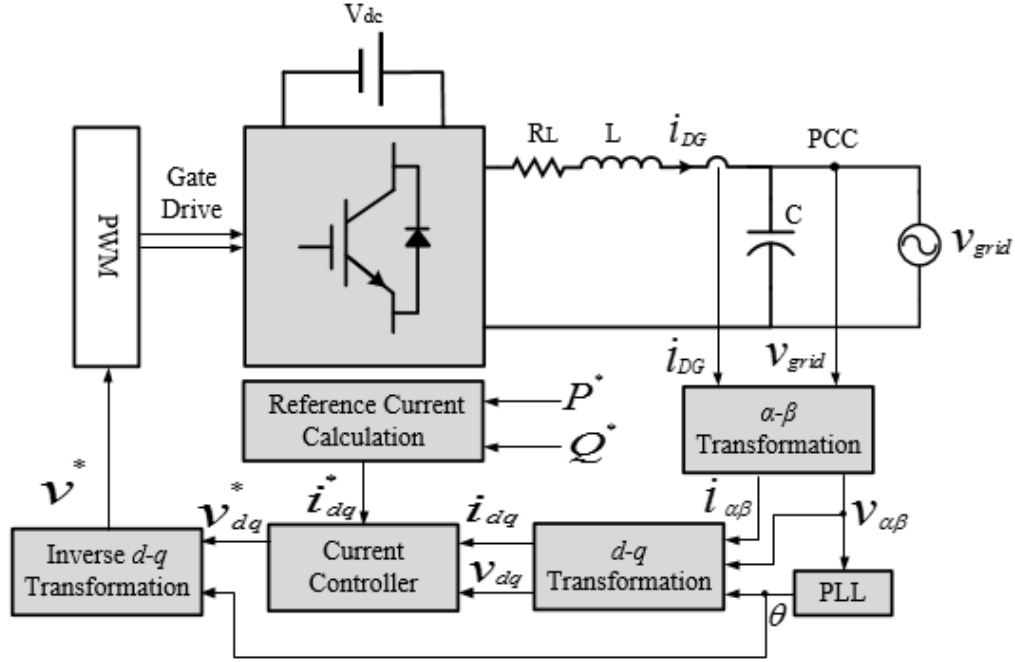


Figure 3.1. Grid-connected microgrid and the control overview.

Then, the Park transformation ($\alpha\beta \rightarrow dq$) is applied to obtain the synchronous reference frame, as follows:

$$\begin{bmatrix} v_d \\ v_q \end{bmatrix} = \begin{bmatrix} \cos \hat{\theta} & \sin \hat{\theta} \\ -\sin \hat{\theta} & \cos \hat{\theta} \end{bmatrix} \cdot \begin{bmatrix} v_\alpha \\ v_\beta \end{bmatrix} \quad (3.3)$$

where $\hat{\theta}$ is the PLL output. The single-phase PLL is similar to the three-phase case, which was explained in detail in Section 2.1. A conventional SRF-PLL unit consists of three main parts, a phase detector (PD), loop filter (LF), and voltage controlled oscillator (VCO). Most of the PLL algorithms in the literature share the same LF and VCO parts, while most of the contributions have improved the PD component [71], [79]. Fig. 3.2 shows the block diagram of a conventional SRF-PLL. Under a steady-state condition, while the phase difference $\delta = \theta - \hat{\theta}$ is very small, the phase error (e) can be represented as [8]

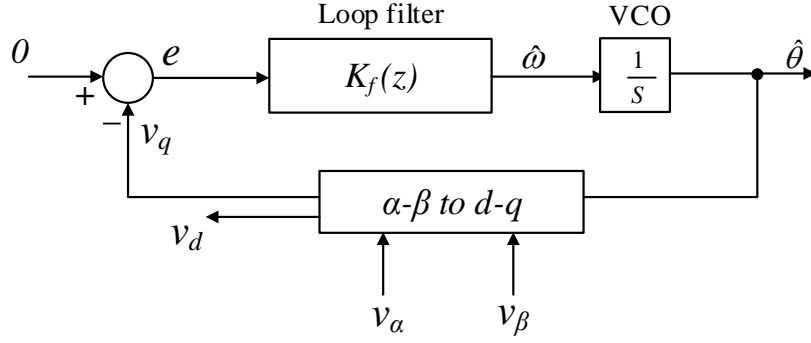


Figure 3.2 Synchronous reference frame PLL.

$$e = V_m \delta. \quad (3.4)$$

If the loop filter is properly designed, the PLL can accurately track the grid frequency ω and the phase angle θ . The PI controller is commonly used for the loop filter, which is given by

$$K_f(s) = K_p \frac{1 + s\tau}{s\tau} \quad (3.5)$$

where K_p and K_p/τ are the filter proportional and integral gains, respectively. Considering the closed loop system, the second-order transfer function can be rewritten in the general form as

$$H(s) = \frac{s^2}{s^2 + 2\zeta\omega_n + \omega_n^2} \quad (3.6)$$

where the bandwidth $\omega_n = \sqrt{K_p V_m / \tau}$ and the damping ratio $\zeta = \sqrt{\tau K_p V_m} / 2$.

In the presence of nonlinear loads, the grid voltage signal can be distorted by higher harmonics that might affect the operation of the PLL. Therefore, when tuning the loop filter parameters, the performance of the PLL in a distorted grid should be taken into account. Consider the single-phase voltage grid (v_{grid}), as follows:

$$v_{grid} = V_1 \cos(\theta) + V_3 \cos(3\theta) + V_5 \cos(5\theta) + V_7 \cos(7\theta) + \dots \quad (3.7)$$

where $V_1, V_3, V_5, V_7, \dots$ are the voltage magnitude of the harmonic components. The q -axis voltage can be found from (3.3) as [71]

$$v_q = V_1 \delta + (V_3 - V_5) \sin(4\theta) + (V_7 - V_9) \sin(8\theta) + \dots \quad (3.8)$$

Comparing (3.4) and (3.8), the phase difference (δ) correspond to the voltage harmonics can expressed as

$$\delta = \frac{(V_3 - V_5)}{V_1} \sin(4\theta) + \frac{(V_7 - V_9)}{V_1} \sin(8\theta) + \dots \quad (3.9)$$

Most of the PLL types are classified based on the prefilter stage method. The dynamic performance of the PLL should be taken into consideration when designing the proportional-integral (PI) controller to allow for both fast and accurate tracking of the phase. However, a higher bandwidth would increase the tracking error. On the other hand, low bandwidth would degrade the dynamic response. Therefore, PI controller tuning requires a compromise between a good dynamic response and accurate tracking [80]. A prefilter stage using an SDFT filter can eliminate the harmonics from the signal to improve the PLL performance without sacrificing its good characteristics.

3.3 Sliding Discrete Fourier Transform Phase-Locked-Loop

The SDFT filter has been used for online spectrum analysis to extract accurate fundamental signal amplitude and harmonics at any frequency [81]. As shown in Fig. 3.3, the SDFT filter consists of two cascaded digital filters and a comb filter, followed by a second-

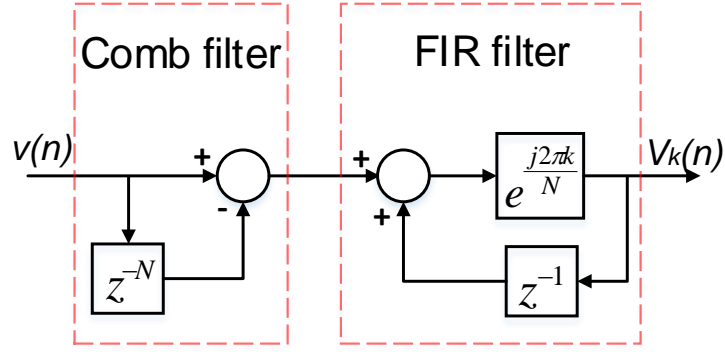


Figure 3.3. SDFT filter structure.

order finite impulse response (FIR). Within a sliding window, the SDFT algorithm performs an N -point DFT on time samples to analyze the harmonic components of a periodic signal. The SDFT algorithm calculates a single DFT bin (k), centered at a normalized frequency of $2\pi k/N$, by shifting the original signal by one sample, as shown in Fig. 3.4. Due to the comb filter delay of N , the output of the SDFT filter will not reach the steady-state until N input samples of the periodic signal have been calculated. The number of samples (N) is a function of the cycle time (T_1) and sampling time (T_p) and can be found as follows:

$$N = \frac{T_1}{T_p} \quad (3.10)$$

The main advantages of the SDFT are its simple structure and its ease of implementation in real time, which served as the motivation to develop the SDFT-PLL for grid synchronization in this research. The z -domain transfer function of the SDFT can be described as

$$H_{SDFT}(z) = \frac{e^{j2\pi k/N}(1 - z^{-N})}{1 - e^{j2\pi k/N}z^{-1}} \quad (3.11)$$

where k is an integer number representing the k^{th} harmonic.

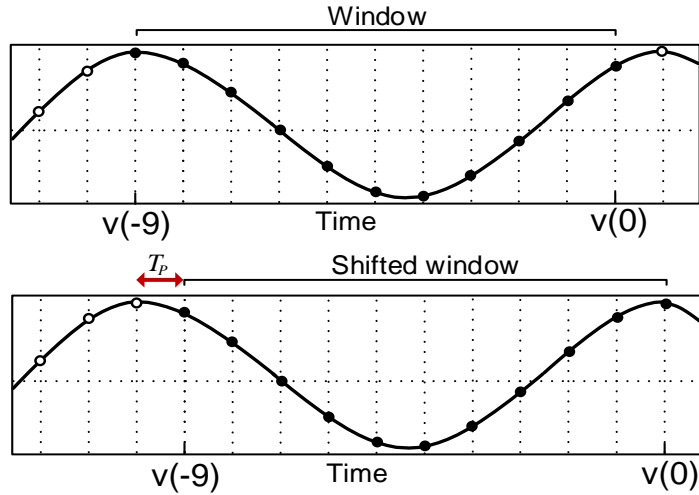


Figure 3.4. Window signal sampling for a 10-point SDFT.

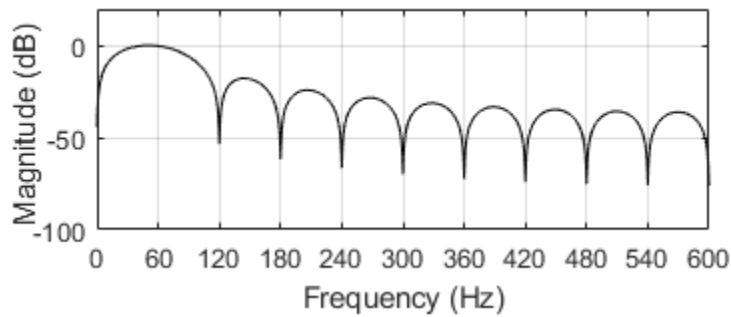


Figure 3.5. Frequency response of the SDFT filter for $N = 18$.

The SDFT filter can accurately extract the fundamental cyclic frequency of the grid when the SDFT time window N matches the grid frequency. Assuming N of the SDFT filter is designed for a grid frequency of 60 Hz, the filter would provide accurate extraction of the fundamental frequency of 60 Hz from the distorted signal. When v_{grid} is fed to the SDFT block with $k = 1$ (tuned to a nominal grid frequency, ω), it will reject the harmonics and extract the fundamental component. The frequency response of the SDFT filter for $N = 18$ is shown in Fig. 3.5.

It is evident from (3.11) that the output of the SDFT filter consists of real and imaginary parts. The real part is in-phase with the input, while the imaginary part is the orthogonal component. This is very useful in the implementation of SRF-PLL because performing a dq transformation requires both signals ($\alpha\beta$), which is one of the main advantages of using the SDFT with the PLL in single-phase systems. Fig. 3.6 displays the block diagram of the SDFT for fundamental component extraction, where θ_k can be obtained as

$$\theta_k = \frac{2\pi k}{N}. \quad (3.12)$$

The SDFT is marginally stable because the poles are located on the unit circle of the z -domain, as shown in Fig 3.7. Therefore, a damping factor r can be introduced to the SDFT

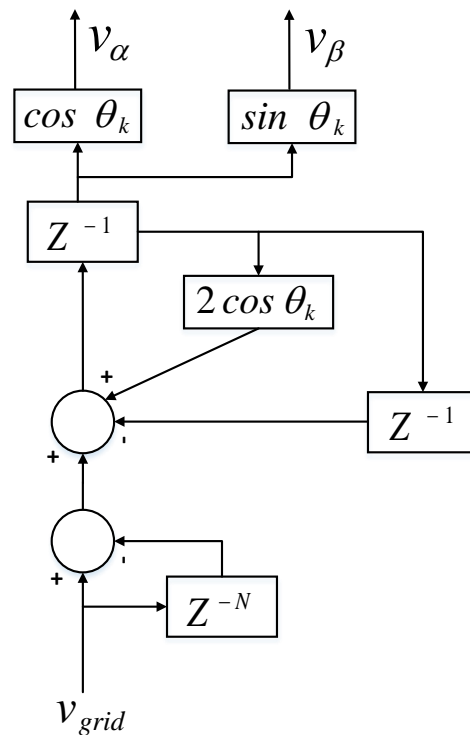


Figure 3.6. SDFT filter for fundamental component extraction.

transfer function to move the filter's pole inside the unit circle [7]. In the modified transfer function below

$$H_{SDFT}(z) = \frac{r e^{\frac{j2\pi k}{N}} (1 - r z^{-N})}{1 - r e^{j2\pi k/N} z^{-1}} \quad (3.13)$$

r must be less than unity (but very close) so that introducing this factor does not result in large errors in the magnitude and phase of the output signal. However, the selection of r and its effect on the error should be investigated for each case. In this study, $r = 0.999$ was selected.

3.4 Simulation Results

The synchronization technique based on the SDFT-PLL was tested using the system shown in Fig. 3.1. The simulation was conducted using MATLAB/Simulink. System parameters are given in Table 3.1. The grid voltage signal contains the fundamental frequency

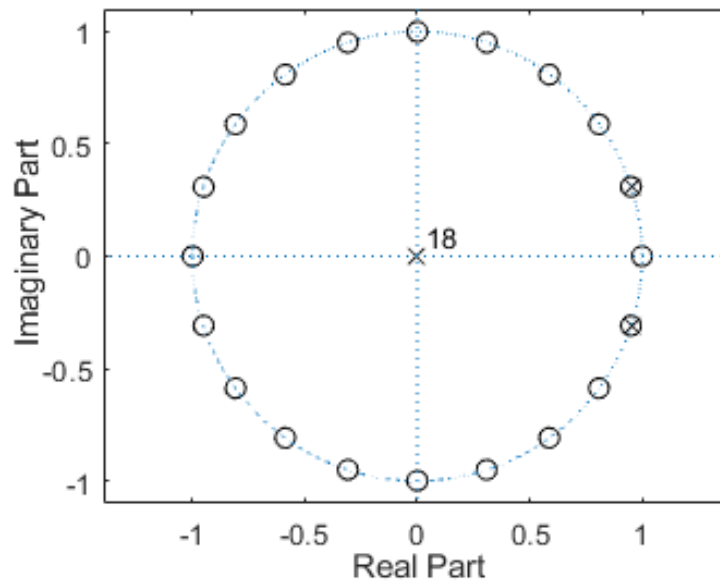


Figure 3.7. Pole-zero plot for the SDFT filter for $k = 1$, $N = 18$.

as well as the third, fifth and seventh harmonics. Fig. 3.8 shows the signal voltage before and after the harmonic elimination by the proposed method. It is obvious that the SDFT filter can accurately extract the voltage fundamental component (60 Hz), and the resultant signal is a pure sinusoidal wave.

Table 3.1. System parameters.

Grid voltage	$150 \sin(2\pi 60t) + 12 \sin(3 * 2\pi 60t) + 4 \sin(5 * 2\pi 60t) + 2 \sin(7 * 2\pi 60t) V$
Feeder impedance	$0.5 + j0.37 \Omega$
Inductor filter	5mH
Resistor filter	0.1 Ω
Load	1 kW
DC link voltage	300 V _{dc}
Switching frequency	10 kHz
SRF-PLL loop filter	$k_p = 1.5, \tau = 0.0072$
SDFT-PLL loop filter	$k_p = 20, \tau = 0.0053$

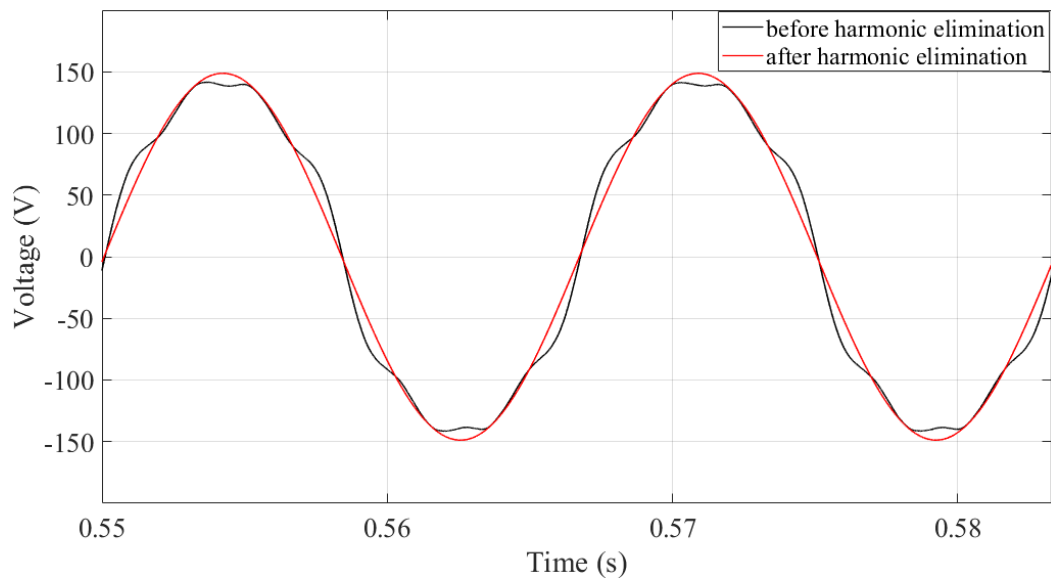


Figure 3.8. Voltage signal before and after harmonic elimination by the SDFT filter.

The performance of the SDFT-PLL with the distorted grid condition was evaluated in comparison with the results of the SRF-PLL. Figs. 3.9 and 3.10 show the frequency and phase error output of the SDFF-PLL and SRF-PLL, respectively. The SDFT-PLL showed a faster response compared to the SRF-PLL. The settling time was 0.02 s for the SDFT-PLL and 0.06 s for the SRF-PLL. The fast dynamic response was due to the wider bandwidth of the SDFT-PLL (377 rad/s), while the bandwidth of the SRF-PLL was chosen to be 188 rad/s to reduce the tracking error in the case of distorted voltage. The overshoot of frequency for the SDFT-PLL was higher by 30% compared to the SRF-PLL due to the fast response; however, the settling time was lower when using the SDFT-PLL. The ripples in the frequency and the phase error output of the SRF-PLL will be analyzed in the next case.

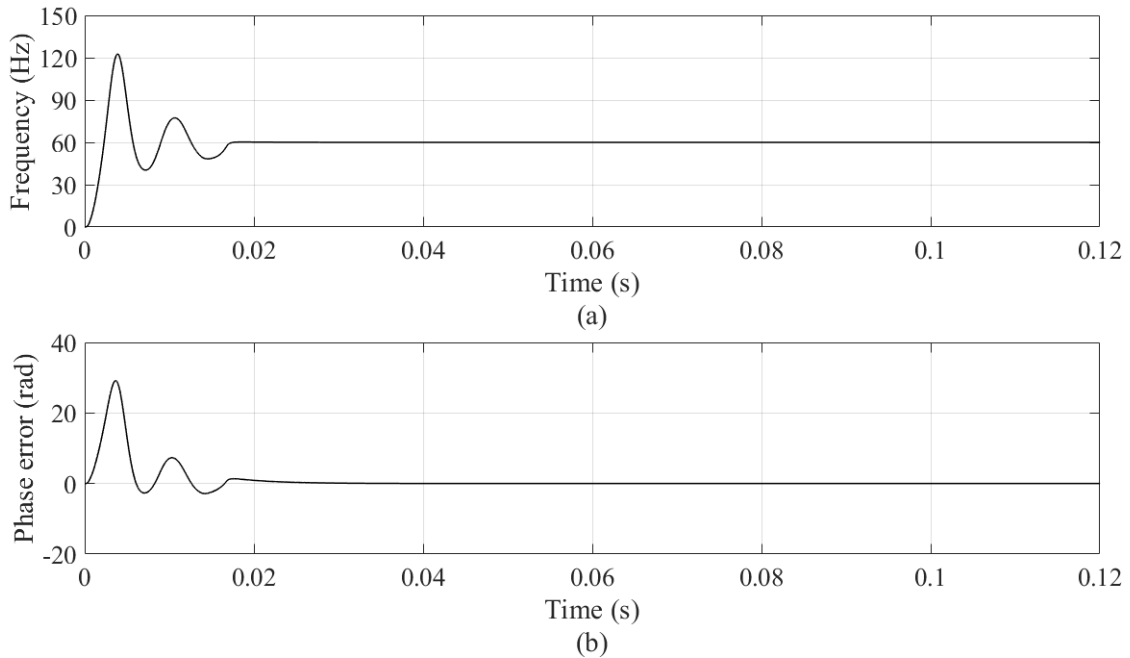


Figure 3.9. Dynamic performance of the SDFT-PLL.

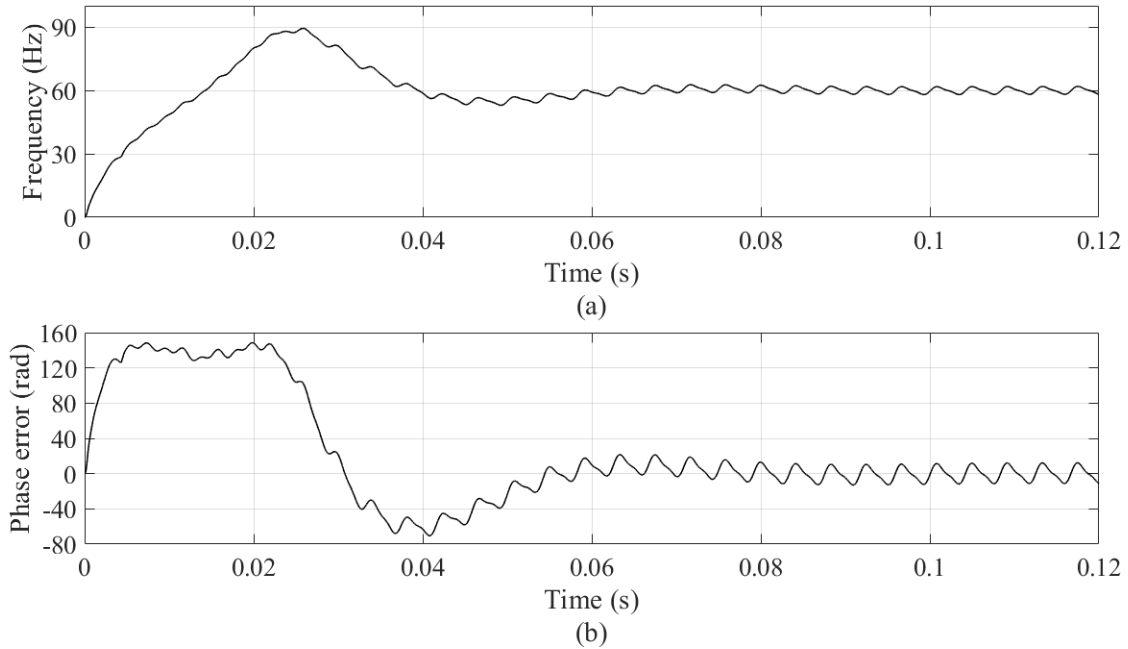


Figure 3.10. Dynamic performance of the SRF-PLL.

In the second simulation, the performance of the proposed method in eliminating harmonics was analyzed. Fig. 3.11 illustrates that the utility voltage with harmonic components caused ripples in the frequency and the phase error output of the SRF-PLL. The odd harmonics of the grid voltage appeared as even harmonics in the phase error with frequency components of 4ω and 8ω in the q -axis voltage as given by (3.9) and shown in Fig. 3.12. At $t = 0.6$ s, the SDFT filter was activated to eliminate harmonic components before feeding the voltage measurement into the PLL. The SDFT filter effectively removed the harmonics, which resulted in eliminating the ripples in the frequency and the phase error output of the SDFT-PLL. Therefore, the SDFT-PLL is more accurate in tracking the phase and frequency of the grid in a distorted condition compared to the SRF-PLL, due to its poor capability in rejecting the harmonics.

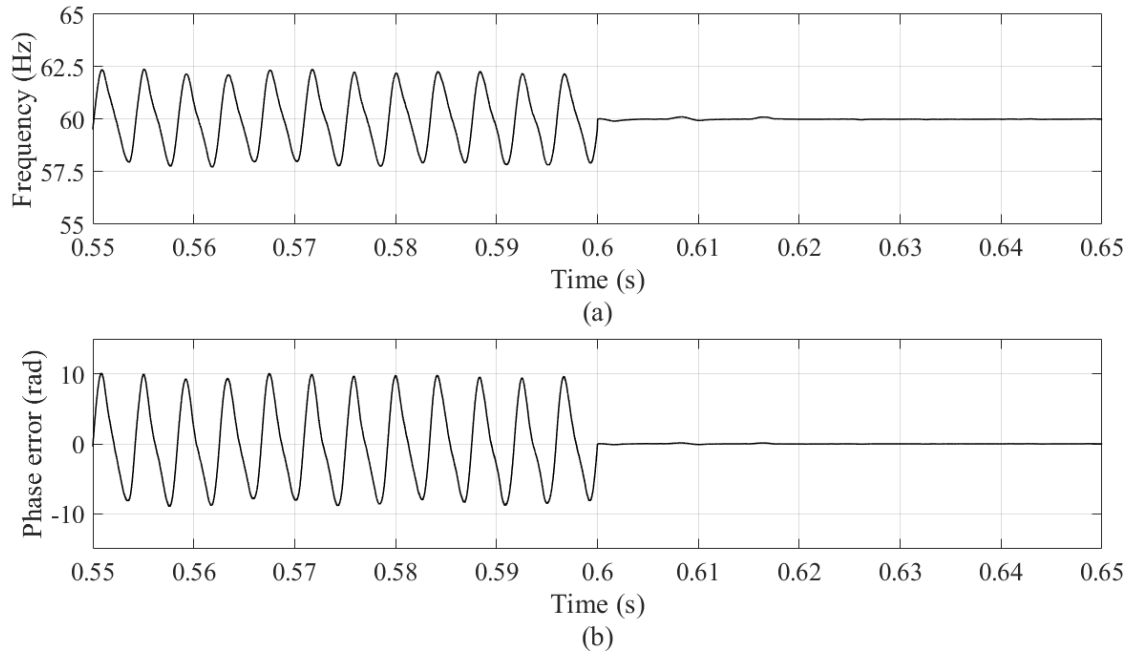


Figure 3.11. Simulation results for the harmonic elimination effect on the frequency and phase error estimation (SDFT prefilter, enabled at $t = 0.6$).

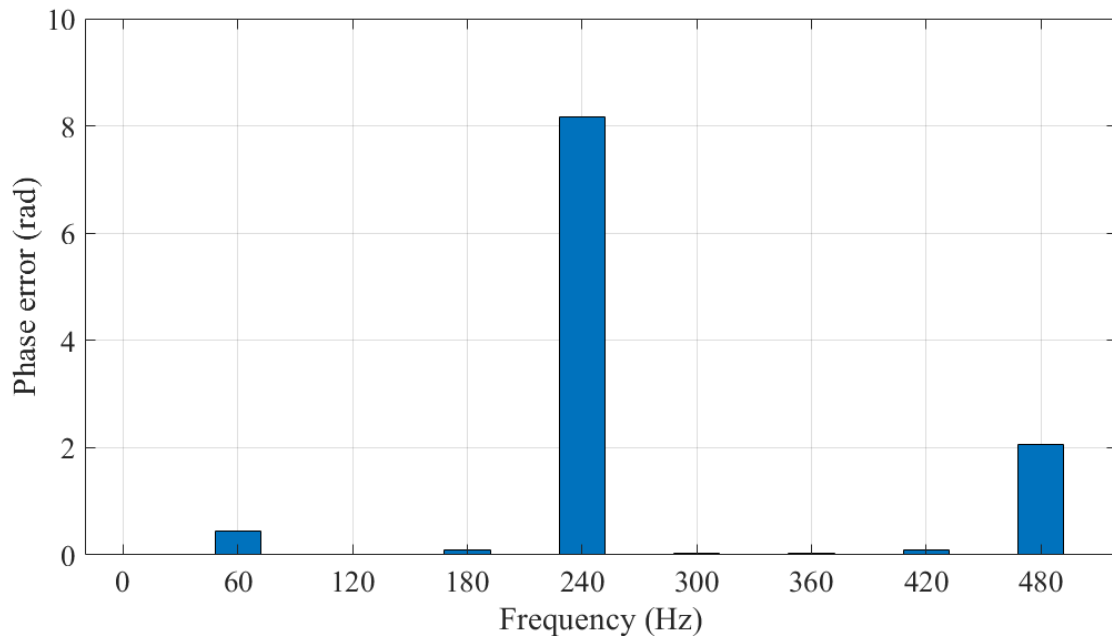


Figure 3.12. Harmonic components of the phase error for the SRF-PLL.

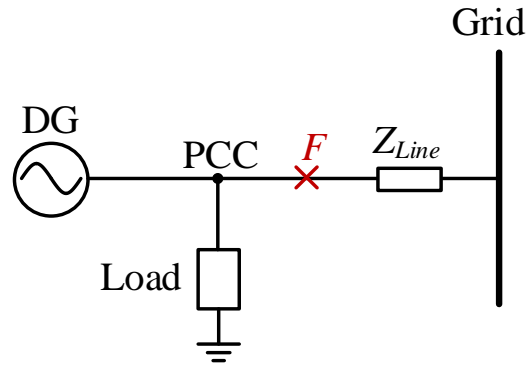


Figure 3.13. Simple distribution feeder with fault at node F .

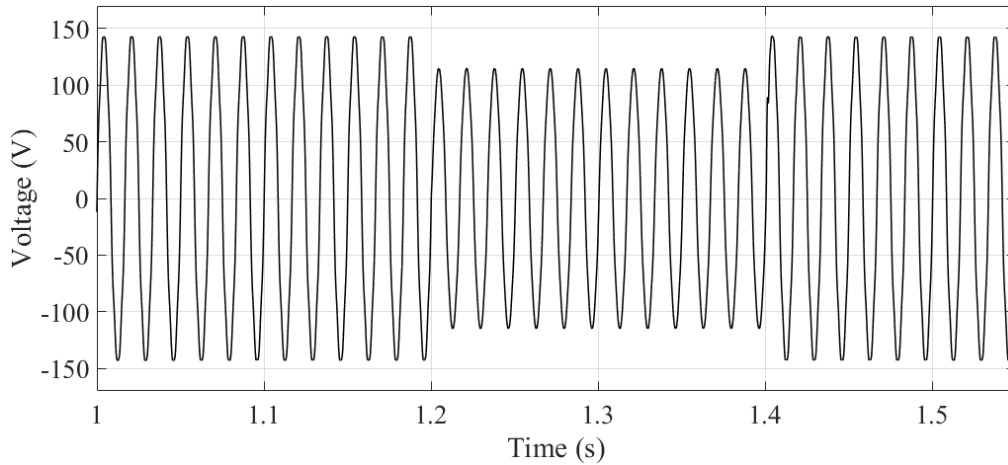


Figure 3.14. Voltage at the PCC with the grid in fault condition (fault applied at $t = 1.2$ s and cleared at $t = 1.4$ s).

In the third simulation, the dynamic performance of the SDFT-PLL was tested in the case of a phase-to-ground fault for the single-phase system to investigate the robustness of the SDFT-PLL in withstanding disturbance. The fault was applied to the distribution feeder at node F , as shown in Fig. 3.13, at $t = 1.2$ s and was cleared at $t = 1.4$ s. The fault resulted in a voltage sag condition of 25% at the point of common coupling (PCC), as shown in Fig. 3.14. The frequency and phase error output of the SRF-PLL and SDFT-PLL in the fault condition are shown in Figs. 3.15 and 3.16, respectively. The simulation results demonstrated that the

SDFT-PLL had a better performance in terms of frequency and phase error and reached the steady-state condition faster than the SRF-PLL during the fault event. In other words, the SDFT-PLL showed a good dynamic performance with disturbance rejection for riding through a fault. The settling time was 0.025 s for the SDFT-PLL and was 0.05 s for the SRF-PLL during the fault condition and after fault removal. The fast dynamic response was due to the wider bandwidth of the SDFT-PLL (377 rad/s), which was double the bandwidth of the SRF-PLL (188 rad/s). In addition, eliminating the harmonic components in the voltage signal by applying the SDFT filter resulted in removing the ripple in the phase error and frequency, which eventually led to accurate tracking.

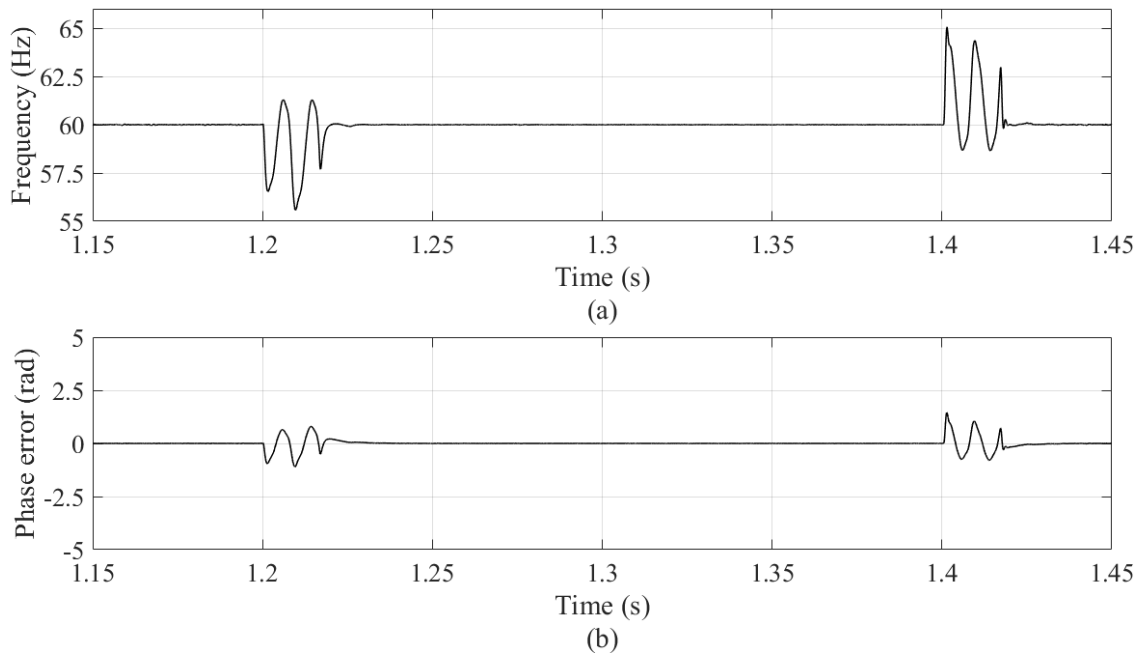


Figure 3.15. Frequency and phase error estimation from the SDFT-PLL in the fault condition.

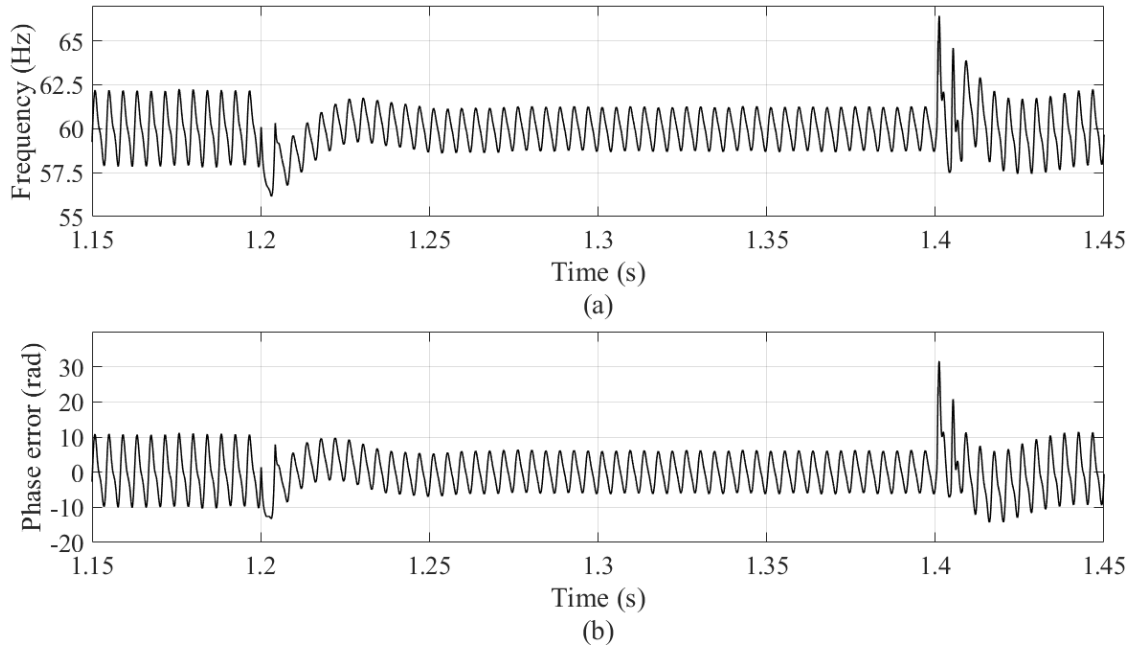


Figure 3.16. Frequency and phase error estimation from the SRF-PLL in the fault condition.

Table 3.2 Performance comparison between the SRF-PLL and SDFT-PLL.

	SRF-PLL	SDFT-PLL
Harmonic rejection capability	Low	High
Steady-state error	High	Low
Dynamic response	Average	Fast
Computational burden	Low	High

Table 3.2 summarizes the results of the performance comparison study based on the simulation results for the SRF-PLL and SDFT-PLL methods. The PLL benefits from the SDFT filtering capability, which resulted in a high harmonic rejection capability. Harmonic elimination by the SDFT-PLL allowed for operating at higher bandwidths to improve the dynamic performance during network disturbances. The fast and accurate tracking of system

frequency and voltage is necessary in order to support the grid under fault condition to avoid DGs tripping.

The SDFT-PLL showed an overall improvement of performance in comparison to the SRF-PLL at the cost of higher computational complexity. For the SDFT with $N = 20$, the required number of multiplications and additions increased by 80 in comparison to the SRF-PLL.

3.5 Contribution

- A harmonic elimination method was proposed for single-phase distributed generation synchronization with a distorted grid.
- The proposed method incorporates the SDFT method in the SRF-PLL prefiltering stage to remove the effect of harmonics from the input voltage.
- The SDFT method allows for a lower steady-state error. Therefore, the SDFT-PLL can operate at higher bandwidths to improve the dynamic performance during network disturbances.
- Simulation results were presented to validate the performance of the SDFT-PLL in a distorted grid.

3.6 Conclusion

This chapter presented the SDFT-PLL method to achieve an accurate synchronization of single-phase inverter-interfaced DGs with a weak or distorted grid. The SDFT was incorporated into the SRF-PLL method as a prefilter for the harmonics of the input voltage. By

eliminating harmonic components of the voltage signal, which are the main sources of the steady-state error, the PLL filter loop can be designed in such a way that it allows for higher bandwidth to improve dynamic performance. Simulation results were presented to evaluate and compare the performance of the SDFT-PLL and SRF-PLL methods in synchronizing a single-phase DG with the grid. The SDFT-PLL operated more accurately in tracking the frequency in both steady-state and fault conditions. The overall dynamic performance was improved with the use of the SDFT-PLL compared with the conventional SRF-PLL. In addition, it was shown that the SDFT-PLL is capable of rejecting harmonics and withstanding disturbances.

4 Volt/Var Control in Distribution Networks Considering Inverter Utilization

4.1 Introduction

In the past, the operation of distribution networks received the least amount of attention from power system planners and developers, such that most of the distribution network actions were done manually by operators, including load restorations after faults, setting the on-load tap-changer (OLTC) of distribution transformers, and energizing or de-energizing capacitor banks. Currently, most distribution networks are blind spots in the power system because of the lack of communication channels between network elements and the energy management center. The cost of adding communications is prohibitive due to the large number of distribution transformers that are geographically scattered and also because of the length of the feeders. In addition, the need for information exchange within the existing distribution networks is minimal due to the convenient configuration of the feeders, which allows only unidirectional power flow, and the simplicity of forecasting local loads, which follows seasonal patterns and weather.

Migration from conventional centralized generation to renewable energy distributed generation (REDG) is challenging because the latter is intermittent and decentralized. Cloud passing causes significant voltage fluctuations, especially when the PV penetration is high. Also, at high PV penetration levels, high feed-in and reverse power occur under light load conditions. This high reverse power could lead to overvoltage at the end of the distribution feeder, resulting in a voltage violation that must be limited to within ± 0.05 p.u. per ANSI C84.1, standard Range A service voltage [10].

The level of PV penetration in a power system can have different definitions depending on the perspective from which it is viewed. In this work, the level of PV penetration from a distribution system's perspective is expressed as follows:

$$PV \text{ Penetration} = \frac{\text{Total PV Capacity}}{\text{Peak Load of Distribution Feeder}} \times 100\% \quad (4.1)$$

As the level of PV penetration increases, the distribution network control needs to manage the intermittent changes in PV power production. High levels of PV penetration may be accompanied by voltage violations and reverse power flow, especially in residential distribution networks where the PV's maximum output power tends to occur before the peak time in a typical load profile.

Several approaches have been recommended to address the voltage rise issue. The impact of Volt/Var control was investigated in conventional distribution networks based on coordination between the OLTC and the substation capacitor, in the presence of DGs [82]. A decentralized Volt/Var control with dispatchable synchronous machine-based DG was proposed [83]. Reference [84] suggested a coordinated control of the distributed energy storage system that uses OLTC for voltage rise mitigation under high PV penetration. Energy storage can also provide a peak load shaving functionality and reduce distribution feeder power losses during the peak by 20%. Due to its random nature, PV is an intermittent source of energy that is not always available when it is needed. This increases the complexity of energy balancing between the local loads and PV generation in distribution networks. Conventional voltage regulation devices are not designed to operate in the presence of PVs and might not be capable of maintaining the voltage within the standard limit. Also, these devices suffer from mechanical and operational limitations. For example, OLTC is expected to provide 11 tap steps

per day in a typical distribution system [85]. However, in a distribution system with a high level of PV penetration, the number of OLTC tap steps can jump to 400, leading to extensive utilization [86].

Some of the literature has proposed installing new devices or upgrading distribution system configurations to address the voltage regulation issue. In [87], installing multiple voltage regulators is suggested for voltage regulation when connecting DGs to the main distribution feeder. The distribution network was upgraded from normally open loop to normally closed loop to integrate more DGs from a voltage regulation perspective [88]. The effect of replacing conventional feeder sectionalizers with a power electronics unit (e.g., back-to-back and multi-terminal converters) was investigated [89]. The main advantage of this approach is to allow a bidirectional exchange of active and reactive power between distribution feeder sections. As a result, higher levels of PV penetration can be integrated into distribution systems with improved voltage regulation. These approaches are not favorable due to an increase in the short-circuit level in distribution networks and the cost of upgrading the protection infrastructure.

The Volt/Var control architectures of distribution networks can be classified into two main categories: centralized and decentralized. In the decentralized method, only local measurements are required to perform the control strategy. A droop-based, local reactive power control method is proposed in [90] to prevent overvoltage in the distribution networks. In [15], online decentralized voltage control in distribution systems with multiple voltage regulating devices is proposed. This work is based on prioritizing the operation of DGs along with other voltage regulating devices to prevent conflict or simultaneous operation between these devices. To coordinate between these devices, time delay based on inverse time

characteristics are suggested when assigning priorities for the voltage regulating device operation. Decentralized Volt/Var control strategies in low voltage networks may lead to high reactive power flow due the presence of a high R/X ratio.

Droop-based active power curtailment techniques for overvoltage prevention were proposed [91]. This conservative control strategy considers only local information at the PCC, and it offers the option of sharing the power curtailment among all DGs by tuning the droop coefficients. Droop control can also provide a virtual inertia for DG interfaced with power electronics, thereby improving the disturbance rejection capability. However, over-practicing power curtailment eliminates the environmental and economic benefits of PV installations.

The installation of a communication system in the distribution network is an essential strategy in real-time centralized Volt/Var control to improve the hosting environment for a high level of PV. Bidirectional communication channels allow collecting watts, vars, and volts measurements to monitor and schedule PV production. A centralized reactive power compensation was proposed to regulate the voltage and reduce the power losses in the distribution networks using PV [92]. The proposed algorithm maintains the system requirements and helps to minimize the expected total cost of energy. Utilizing battery energy storage units for voltage regulating and peak load shaving in conjunction with DGs is suggested [93]. In addition, the system could be improved by minimizing the degradation of the battery units because the lifetime of batteries varies greatly depending on usage conditions. Yeh et al. [13] examined a multi-objective optimization problem to minimize the voltage variation and power losses in distribution networks. They proposed using adaptive weights for each objective function due to the difficulty of solving the multi-objective optimization problem. Unlike the transmission system, controlling the voltage in the distribution networks

is directly influenced by the complex power due to the presence of large R/X ratios in the distribution feeders. Therefore, adaptive real power capping was proposed for fair overvoltage mitigation when using a high penetration PV system [14]. A real power capping method (RPCM) is a combination of active power curtailment and reactive power management. Also, it considers the fair sharing of real power capping among the customers for voltage regulation. A stochastic reactive power management was considered to deal with renewable-based DG time-variability [24]. An online convex optimization was implemented to deal with the stochasticity of the DGs and loads. The cost of reactive power compensation was considered when regulating the voltage. Model predictive control (MPC)-based Volt/Var was applied to schedule the OLTC position, capacitor status, and output reactive power of the DG, depending on the forecast of the load, temperature, and clouds over the prediction horizon [16].

The control strategies so far have not considered the impact of Volt/Var on the reliability of PV inverter switches, which are the key elements in reactive power compensation. Compared to other components, inverter failures are the major cause of PV system outages according to a survey in [46]. The lifetime of PV inverters is influenced by cyclic temperature variations due to loading and ambient conditions [94]. Consequently, overusing PV inverters to exchange reactive power with the grid causes additional losses in the inverter switches, resulting in junction temperature increases, thus leading to a faster depreciation of the devices [20]. Therefore, junction temperature, which is associated with device losses, can be an integral part of a DER-based distribution system control strategy that considers the impact of inverter use on its lifetime and reliability.

In this chapter, a voltage control strategy is presented that includes solving for the optimal power flow to minimize both distribution system losses and the additional losses in

inverters switches caused by reactive power compensation. The main advantage of considering PV inverter use through inverter switching loss minimization is to reduce the thermal stress on the inverter's switches. This allows for optimal reactive power allocation among DGs because DG owners are not compensated for their inverter overutilization. The proposed strategy considers scheduling the output of the PV active power for a specific period of time. This time period is based on loads and the solar radiation forecast to conform with the advanced metering infrastructure (AMI) which is designed to send and receive periodic signals every 15 min. If voltage violations on one or more nodes are predicted, an optimal power flow solver is applied to allocate the reactive power among the DGs. Scheduling output real power for DGs is crucial for the economic dispatch of the distribution power system.

4.2 System Model

4.2.1 Distribution Network Model

In the main substation, several distribution feeders are connected to the lower voltage bus, and each feeder has multiple nodes to connect laterals through the secondary distribution transformers. In this study, a main distribution feeder with n number of nodes was employed, as shown in Fig. 4.1. To solve for the power flow, a well recognized power solver DistFlow was used [95]. The power flow equations are as follows:

$$P_{i-1} = P_i + r_i \frac{P_i^2 + Q_i^2}{V_i^2} - P_{Li} + P_{DG_i} \quad (4.2)$$

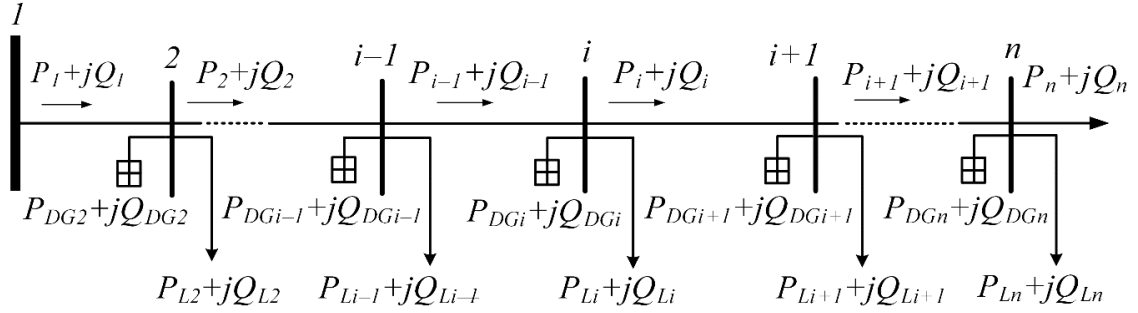


Figure 4.1. Schematic diagram of a radial distribution feeder with n nodes.

$$Q_{i-1} = Q_i + x_i \frac{P_i^2 + Q_i^2}{V_i^2} - Q_{Li} + Q_{DGi} \quad (4.3)$$

$$V_{i-1}^2 = V_i^2 + 2(r_i P_i + x_i Q_i) + (r_i^2 + x_i^2) \frac{P_i^2 + Q_i^2}{V_i^2} \quad (4.4)$$

where P_{DGi} and P_{Li} are the active power generation and load, respectively; Q_{DGi} and Q_{Li} are the reactive power generation and load, respectively; and V_i is the voltage magnitude at node i . The feeder section between nodes i and $i + 1$ is represented by the impedance of $r_i + jx_i$, and the complex power flow between these nodes is expressed as $P_i + jQ_i$.

After updating the voltage magnitude for all nodes and the complex power flow for all feeder sections, a forward sweep update is used to calculate the same variables but in the opposite direction, as follows:

$$P_{i+1} = P_i - r_i \frac{P_i^2 + Q_i^2}{V_i^2} - P_{Li} + P_{DGi} \quad (4.5)$$

$$Q_{i+1} = Q_i - x_i \frac{P_i^2 + Q_i^2}{V_i^2} - Q_{Li} + Q_{DGi} \quad (4.6)$$

$$V_{i+1}^2 = V_i^2 - 2(r_i P_i + x_i Q_i) + (r_i^2 + x_i^2) \frac{P_i^2 + Q_i^2}{V_i^2} \quad (4.7)$$

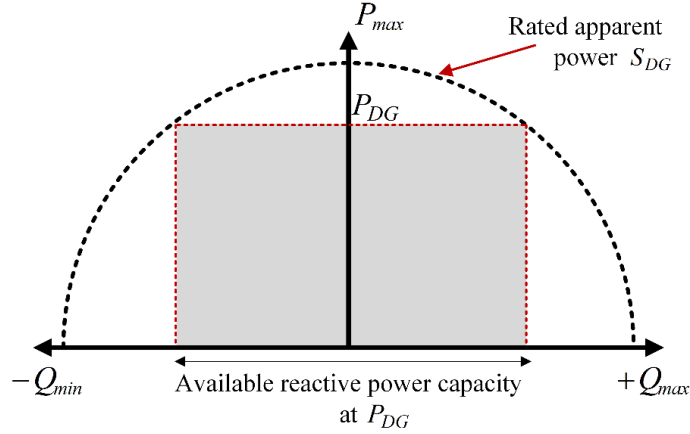


Figure 4.2. PV Inverter capability curve.

The purpose of this study is to regulate the voltage throughout the distribution network by managing the reactive power output of DGs. Minimizing the total power loss along the distribution feeder is one of the operating goals in the Volt/Var control strategy, which balances the economic and security objectives. The total power losses (P_{Loss}) in the distribution network is given by

$$P_{Loss} = \sum_{i=1}^n r_i \left(\frac{P_i^2 + Q_i^2}{V_i^2} \right). \quad (4.8)$$

4.2.2 Distributed PV Model

Distributed PV inverters are usually designed to generate the maximum active power with a unity power factor under normal conditions with maximum power point tracking (MPPT). However, the PV inverter controller provides a flexible capability to control the output real power by curtailing the active power or exchanging reactive power with the grid. The PV inverter output power is limited by the rated apparent power (S_{DG}) as shown in Fig. 4.2. Therefore, the available reactive power capacity ($Q_{DG,max}$) can be found as

$$Q_{DG,max} = \pm \sqrt{S_{DG}^2 - P_{DG}^2}. \quad (4.9)$$

One of the main goals of this research is to incorporate the thermal model of the PV inverter to estimate the additional losses in PV inverter switches that result from voltage regulation. The power losses in the power electronic devices are affected by the thermal impedance between the PV inverter temperature nodes and the ambient temperature. The thermal model of a PV inverter is explained in Section 2.2.

The additional inverter power losses related to supplying reactive power ($P_{loss,DG(Q)}$) can be found as follows

$$P_{loss,DG(Q)} = P_{loss,DG(P,Q)} - P_{loss,DG(P)} \quad (4.10)$$

where $P_{loss,DG(P,Q)}$ is total power losses in the inverter switches with active and reactive power supply, and $P_{loss,DG(P)}$ is total power losses in inverter switches with only active power supply.

4.3 Control Strategy

The central control unit that is the distribution system operator (DSO) in this work is located at the main substation. It monitors the demand, DG production, and voltages throughout the network. To gain the maximum advantage from the available measurements and communication using the centralized Volt/Var control strategy in case of voltage violation, power flow analysis must be performed to optimize the control variables in the distribution control. Fig. 4.3 shows the proposed Volt/Var control architecture in distribution networks. Depending on cyber and control resources, the DSO performed power flow based on the scheduled output power of the DG and the load forecast for each contiguous 15-minute

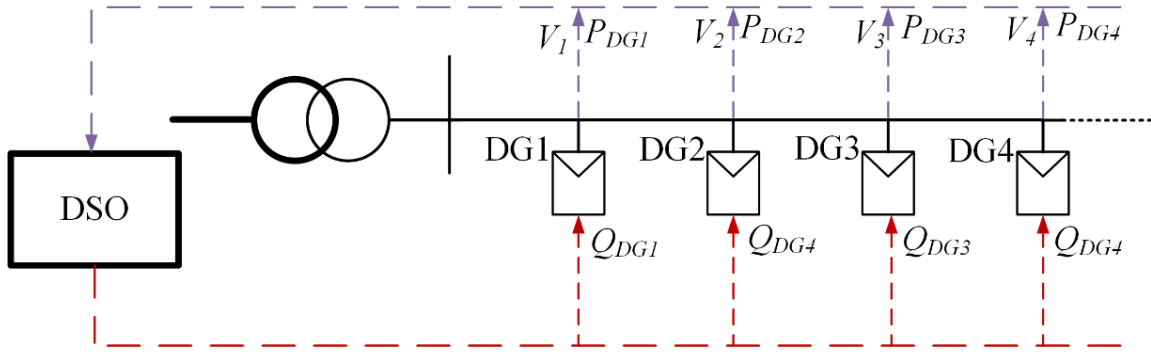


Figure 4.3. Volt/Var control strategy in a distribution network.

segment to monitor the system. If voltage violation occurred in the distribution feeder, solving for optimal power flow optimization for reactive power allocation among DGs will be initiated.

A primary goal of this research is to incorporate the thermal model of the PV inverter to estimate the additional inverter power losses related to supplying reactive power ($P_{loss,DG(Q)}$), which can be found as follows

$$P_{loss,DG(Q)} = P_{loss,DG(P,Q)} - P_{loss,DG(P)} \quad (4.11)$$

where $P_{loss,DG(P,Q)}$ is the total power losses in the inverter switches with the active and reactive power supply, and $P_{loss,DG(P)}$ is the total power losses in the inverter switches with only the active power supply.

Multiple solutions exist that mitigate the voltage rise issue by using Q_{DG} available capacities [96]. In this research, the objective function is defined to minimize the distribution feeder power losses and any additional losses in the PV inverter switches that result from voltage regulation. The objective function can be expressed as follows:

$$\text{minimize} \sum_{i=1}^n P_{loss,add(Q)}(i) + P_{Loss}(i) \quad (4.12)$$

subject to (4.2)-(4.11)

$$V_{min} \leq V_i \leq V_{max} \quad (4.13)$$

$$Q_{DGi,min} \leq Q_{DGi} \leq Q_{DGi,max} . \quad (4.14)$$

This problem can be solved using the particle swarm optimization (PSO) method. PSO is a nondeterministic, population-based optimization introduced by Kennedy and Eberhart [97]. The PSO method has been widely used in power system studies to allocate optimal control settings, particularly in Volt/Var control strategies [98]–[100]. To investigate the effectiveness of PSO in reactive power optimization and power loss minimization, it has been successfully applied to various distribution and transmission systems [101].

PSO works by initiating random particles (x_i) within the search space. Then, each particle is evaluated by the objective function. PSO searches for the best candidate that allows the global minimum (g_{best}). In each iteration, particles modify their values or position and move toward g_{best} , as expressed by

$$v_{i+1} = wv_i + c_1r_1 (P_{best} - x_i) + c_2r_2 (g_{best} - x_i) \quad (4.15)$$

$$x_{i+1} = x_i + v_{i+1} \quad (4.16)$$

where v_{i+1} and x_{i+1} are the new iteration velocity and position of the particles, respectively; w is the inertia weight; r_1 and r_2 are random numbers between 0 and 1; and c_1 and c_2 are correction factors. In each iteration, PSO seeks to find a candidate that allows g_{best} and its update P_{best} for each particle that allows the best personal solution. This will continue until a termination condition is met.

4.4 Simulation Results

4.4.1 Volt/Var Control Results

To investigate the effectiveness of the proposed control strategy, a medium-voltage (MV) distribution feeder based on a 33-bus system was considered as the test system [95]. The test system was modified to include only nodes from 1 to 18, with the same peak load and feeder impedance in the original network, as shown in Fig. 4.4. In practice, loads and distributed PV systems are connected to low-voltage distribution laterals. However, the scope of this study is to investigate the impact of high PV penetration on the main distribution feeders. Therefore, distributed PVs and loads were aggregated and connected to each node through 12.6 kV/0.24 kV three-phase transformers. The peak load of this feeder was 3.4 MW, which occurred in the summer; the PV penetration was assumed to be 100%, according to the summer peak. The aggregated inverter capacity (per node) was 200kVA, which included 62 PV units at each node.

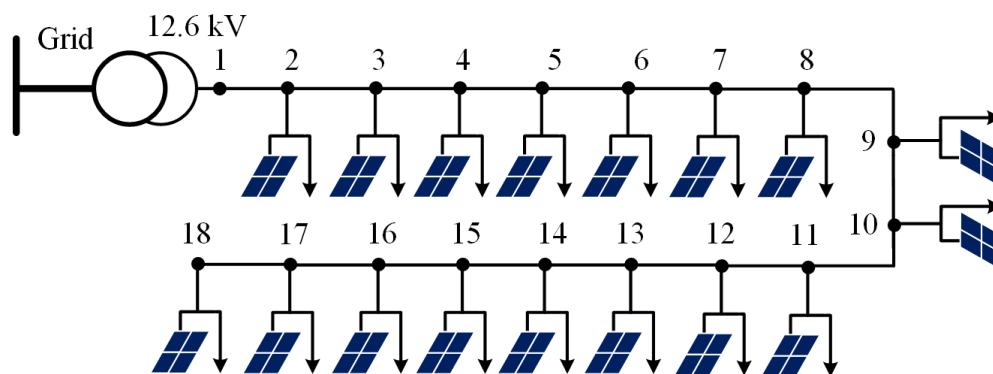


Figure 4.4. 18-node test system.

To evaluate the proposed Volt/Var control strategy as well as the reliability of the PV inverters over a long time span, yearly mission profiles of the solar irradiance, ambient temperature, and loads were considered in the case study. The solar irradiance and ambient temperature data (15-min resolution) remained the same as described in Section 2.3. The scaled load profile was extracted from the Residential Energy Consumption Survey (RECS) for residential loads, collected by the U.S. Department of Energy (DOE) [102], as shown in Fig. 4.5. The scaled load profile can be multiplied by the peak power of each node to obtain the load. All yearly mission profiles are from Phoenix, Arizona, collected in 2011, for the entire year. In the analysis, the same PV production and load profile were applied to all distribution feeder nodes.

To incorporate the thermal model of PV inverter in the proposed control strategy, a three-phase inverter module from a leading manufacturer was selected. The electrical and

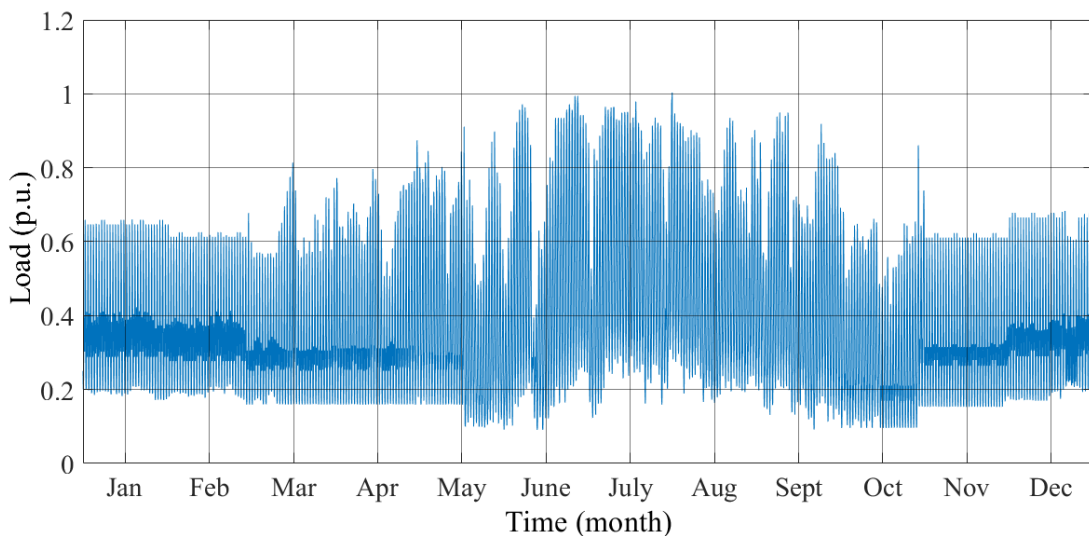


Figure 4.5. Scaled load profile (15 minute per sample).

thermal parameters of the PV inverter are given in Table 2.2. The steps of calculating the losses and the junction temperature in the inverter were explained in detail in Chapter 2.

In this work, three cases were considered:

- Case 1: Without Volt/Var from DGs.
- Case 2: With Volt/Var from DGs, considering minimizing feeder losses.
- Case 3: With Volt/Var from DGs, considering minimizing feeder losses and additional inverter losses.

The annual voltage profiles of node 18, which is located at the end of the feeder, was obtained from the load flow simulation of the network with and without Volt/Var control; the results are shown in Fig. 4.6. The time step of the annual voltage profiles is 15 min, resulting in 35,040 readings. The voltage rises above the permissible value of 1.05 p.u. in 2,977 readings, mainly in the fall and spring, because PV production is greater than the local demand due to a lower load consumption, as observed in the zoomed plot in Fig. 4.6. In addition, the voltage fluctuation due to the intermittent nature of solar energy is evident, which emphasizes the importance of short-term scheduling. When any voltage violation is detected, the centralized Volt/Var control is enabled to regulate the most critical node voltage. Both the conventional (Case 2) and the proposed (Case 3) Volt/Var control strategies were capable of maintaining the voltage within limits by scheduling the available capacity of Q_{DG} based on the optimal power flow solution every 15 min.

To analyze the impact of the Volt/Var control on the thermal performance of the PV inverter and the distribution network, a modified boxplot introduced by Tukey [103] was used to visualize the results of 2977 samples in which voltage violations were observed. The

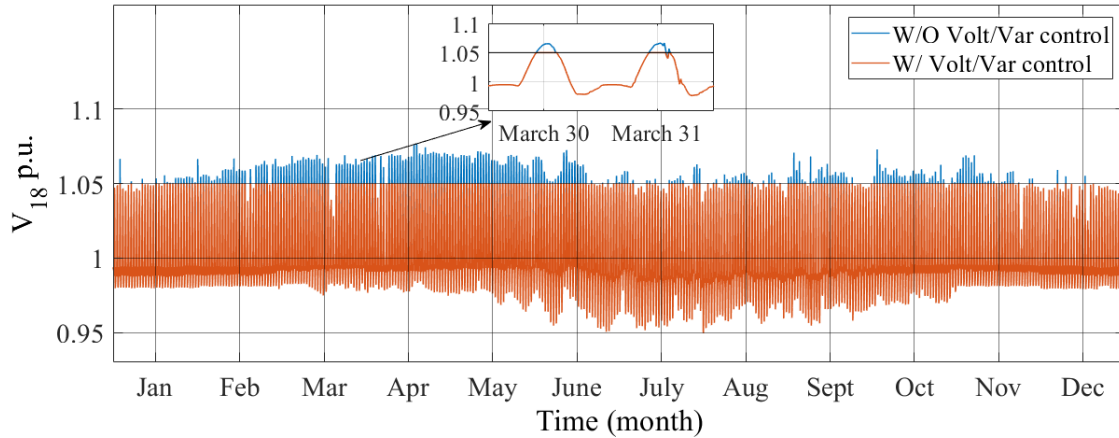


Figure 4.6. Voltage profile of node 18.

absolute magnitude of the reactive power compensation by DGs ($|Q_{DG}|$) at each individual node is displayed in Fig. 4.7. The Volt/Var control strategy in Case 2 results in an excessive reactive power supply, especially in DGs at nodes 2, 7, 8, 13, 14, 17, and 18, where the median $|Q_{DG}|$ values are above 100 kVar. Overusing PV inverters results in additional losses in the inverter switches. This exposes the switches to a high temperature (Fig. 4.8), compared with Case 1, where no Volt/Var control is applied. Therefore, minimizing the additional losses in PV inverters due to reactive power compensation is considered in the proposed Volt/Var control strategy (Case 3) to offset the temperature rise in the objective function. The reactive power allocation is more equally spread across the distribution network in Case 3, as observed in Fig. 4.7. Even though, there are some instances when DGs supply their maximum available reactive power capacity depending on the loading conditions, the median $|Q_{DG}|$ values were significantly reduced for all DGs except node 18. Consequently, PV inverters switches operated at lower T_j values in most events, compared with Case 2, as shown in Fig. 4.8.

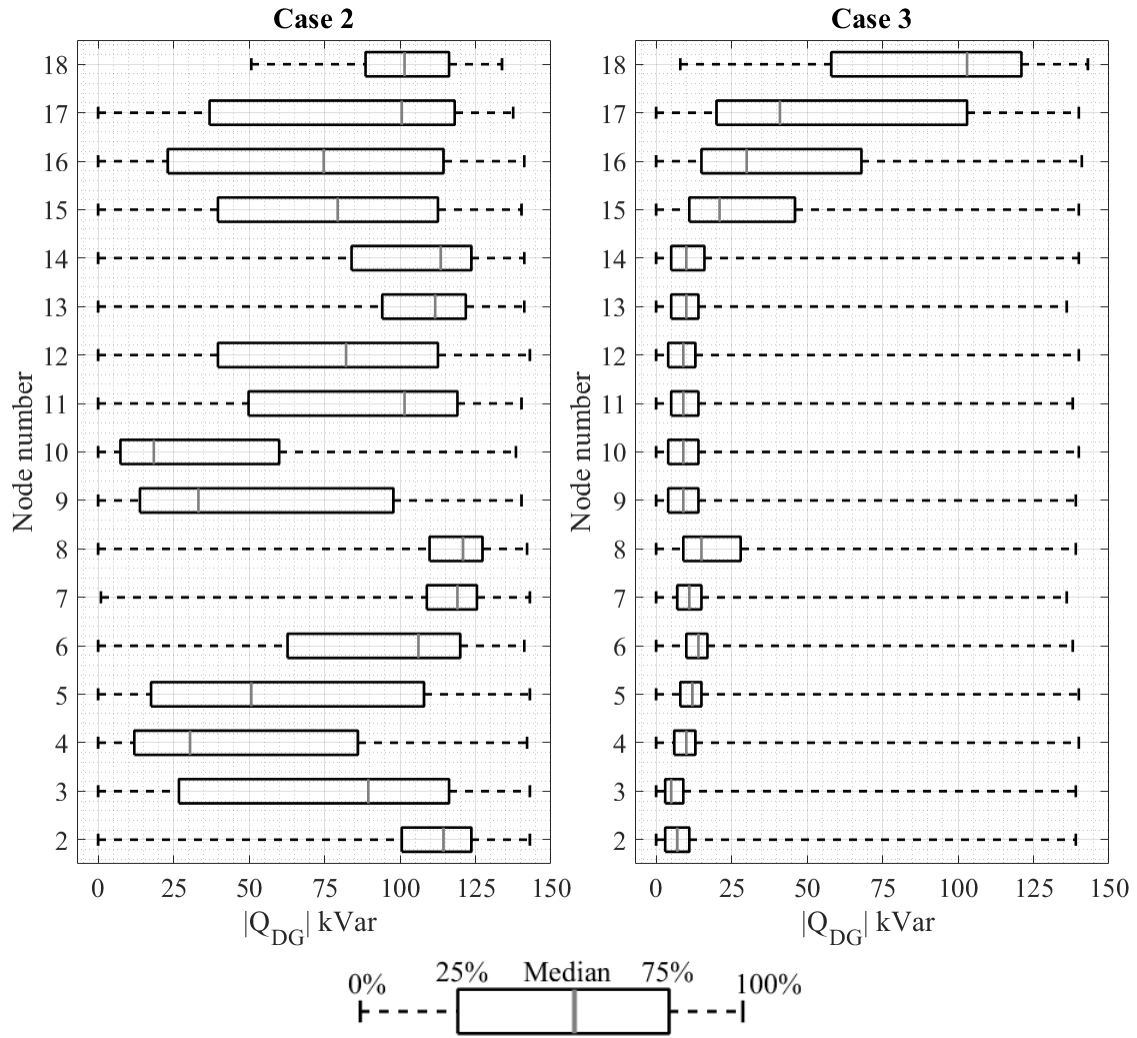


Figure 4.7. Modified boxplot for the reactive power support by PV inverter for different control methods. The whiskers are extended to cover the minimum and maximum values.

Table 4.1 lists the average daily losses of PV inverters and the distribution feeder for the three cases in the given mission profile. Clearly, the application of both Volt/Var control strategies resulted in increased energy losses of the inverters and the network. The proposed control led to reduce daily energy losses of PV inverters by 20 kWh compared with the conventional strategy in Case 2. However, this came at the cost of a slightly higher distribution

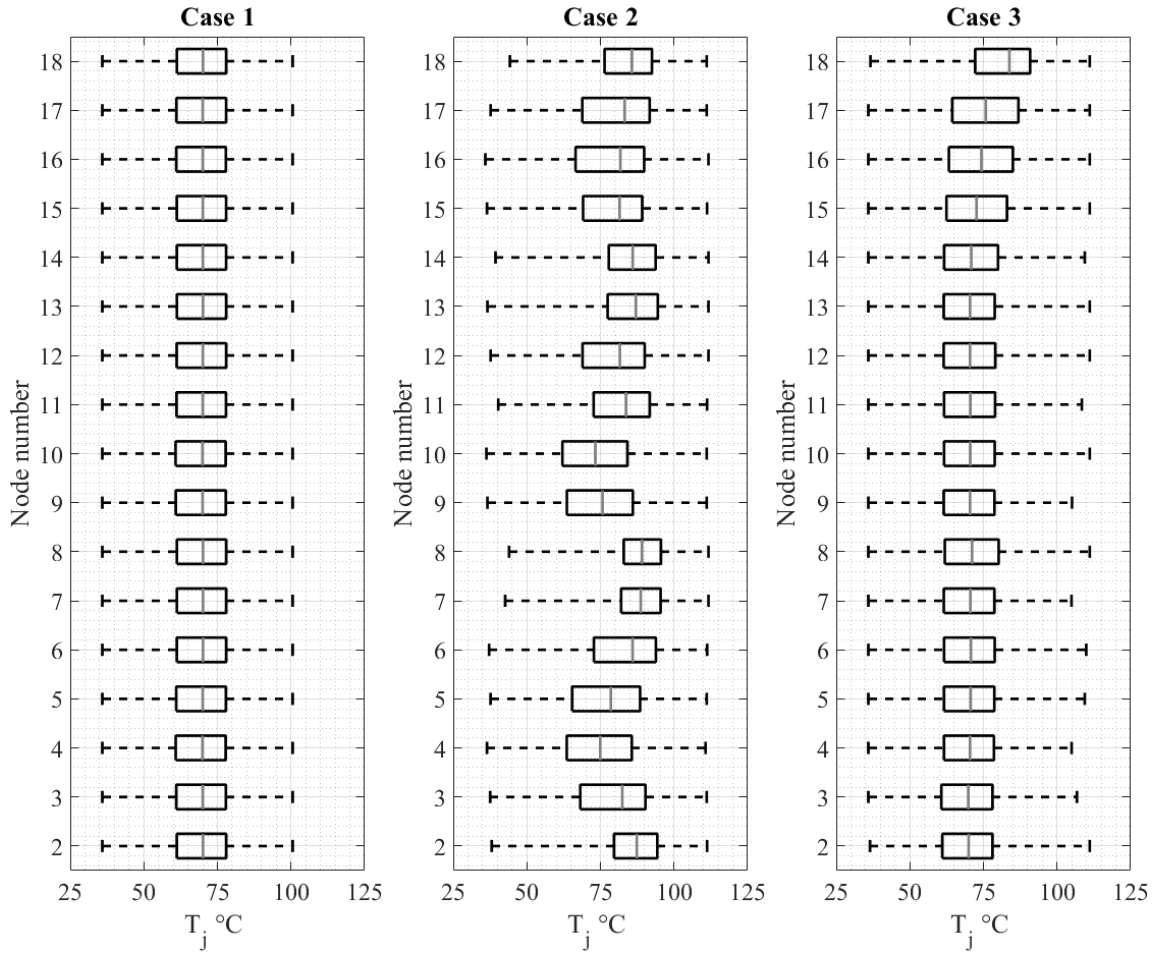


Figure 4.8. Modified boxplot for the junction temperature (T_j) of IGBT devices in PV inverters for different control methods.

Table 4.1. Average daily losses of feeder and PV inverters.

	Case 1	Case 2	Case 3
Average daily feeder losses (kWh)	381	396	398
Average daily PV inverter losses (kWh)	253	277	257

of losses. It can be seen as a compromise between improved reactive power allocation and energy losses in the distribution network.

4.4.2 Reliability Analysis

After obtaining the annual thermal profile of IGBTs for the PV inverters, the rainflow algorithm was applied to extract the values from ΔT_j and T_m in the temperature cycles to be used in the damage analysis. The distribution of the extracted temperature cycles from rainflow counting for the PV inverters at node 2 in Cases 2 and 3 are shown in Fig. 4.9. It can be observed from Fig. 4.9(b) that there is a lower number of ΔT_j cycles in the range from 60°C to 90°C and a lower number of T_m cycles in the range from 80°C to 110°C for Case 3 compared to Case 2.

The number of cycles to fail was determined by the Coffin-Manson-Arrhenius model for each cycle. Consequently, the total damage to the inverter switches can be calculated

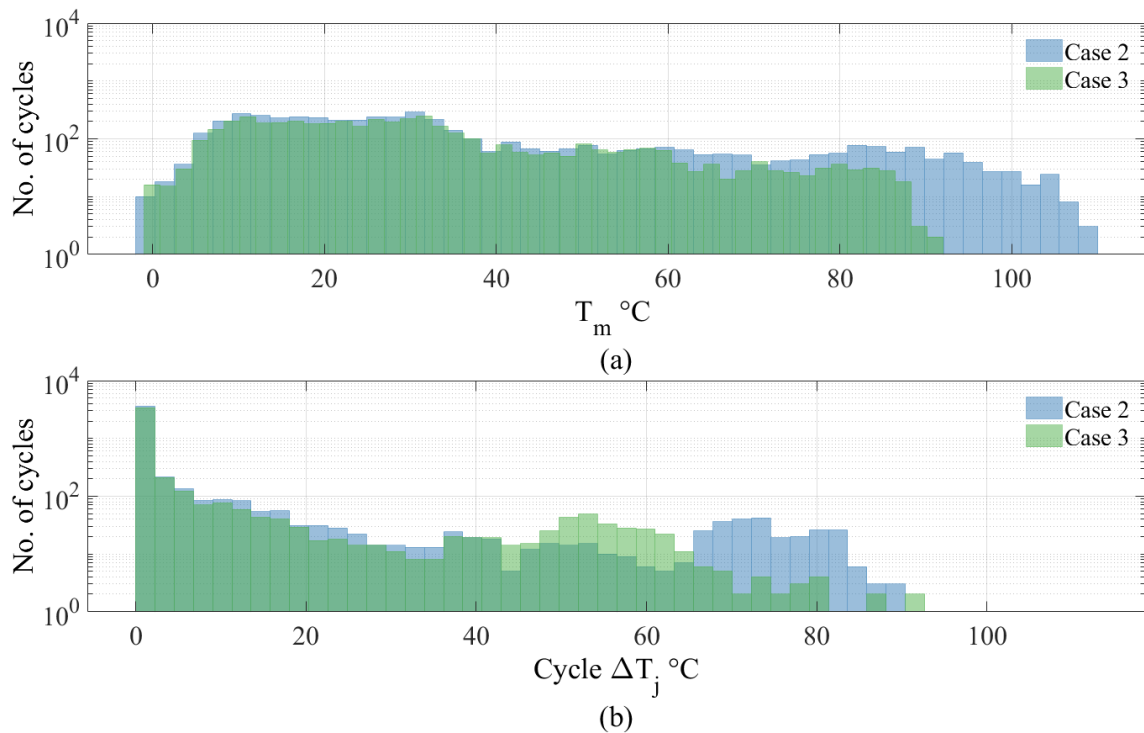


Figure 4.9. Temperature cycle-counting results from the rainflow algorithm for IGBT devices in PV inverters at node 2 for Cases 2 and 3: (a) mean junction temperature (T_m), and (b) junction temperature cycle amplitude (ΔT_j).

according to the Palmgren-Miner rule. Fig. 4.10 shows the total damage of all inverter switches in the thermal loading profiles for the three cases. In Case 1, all inverters had the same total damage because they shared the same PV production profile, and Volt/Var control was not considered. Case 2 exhibits the highest damage due to the rise in the thermal stress of the devices, which resulted from an excessive reactive power compensation by PV inverters. The results show that the damage percentage of all inverter devices decreased with the proposed Volt/Var control in Case 3. Inverters at nodes 2 to 15 benefited the most, as their damage percentages dropped by more than half compared to Case 2. This is a consequence of considering PV inverter losses in the optimization, which eventually led to relieve the thermal stress of the inverter switches. The analysis of determining accumulated damage of Inverter switches can be used in estimating the real cost of reactive power compensation using DGs,

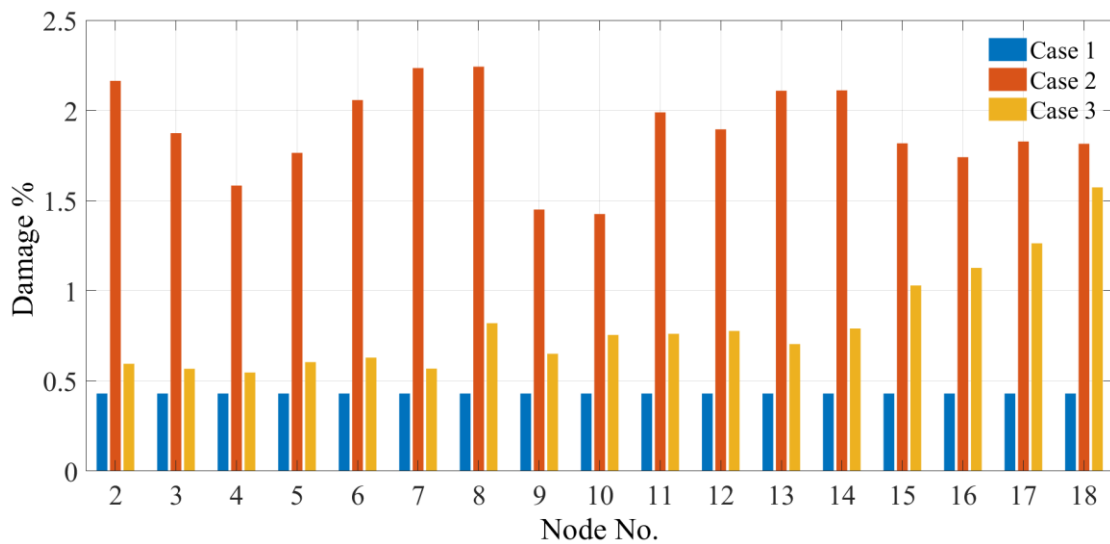


Figure 4.10. Accumulated damage of IGBT devices in PV inverters for different control methods (cases).

which can help power system planners when choosing between conventional devices and DGs to regulate the voltage in distribution networks.

4.5 Contribution

- A Volt/Var control strategy in distribution networks was proposed.
- The strategy aims to minimize both distribution system losses and overutilization of inverters caused by Volt/Var control by optimizing reactive power allocation among DGs.
- The main advantage of considering PV inverter utilization through inverter switching loss minimization is to relieve the thermal stress of the inverter switches.
- An electrothermal inverter was used to analyze the impact of reactive power compensation on the thermal performance of power electronic switches.
- A radial distribution feeder with PV penetration was employed as a test system to analyze the proposed control strategy for long-term mission profiles.
- Reliability analysis was conducted to determine the total damage inverter switches in the obtained thermal profile.

4.6 Conclusion

This chapter presents a Volt/Var control strategy by scheduling the available reactive power capacity of PV inverters to mitigate the voltage rise in distribution systems in a centralized manner. The control strategy considers minimizing the additional losses in the PV inverter switches caused by the reactive power supply as well as minimizing distribution

network losses. Yearly mission profiles of solar irradiance, ambient temperature, and load were considered to evaluate the effectiveness of the proposed method. The reported simulation results clearly show that the proposed control is capable of maintaining the voltage within the limit, while it results in improving the reactive power allocation among the PV inverters and lowering the power losses in the inverter switches, and consequently, relieving the thermal stress.

The rainflow counting algorithm was applied to the thermal profile to extract temperature cycles to investigate the impact of temperature variations on switch lifetime. The results from the reliability-based fatigue model reveal that the damage to the inverter switches can be significantly decreased when limiting the reactive power supply in Volt/Var control.

5 Reactive Power Management in Distribution Networks with Intermittent Renewables

5.1 Introduction

The fast-growing capacity of distributed generation (DG) has led to new operational challenges in both distribution networks and the bulk power system. Conventional voltage regulation devices, such as load tap changers (LTCs) and capacitor banks, are not sufficient to deal with high-voltage variation due to the intermittent output of renewable energy sources (RES)-based DGs. In addition, at high levels of DG penetration, overvoltage caused by a reverse power flow could occur in the distribution network. The role of DG lies in replacing conventional generation, which is currently the main source of the reactive power reserve in the system. DG can provide reactive power during an emergency to secure the system.

Different voltage control methods in the presence of high RES-DGs have been proposed to deal with the voltage rise issue. Conventional voltage regulation devices and a synchronous generator have been combined to control voltages throughout the distribution network [83]. A reconfigurable distribution network can mitigate voltage rise [15], [104], [105]. To facilitate a large increase in DG penetration, a power electronics converter with reactive power compensation has been implemented and evaluated as an alternative to using the normally open point [106]. Structural changes in distribution networks are very effective solutions for overvoltage prevention and accommodate higher levels of PV penetration. However, technical and cost-related issues could impact end consumers as well as utility companies.

A smart PV inverter that has an exchanging reactive power capability with the grid can provide flexible voltage control and cut the cost of upgrading the network. Some local voltage control strategies rely only on the measurement at the point of common coupling with the grid [107]–[109]. Droop-based control is the most common in decentralized approaches [22], [110]–[112]. The droop-based methods are designed to mimic the synchronous generator excitation control system by updating the set point of the reactive power in the event of voltage deviation. Despite the simplicity of applying droop control in decentralized architecture, it suffers from poor performance in low-voltage distribution due to voltage dependency on both active and reactive power as well as distribution feeder impedance [113]. In the case of voltage rise at the end of the feeder, a larger amount of reactive power could flow to regulate the voltage, causing higher losses in the distribution network. Thus, several decentralized Volt/Var control methods have been proposed to improve reactive power sharing among DGs. Tuning the droop coefficients of each DG based on the sensitivity of the voltage magnitude with respect to the injected power has been proposed [19]. This method requires historical data about DGs and load to optimize the amount of reactive power. An adaptive, decentralized droop control has been presented to improve reactive power sharing among DGs [114].

As overvoltage issues in distribution networks are caused by back-feeding active power to the grid, limiting DG power production is a highly effective approach to prevent voltage rise above the permissible limit [19]. The droop-based control can be extended to active power curtailment applications for overvoltage prevention [115]. But when there are several DGs distributed along the feeder, DGs at the end of the feeder would exclusively participate in active power curtailment to mitigate voltage regulation problems. Therefore, the DGs at the end could be affected by unfair participation, such that they lose the benefits of active power

curtailment. Therefore, feeder and power flow characteristics must be considered to improve sharing among DGs and guarantee fair participation in energy management strategies [14], [91].

Centralized control schemes for voltage regulation rely on the availability of bidirectional communication channels to collect measurements and dispatch control commands at regular time intervals [16]. Various centralized approaches have been proposed to address the voltage rise issue in distribution networks with a high penetration of PV systems [18], [116]. In general, centralized schemes aim to minimize power losses over distribution feeders by optimizing control variables so that voltage is maintained within the permissible limit [24], [116]–[118]. MPC has been applied to correct voltage violations by applying optimal changes to the control variables, which are the active and reactive power of DGs [23]. Multi-objective optimization has been performed to minimize both power losses and voltage change along distribution feeders [13], [16]. Despite their efficient performance, online centralized control strategies require fast and robust communication between the DSO and a large number of DGs, which limits the real-time implementation.

Combining local and central schemes extends naturally to controlling applications in distribution networks with high PV penetration. The central control collects measurements of the load demand and DG production to assess the voltage conditions and compute an optimal schedule of DG output reactive power. The schedule is sent to the DGs at every specific time interval. To deal with PV production changes due to cloud movement between consecutive optimizations, the central control can optimize the local controllers' parameters, which can adjust the reactive power output in response to voltage variations at the PCC. To achieve near-optimal local control tuning, accurate solar radiation prediction for the time interval is

essential. Weckx et al. [119] suggest using the short-term forecast to reduce the forecast error due to clouds. The MPC-based voltage control strategy was proposed to overcome distribution model inaccuracies and forecast errors [120]. However, it requires real-time communication to adjust the droop parameters of the local controllers to keep voltages within their limits and balance the contribution of the DGs. To tune the local controllers' parameters, Chistyakov et al. [121] considered the minimum and maximum active power forecast for a given period.

This chapter focuses on optimizing local controllers' parameters to minimize corrective control actions by the local controllers, to keep voltages within allowable limits, considering the uncertainty of PV production. A scenario-based optimization approach was proposed to cover the possible number of potential scenarios to optimize reactive power allocation among DGs. The Monte Carlo simulation (MCS) was used to generate scenarios for PV output based on the stochastic model of PV systems. The scenario reduction algorithm was applied to reduce the number of scenarios to a manageable quantity, thereby reducing the computational complexity. The impact of the proposed Volt/Var control strategy on the thermal performance of the PV inverters was analyzed. Reliability evaluation of power electronics devices in PV inverters was carried out.

5.2 System Operation and Control

Optimally operating DGs is an efficient way to overcome voltage violations in the distribution networks, which are caused by a high level of active power back-feeding to the grid. Fig. 5.1 shows the distribution control architecture. The main control unit periodically collects measurements and computes the optimal set points of DG reactive power. However, during the time period between consecutive optimizations, system conditions can change

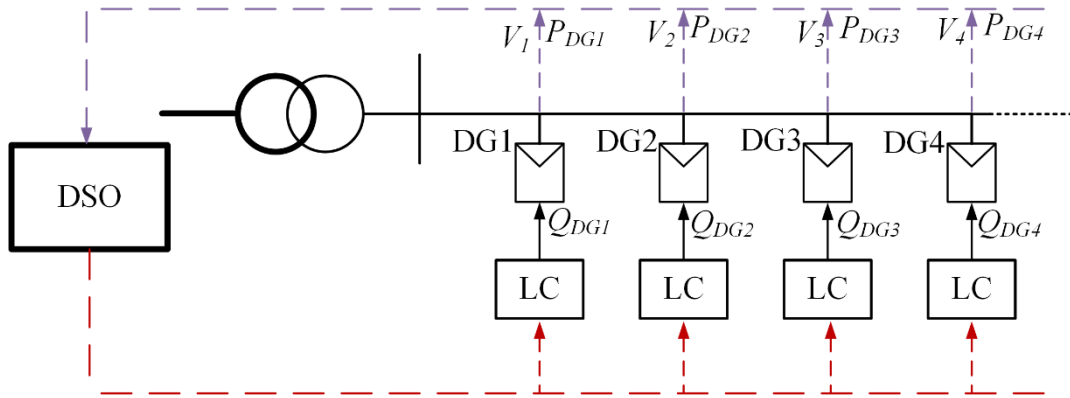


Figure 5.1. Distribution control architecture.

rapidly due to cloud movements or disturbances. Therefore, it may be necessary to operate DGs suboptimally to adapt to changing system conditions. This necessitates having local controllers that can provide a faster response to rapid changes in PV productions. The parameters of the local controllers are optimized such that they minimize the corrective actions, which deviate from scheduled set points. In this work, the control variables are the reactive power output of the DGs. The main controller unit submits the schedule of the local controllers' parameters and the optimal set points to the DGs.

5.2.1 Local Control

Droop techniques are commonly implemented in local control applications [111], [112], [114]. In Volt/Var control, the DG reactive power is determined according to the linear droop characteristic, as shown in Fig. 5.2. If the voltage stays in the dead band [0.95, 1.05], the droop control would not be activated, which means the reactive power set point would not change. The local controller would switch to the droop mode if the measured voltage deviated from the dead band. For instance, if the measured voltage at the DG terminal is greater than

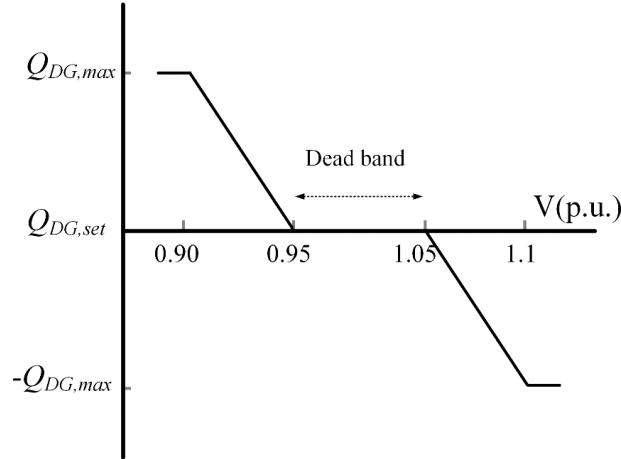


Figure 5.2. V-Q control characteristic.

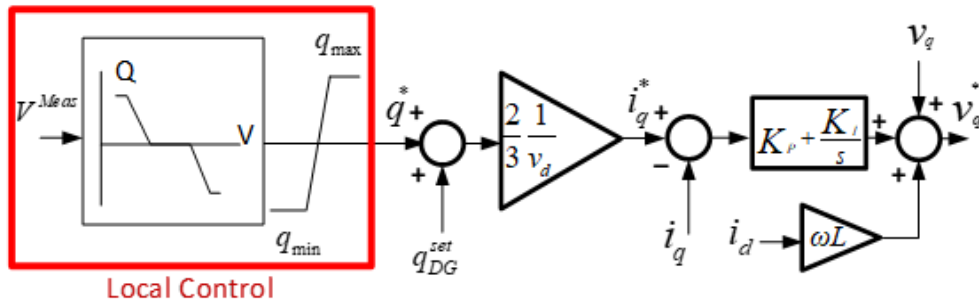


Figure 5.3. Current control block diagram for reactive power control.

the maximum allowable voltage, the DG acts as an inductive load by consuming reactive power to bring the voltage inside the limit.

The reference reactive power can be calculated as

$$q^* = -m(V^{Meas} - V_{max}^{limit}) \quad (5.1)$$

where V^{Meas} is the measured voltage at the PCC, V_{max}^{limit} is the maximum allowable limit (which equals 1.05 p.u. in this work), and m is the V-Q droop coefficient. The droop control is implemented along with the inverter current controller to generate the reactive power reference, as shown in Fig. 5.3. The reactive power reference is processed by the current controller, as explained in Chapter 2.

5.2.2 Centralized Control

The main objectives of centralized control are to monitor node voltage throughout distribution networks and assign corrective actions to DGs in the case of voltage violations. As voltage regulation in this strategy is done by controlling the reactive power generation in relation to the grid, it is important to minimize the cost of the control.

Level 1: Loss Minimization: The centralized control unit computes the optimal reactive power set points of DGs for the next hour. The multi-objective function for minimizing inverter losses and distribution loss is provided in Chapter 4.

Level 2: Local Controller Optimizations: This section discusses how to plan reactive power control to regulate the voltage through the distribution feeder. The DSO optimizes the tuning of the local parameters. The main objective is to minimize the change in the local control variables, while maintaining voltages within the permissible limit, which can be expressed as follows:

$$\min \sum_{i=1}^j |\Delta Q_{DG,j}|^2 \quad (5.2)$$

Subject to

$$\Delta Q_{DG,j} = Q_{DG,j}^{cor} - Q_{DG,j}^{set} \quad (5.3)$$

$$Q_{DG,j} = \sqrt{S_{DG,j}^2 - P_{DG,j}^2} \quad (5.4)$$

$$|V_i|^{reg} = |V_i|^{base} + S_{VQ} \Delta Q_{DG,j} \quad (5.5)$$

$$V^{min} \leq |V_i|^{reg} \leq V^{max} \quad (5.6)$$

where $Q_{DG,i}^{cor}$ is the required reactive to regulate the voltage, $Q_{DG,i}^{set}$ is the set point of the reactive power, $|V_i|^{base}$ is the base voltage before voltage regulation, $|V_i|^{reg}$ is the regulated voltage, and S_{VQ} is the sensitivity factor, which represents the influence of the exchanged reactive power at node j on the voltage at node i .

5.3 Voltage Sensitivity Analysis

The development of a voltage regulation strategy in distribution networks is a challenging task because node voltage is governed by nonlinear equations, which require an iterative power flow solver. The backward-forward, sweep-based power flow is the most popular method for calculating the amplitude of voltages along the distribution feeder. Voltage sensitivity analysis can be incorporated to optimize allocating corrective actions if voltage violations occur. The influence of DG output power on distribution voltages can be represented by the voltage sensitivity factors. Weckx and Driesen propose a statistical model based on historical smart meter data to calculate the voltage sensitivity factors [122]. The perturb-and-observe method is an alternate approach for determining the voltage sensitivity factors; it involves monitoring the voltage changes (ΔV) caused by incremental DG output power adjustments [123]. Hence, each DG can update its voltage sensitivity factor based on local measurements. A control scheme based on MPC has been proposed to compensate for not using voltage sensitivity factors [23]. This method involves solving multi-time step optimization to predict voltage evolution when control actions are applied.

Linearized power flow equations have been used to drive an expression for the voltage variation with respect to reactive power variations in distribution networks [13]. A voltage control approach based on voltage sensitivity analysis has also been proposed [124].

Consider a distribution feeder section, as shown in Fig. 5.4, that connects nodes i and j . By eliminating the nonlinear term in (4.7) that represents the losses, the voltage expression at node j and power flow equations can be simplified as follows:

$$V_j = V_i - \Delta V_{ij} \approx V_i - \frac{R_i P_i + X_i Q_i}{V_j} \quad (5.7)$$

$$P_j = P_i + P_{DG,j} - P_{L,j} \quad (5.8)$$

$$Q_j = Q_i + Q_{DG,j} - Q_{L,j} \quad (5.9)$$

where V_i and V_j are the voltages at nodes i and j , respectively; R_i and X_i are the resistance and reactance of the feeder section i , respectively; P_i and Q_i are the active and reactive power flow in the feeder section i , respectively; $P_{DG,j}$ and $Q_{DG,j}$ are the active and reactive power generation at node j , respectively; and $P_{L,j}$ and $Q_{L,j}$ are the active and reactive power load at node j , respectively.

The OLTC at the substation operates to hold constant voltage; therefore, the only variables that can control the node voltages along the distribution feeder are the active and reactive power flow. The active and reactive power load profiles are assumed to be known. The output active (P_{DG}) and reactive (Q_{DG}) power of DGs are the control variables in this

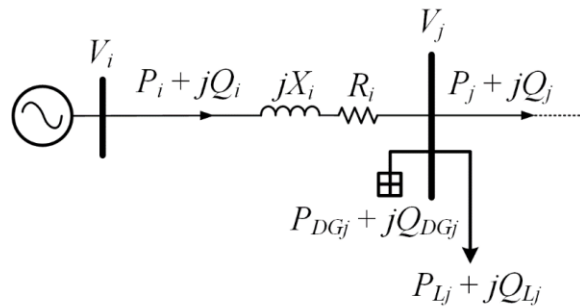


Figure 5.4. Schematic diagram of a distribution feeder.

strategy. The voltage variation with respect to active and reactive power DG variation can be expressed as follows [125]:

$$\begin{bmatrix} \Delta V_1 \\ \vdots \\ \Delta V_n \end{bmatrix} = \begin{bmatrix} \frac{\partial V_1}{\partial P_{DG1}} & \dots & \frac{\partial V_1}{\partial P_{DGn}} \\ \vdots & \ddots & \vdots \\ \frac{\partial V_n}{\partial P_{DG1}} & \dots & \frac{\partial V_n}{\partial P_{DGn}} \end{bmatrix} \begin{bmatrix} \Delta P_{DG1} \\ \vdots \\ \Delta P_{DGn} \end{bmatrix} + \begin{bmatrix} \frac{\partial V_1}{\partial Q_{DG1}} & \dots & \frac{\partial V_1}{\partial Q_{DGn}} \\ \vdots & \ddots & \vdots \\ \frac{\partial V_n}{\partial Q_{DG1}} & \dots & \frac{\partial V_n}{\partial Q_{DGn}} \end{bmatrix} \begin{bmatrix} \Delta Q_{DG1} \\ \vdots \\ \Delta Q_{DGn} \end{bmatrix} \quad (5.10)$$

The partial derivative (terms $\partial V/\partial P_{DG}$ and $\partial V/\partial Q_{DG}$) represents the voltage sensitivity factor, which can be obtained using

$$\frac{\partial V_i}{\partial P_{DGj}} = -\frac{1}{V_1} \sum_{i=0}^n R_i \quad (5.11)$$

$$\frac{\partial V_j}{\partial Q_{DGj}} = -\frac{1}{V_1} \sum_{i=0}^n X_i \quad (5.12)$$

where V_1 is the rated voltage at node 1. The sum of feeder section impedances represents the path between node j and the medium voltage bus at the main substation. This relation is not valid in low-voltage (LV) distribution feeders because of the high R/X ratio.

5.4 Stochastic Optimization

5.4.1 PV Stochastic Model

On cloudy days, solar irradiance is intermittent, creating a need for a stochastic model to simulate PV outputs. The stochastic model is a simulation-based technique to describe the nondeterministic behavior of systems [126]. The beta distribution function is used to generate simulation scenarios. When the certain prediction value is P_{pred} , the occurrence of the PV output active power value y can be modeled by the beta function, as follows [127]:

$$F_{P_{pred}}(y) = y^{\alpha-1} \cdot (1 - y)^{\beta-1} \quad (5.13)$$

where α and β are shape parameters. Both α and β can be expressed as functions of the mean (P_{pred}) and its error variance (σ^2), and can be calculated as follows:

$$P_{pred} = \frac{\alpha}{(\alpha + \beta)} \quad (5.14)$$

$$\sigma^2 = \frac{\alpha \beta}{(\alpha + \beta)^2 + (\alpha + \beta + 1)}. \quad (5.15)$$

The Monte Carlo simulation (MCS) is a probabilistic method that is commonly used to predict the behavior of system components and can be used to generate scenarios for PV outputs based on the PV stochastic model.

5.4.2 Scenario Reduction

The solution to a stochastic optimization problem requires a proper representation of uncertainty, which can be obtained by generating a set of scenarios. Sampling from historical data or a statistical model is used to create these scenarios. In a highly variable system, a large number of scenarios might be used to cover possible cases that require high computation effort to solve. There often exists a trade-off between the quality of the solution and the computation effort.

Several scenario reduction approaches are proposed for optimization problems under stochastic uncertainty to reduce the computational intensity [128]–[130]. The backward reduction (BR) algorithm, introduced in [131], exploits the probability distance to select/delete scenarios iteratively. The procedures of BR used in this work are presented below:

- 1) Initialization: Generate N scenarios, with the initial probability of each scenario equal to $1/N$.

- 2) Compute the Kantorovich distance (KD): Construct a KD matrix for all scenarios. The distance KD_{ij} between two scenarios s_i and s_j is defined as

$$KD_{ij} = |s_i - s_j|. \quad (5.16)$$

- 3) Find the nearest scenario: Search for the minimum KD_{ij} for each scenario.
- 4) Compute the probability (PKD) for each pair of scenarios found in step 3:

$$PKD_{ij} = \min |s_i - s_j| * P_i \quad (5.17)$$

where P_i is the probability of scenario s_i . Eliminate scenario s_i , and add its probability P_i to the probability of the nearest scenario P_j .

$$P_j = P_i + P_j. \quad (5.18)$$

- 5) Construct a new KD matrix after eliminating the scenario in the previous step.
- 6) Repeat steps 2-4 until the target reduced scenario is found.

5.4.3 Stochastic Optimization

The implementation of stochastic optimization methods provides a means of coping with the intermittent nature of systems models. A scenario-based stochastic optimization is commonly used to explore optimal DG management decisions with respect to DG output uncertainty for different applications in power systems [16], [132]. In this work, a scenario-based stochastic optimization process was used to optimize the local control parameters. The MCS generated a set of scenarios to cover a wide range of possible PV outputs. Scenario reduction was applied to decrease the number of scenarios from N to n . The objective function in (5.2) was reformulated as follows:

$$\min \sum_{s=1}^n P_s \left(\sum_{i=1}^j |\Delta Q_{DG,i}|^2 \right). \quad (5.19)$$

The problem can be solved using the particle swarm optimization (PSO) method, explained in Chapter 4. The above objective function is solved every hour to schedule ΔQ_{DG} which is the reactive power based on measurements and results from the stochastic PV model. Fig. 5.5 shows the flowchart of the calculation process of the optimal local control parameters.

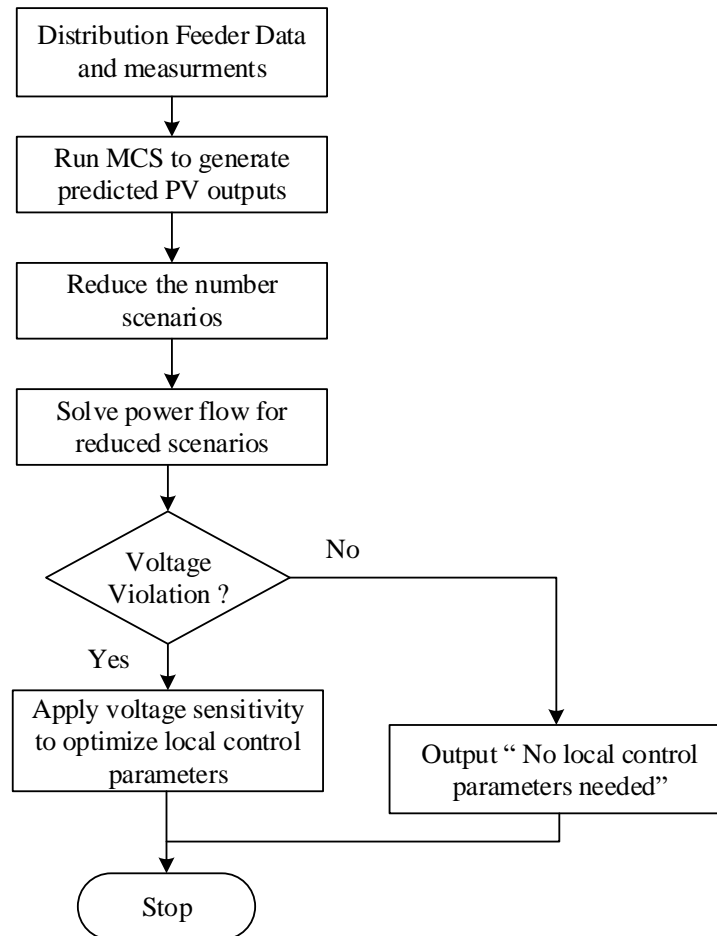


Figure 5.5. Flowchart of optimal local control parameters.

5.5 Case Study

To validate the proposed strategy and examine its effectiveness, the 18-node, medium-voltage (MV) distribution feeder, displayed in Fig. 4.4, was considered again. The system details and PV generation location and capacity remained the same as described in Section 4.4. The case study used 1-min resolution irradiance and ambient temperature data provided by NREL in [66], whereas the load profile was developed based on the DOE residential load model in [102]. The mission profiles of PV production, ambient temperature, and load profiles are shown in Figs. 5.6, 5.7, and 5.8, respectively. The scaled profiles are multiplied by the peak power to obtain the load and PV production for each node. All yearly mission profiles are from Phoenix, Arizona, collected in 2011, for the entire year. In the analysis, the same PV production and load profile were applied to all distribution feeder nodes.

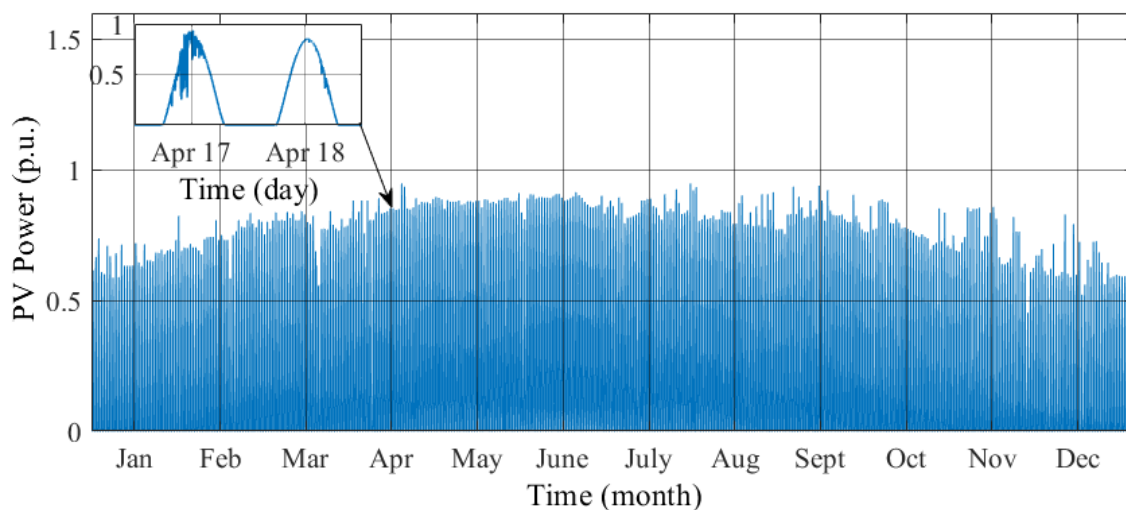


Figure 5.6. Scaled PV active profile (1 minute per sample).

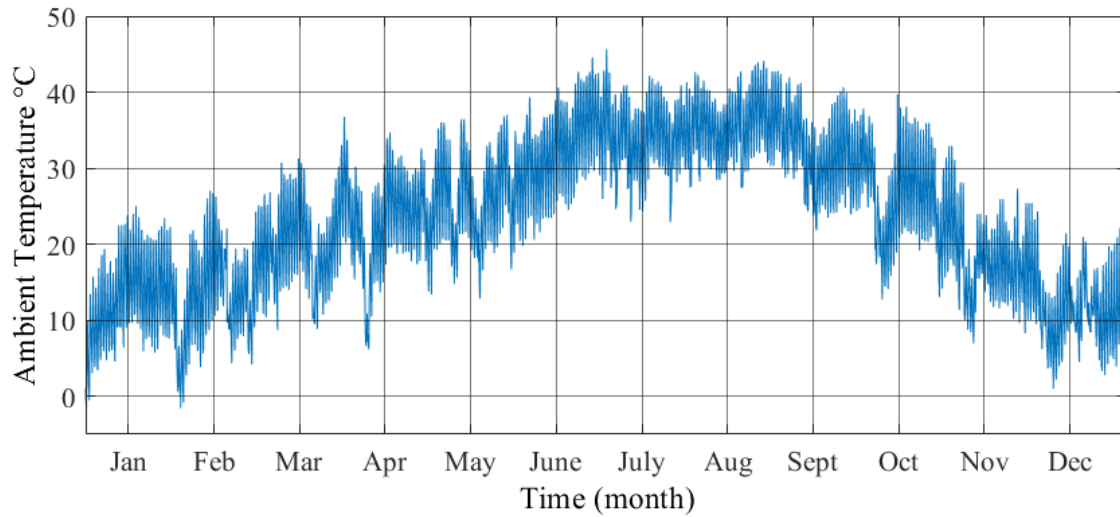


Figure 5.7. Ambient temperature profile (1 minute per sample).

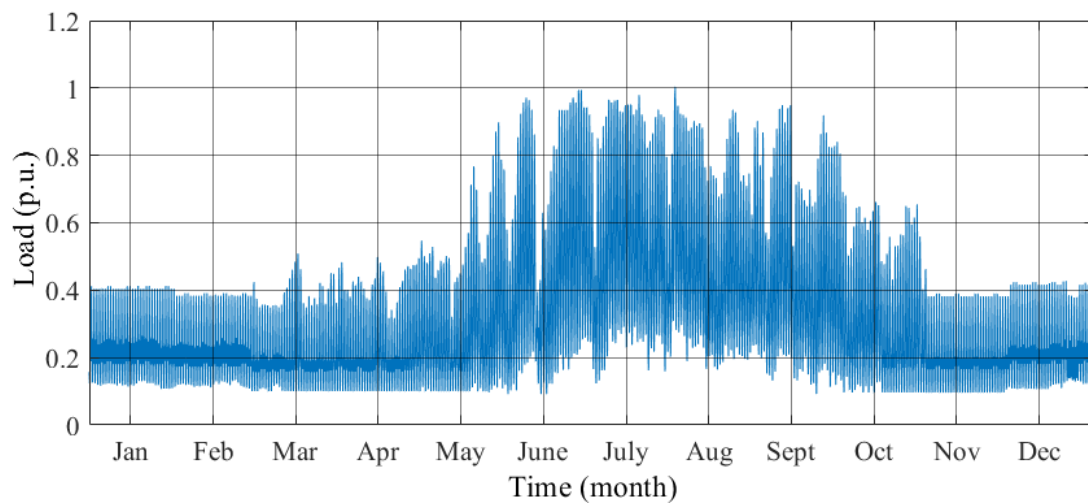


Figure 5.8. Scaled load profile (1 minute per sample).

5.5.1 Volt/Var Control Results

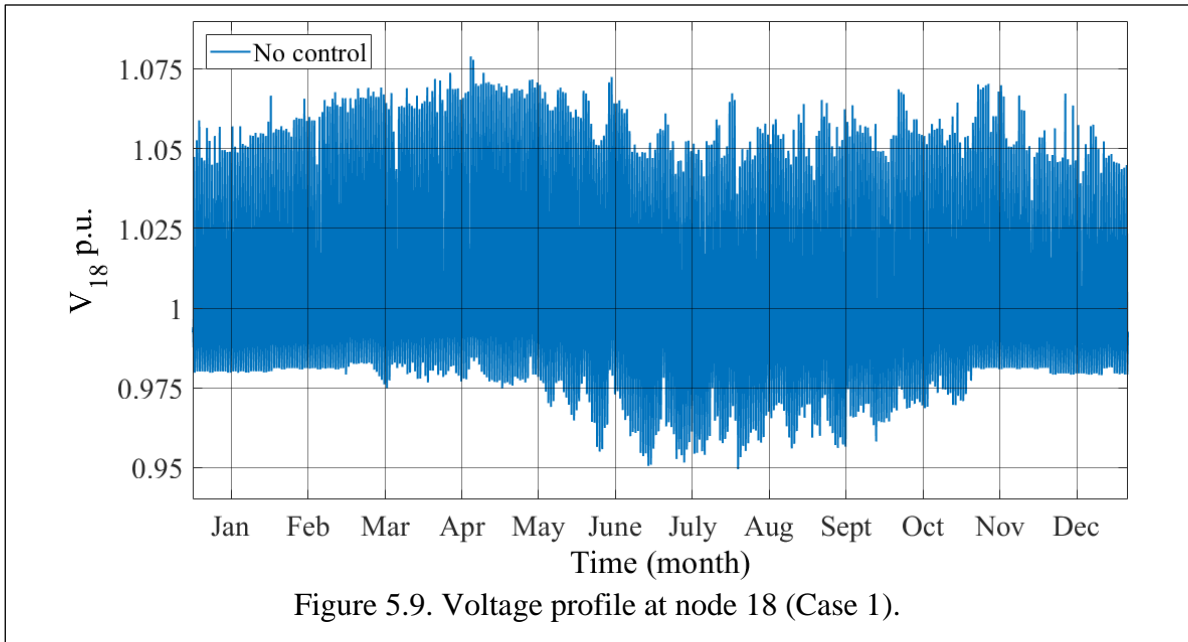
In this section, time series simulations were used to evaluate the performance of four Volt/Var control strategies:

- Case 1: Base case without Volt/Var control by DG.

- Case 2: Static central control method.
- Case 3: Online central control method.
- Case 4: Combined control method.

In Case 1, no reactive power support from DGs was considered. PV units operate with MPPT at unity power factor. The voltage of node 1 at the substation was assumed to be constant and set to 1 p.u. Power flow solver was used to calculate voltage values throughout the distribution network for the given mission profile. The annual voltage profile of node 18, which is located at the end of the feeder is shown in Fig. 5.9. The voltage rises above the permissible values of 1.05 p.u. in 43,650 readings in the given mission profiles because PV production is greater than the local demand due to a lower load consumption.

In Case 2, the DSO collects measurements throughout the distribution network to monitor voltages throughout the network. When any voltage violation is predicted in the next hour, the static central optimization in (4.11) is used to define the reactive power set point of



the DGs, to mitigate overvoltage issues. Fig 5.10 shows the empirical cumulative distribution function (CDF) curves of the maximum voltage magnitudes at node 18. It can be observed that the Volt/Var control strategy in Case 2 reduced the probability of voltage violations by 45% compared to Case 1. On clear days, the static central control could accurately predict PV production and schedule the reactive power set point of PVs to correct the voltage rise issue, as shown in Fig. 5.11. The static central control performance was sufficient in this case. In the presence of clouds, PV production can rapidly change. Therefore, the planned reactive power by the central control scheme might not be sufficient to correct voltage violations, as is evident in the voltage profile of Nov. 20.

In Case 3, the online central control includes a two-stage strategy for managing DG reactive power. The first stage was similar to the control strategy in Case 2. The second stage includes a real-time voltage control to adjust the DGs' reactive power set points to correct for voltage violation by solving for (5.2). In Figs. 5.10 and 5.12, with online central control, it can

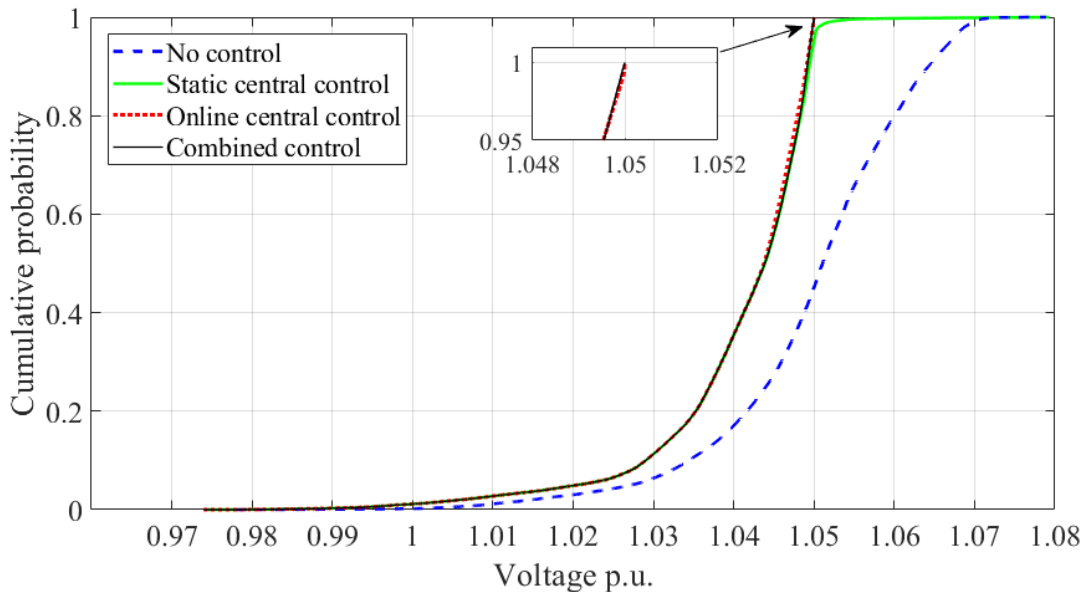


Figure 5.10. Empirical CDF curves of the voltage at node 18 for different control methods.

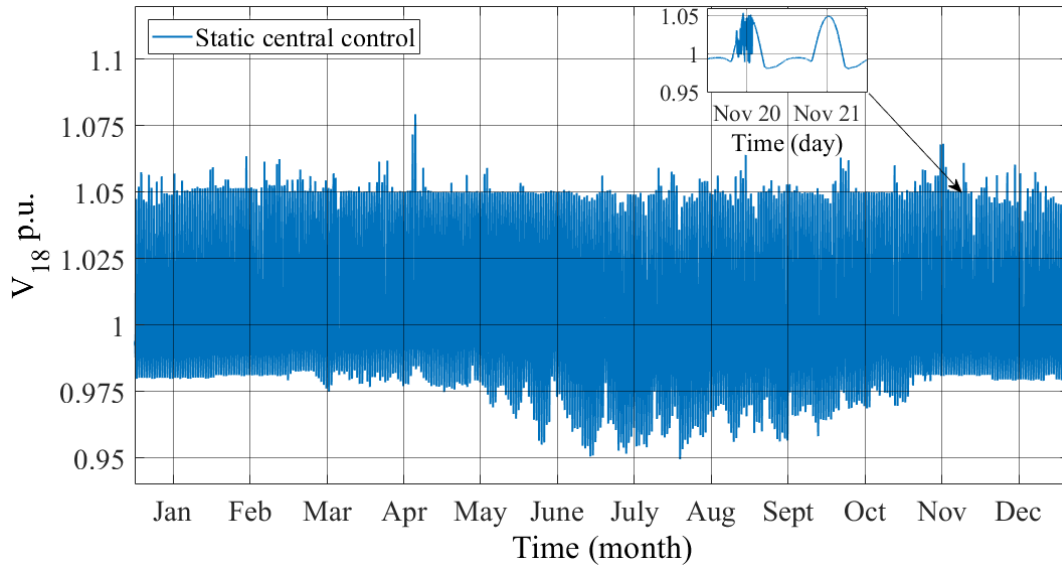


Figure 5.11. Voltage profile at node 18 (Case 2).

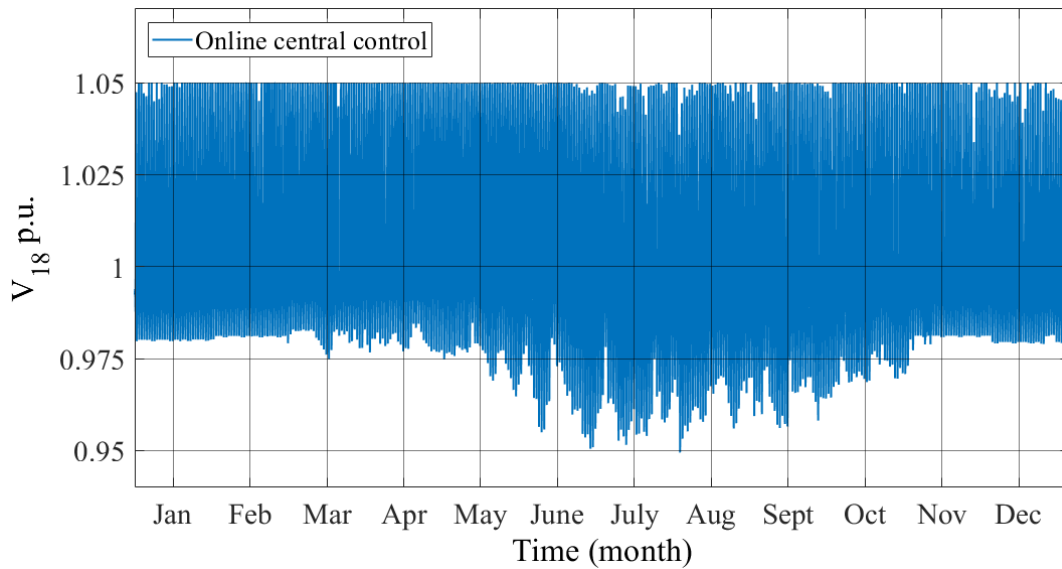


Figure 5.12. Voltage profile at node 18 (Case 3).

be observed that all voltage violation occurrences were eliminated, and the probability of observing overvoltage events was zero. Despite the superior performance, online central control requires very fast communication between the DSO and a large number of DGs. Also, this strategy involves a high computational effort for solving the optimization problem.

To cope with the voltage fluctuation and reduce the complexity of the online Volt/Var control scheme, the proposed combined control strategy was implemented. The DSO collects measurements throughout the distribution network to optimize the reactive power allocation among the DG units for the next hour. For local controllers' optimization, a PV stochastic model was used to generate 200 scenarios to represent the prediction error. The generated scenarios were reduced to 20, as discussed in the previous section. The schedule of the local controllers' parameters was obtained by solving the stochastic optimization problem in (5.19). It is obvious that the voltage profile at node 18 is improved by the introduction of the combined control scheme, as shown in Fig. 5.13.

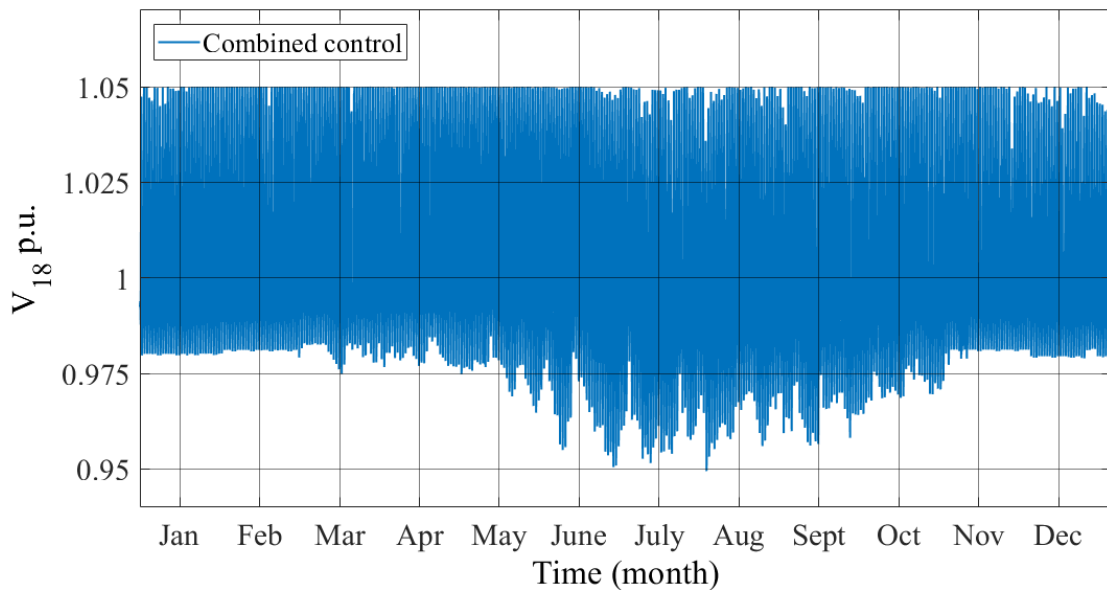


Figure 5.13. Voltage profile at node 18 (Case 4).

The impact of Volt/Var control strategies on the thermal performance of the PV inverters was analyzed. Fig. 5.14 displays a modified box plot for the absolute magnitude of the aggregated reactive power supply by DGs ($|Q_{DG}|$) at each node. It includes the results of 43,650 samples, in which voltage violations were observed when not considering Volt/Var

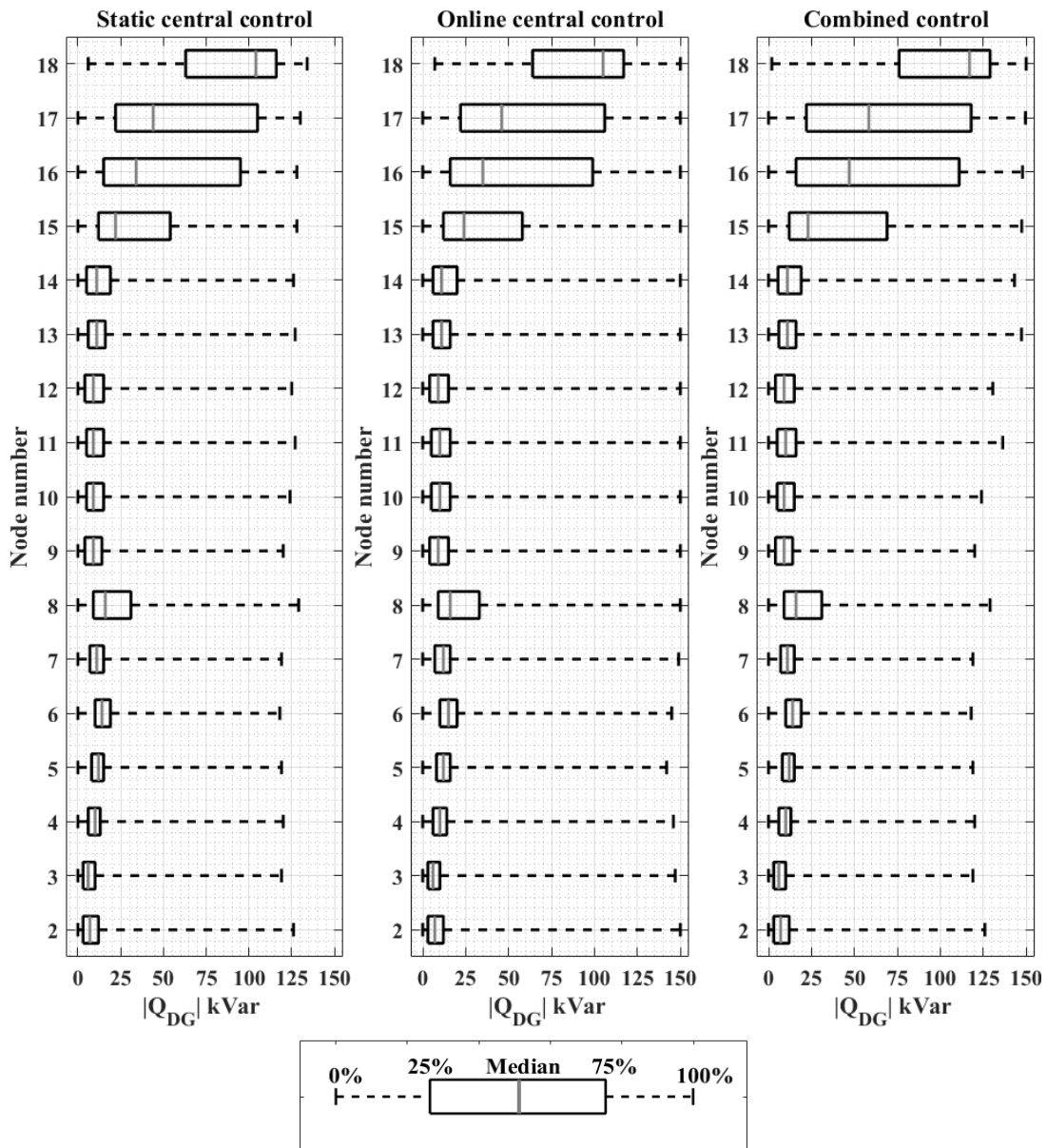


Figure 5.14. Modified box plot for the reactive power support by the PV inverter for different control methods.

control. The reactive power supply by DGs varies depending on the PV and load profiles and their location in the distribution feeder. Clearly, DGs at the end of the feeder provided the most reactive power compensation, mainly close to the locations where voltages rise. The online central control method resulted in a slightly increased reactive power supply at all nodes compared to the static control approach. This is because the real-time control level has the capability to adjust all DGs' reactive power set points to avoid voltage violations. The additional reactive power exchange results in a higher loss in PV units, which eventually leads to a rise in the junction temperature of the inverter switches, as shown in Fig. 5.15. In the combined control method, the local control level can change the output reactive power set points of DGs, depending on local voltage measurements to maintain voltage within the allowable limit. Based on the analysis, nodes 15, 16, 17, and 18 experienced the most overvoltage issues in the tested profiles. Thus, DGs at these nodes participated in the local voltage control mode by absorbing higher reactive power compared to the real-time control level in Case 3. Consequently, PV inverters switches operate at higher junction temperature values.

The performance of Volt/Var control strategies in the four cases was further analyzed. Compared with the online central approach, the high amount of absorbed reactive power in the combined strategies by the local controllers of end nodes DGs increased the distribution feeder average daily energy loss by 0.2 %, as seen in Table 5.1. On the other hand, the average daily PV inverter losses under the proposed method decreased by 0.4 % compared to the online central method. This is because all DGs can participate in correcting voltage violations in the online central approach, whereas the end nodes exclusively provide the reactive power supply in the case of the combined control method. Both control strategies in Cases 3 and 4 had similar

performances in avoiding voltage violations as evidenced by the fact that the maximum observed voltage through the distribution network was 1.05 p.u.

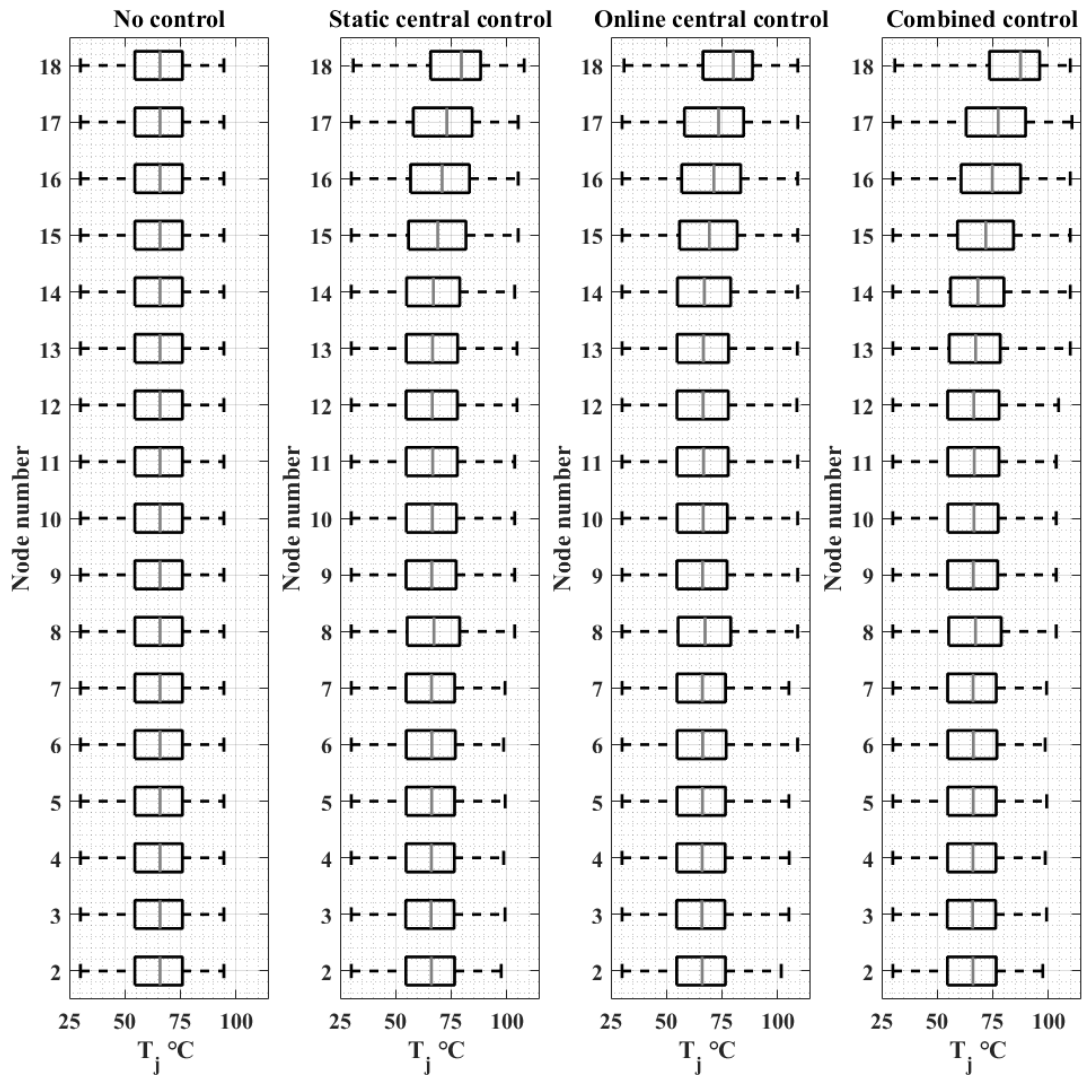


Figure 5.15. Modified box plot for the junction temperature (T_j) of IGBT devices in PV inverters for different control methods.

Table 5.1. Energy losses of PV inverters and feeder, and maximum voltage violation.

	No control	Static central control	Online central control	Combined control
Average daily feeder losses (kWh)	376	409.2	409.8	410.5
Average daily PV inverter losses (kWh)	253	261	262.2	261.5
Max voltage violation (p.u.)	1.08	1.078	1.05	1.05

5.5.2 Reliability Analysis

The rainflow counting method was applied to the thermal profiles to determine the number of cycles present in the thermal loading profiles of the inverters switches in the four cases. The values of T_m and ΔT_j were extracted to be used in the damage assessment of IGBT switches in PV inverters, as explained in Section 2.2. After obtaining the number of cycles to fail using the Coffin-Manson-Arrhenius model (2.26) for each cycle, the linear damage accumulation, described by the Palmgren-Miner rule, was calculated for all IGBT devices in PV inverters in the given thermal profiles, as shown in Fig. 5.16. When no Volt/Var support from PV inverters was considered in Case 1, all PV inverters devices had the same damage accumulation because they shared the same PV profile. Compared to the static central control (Case 2), the damage was higher in all PV inverters with the implantation of the online central control (Case 3). This is because the additional reactive power supply in the real-time voltage control mode results in raising the junction temperature of the inverters switches. The application of the combined control strategy (Case 4) led to an increase in the damage percentage of inverters devices at the critical nodes 15, 16, 17, and 18, compared to Case 3. This is because the local controller would adjust the reactive power set point if the measured

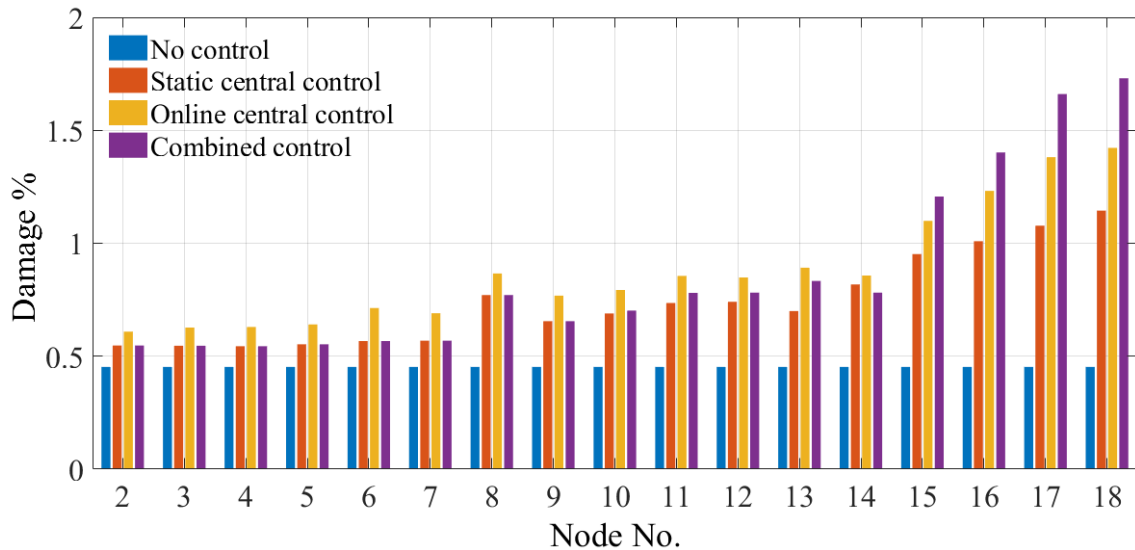


Figure 5.16. Accumulated damage of IGBT devices in PV inverters for different control methods.

voltage at the PCC rose above the allowable limit, which primarily occurs in the downstream distribution network. Therefore, PV inverters connected to the critical nodes operate at higher temperature values.

In the local control level of the proposed strategy, reactive power allocation was unfair to customers connected at the end of the feeder because they provided the most reactive power support to control the voltage. However, considering the low cost of the communication system and computational effort, the proposed Volt/Var control strategy provides a remedy for overvoltage issues in distribution networks with high PV penetration.

5.6 Contribution

- A reactive power management strategy in distribution networks was proposed.
- The strategy combines central and local control schemes. The central control collects both loads and DG measurements to optimize the reactive power set point of DG units to keep voltages within allowable limits. In addition, the central control uses a scenario-based approach to minimize corrective control actions by local controllers.
- The main advantage of using a combined control strategy is to operate DGs suboptimally to adapt to changing system conditions, such as cloud movements or disturbances.
- An electrothermal inverter model was used to evaluate the impact of the proposed control strategy on the thermal performance of IGBT devices in PV inverters.
- The rainflow counting method was incorporated to extract the thermal temperature cycles to be used in determining the accumulated damage of IGBT devices in PV inverters.

5.7 Conclusion

Proper reactive power management from DGs can regulate the voltage in distribution networks. The proposed strategy is based on scheduling the reactive power capacity of the DGs at two levels: local and central. The central control receives measurements to optimize the set points of the reactive power DGs. To mitigate the production uncertainties of renewables, a scenario-based approach is used to optimize the local controllers' parameters. A simulation study was conducted to validate the proposed strategy and examine its effectiveness in

mitigating overvoltage issues over a yearly mission profile. The study investigated the impact of supplying reactive power by PV inverters in the control strategy on the thermal performance of their power electronics devices. The simulation results showed that the proposed strategy is capable of mitigating overvoltage issues. The findings suggest that PV units connected to the end of the feeder provide the most reactive power support in the local control mode.

6 Reactive Power Reserves Management by DGs for Voltage Stability Enhancement: A Case Study

6.1 Introduction

In the classic power system, conventional generators play the main role in automatic voltage regulation in steady-state and transient conditions. This requires maintaining adequate reactive power reserves to prevent voltage collapses throughout power systems. At a high penetration level of distributed PV, a portion of the conventional generation would be displaced, resulting in the loss of the main sources of dynamic reactive power in the transmission networks. Consequently, power systems may become more vulnerable to voltage instability events [133]. To enhance the power system's capability to eliminate large-scale and long-term blackouts and service outages, distributed PV will be expected to provide ancillary services that are traditionally provided by spinning generators and voltage regulators.

In conventional power systems, OLTCs play the main role in regulating voltages at medium-voltage buses. However, the operation of OLTCs can lead to voltage instability. Following a major disturbance, OLTCs operate to restore the voltage throughout the system. At the same time, over-excitation limiters (OELs) restrict generators' output reactive power, resulting in progressive voltage collapses due to reactive power shortages [134]. Therefore, the amount of static and dynamic reactive power reserves must be considered when assessing system stability to prevent voltage collapses [135].

The International Council on Large Electric Systems (CIGRE) proposes applying Q-V analysis to determine the minimum required amount of static and dynamic reactive power resources of critical buses, without the operation of OLTC [136]. The Q-V analysis has been well studied in voltage stability studies [137]–[139]. The Western Electricity Coordinating Council (WECC) [136] specifies that time-domain simulation should be considered to depict the performance of OLTCs and OELs after a disturbance. Both static and dynamic methods can be used to control actions and make determinations in relation to transmission and distribution networks.

The impact of distributed PV systems on distribution networks has been well investigated in the literature [13], [14], [16], [91]. These studies mainly focus on the performance of PV systems, with the assumption that the main grid is always strong. However, when distributed PV systems reach a high level of penetration, they can directly affect the steady state and dynamic performance of transmission systems [4]. Therefore, the interaction between the transmission and distribution networks should be considered when analyzing power system operations.

Operating codes in some countries require Volt/Var regulation by PV inverters [12]. Supplying reactive power to local loads can provide support to transmission networks in stressed operating conditions. Reference [140] evaluates the effectiveness of using the available reactive power capability of distributed generators (DGs) to support a weak area in the case of voltage instability events. If reactive power control is needed during a contingency event, supervisory control at the main substation would issue the control signal to the DGs to supply the maximum available reactive power to prevent voltage instability. A centralized voltage control strategy to deal with long-term voltage stability is proposed [2]. The DSO is

responsible for regulating the voltage at local buses. Following a major outage in the transmission network, the DSO will dispatch a reactive power reference to DGs to support the transmission network. This strategy requires coordination between the transmission system operator (TSO) and the DSO to adjust the control logic of the OLTC and perform voltage reduction to prevent progressive voltage collapse. Even though centralized control strategies provide superior performance in supporting the bulk power system, they require rapid communication between system elements.

In this research, long-term voltage instability will be assessed in the presence of high PV penetration. PV inverters have the capability to regulate the voltage at the point of common coupling (PCC) by adjusting their reactive power references using local controllers. Therefore, the inverter can supply reactive power to decrease the reactive power demand from the main grid and support the system after major disturbances. The CIGRE Nordic network is used as a test system. The Q-V analysis and dynamic simulations are carried out using Power System Simulator for Engineering (PSS/E) software. The dynamic model of power system elements will be introduced in detail.

6.2 Voltage Stability Assessment

According to (IEEE)/CIGRE Joint Task Force, the definition of voltage stability is “the ability of a power system to maintain steady voltages at all buses in the system after being subjected to disturbance from a given initial operating condition” [141]. Voltage instability occurs when the power system becomes unable to meet the reactive power demand, which results in progressive and uncontrollable voltage declines. Consequently, the under-voltage load shedding relay responds by tripping a portion of the local load to prevent voltage collapse.

If the protective system action fails to rebalance the load and the power generation, widespread outages might occur.

Voltage stability dynamics may vary within seconds to tens of minutes. Depending on the time response of the acting equipment in voltage problems, voltage stability can be either short-term or long-term, as shown in Fig. 6.1. Slower-acting equipment, such as the OLTC and OEL, play the primary role in long-term voltage stability [142]. This research focuses on long-term voltage stability assessment and enhancement in power systems with a high penetration of distributed PV.

To assess the voltage stability in power systems, two main methods are frequently used. The first method is based on a static power flow analysis. The second method includes a time-domain simulation to describe the dynamic response of power system elements during transient events. Both methods can be used simultaneously because one method can provide inaccurate results, which might cause the power system to be operated in overly conservative or optimistic manners [137].

6.2.1 Static Voltage Stability Analysis

Q-V and V-P methodologies are often used to determine the minimum required margin of active and reactive power to serve as voltage stability criteria [136]. Both methodologies are based on static power flow. V-P curves are used to calculate the maximum amount of real power that can be transmitted by a transmission line. On the other hand, the Q-V curve shows the sensitivity of the voltage with respect to the reactive power exchanges at a given bus. Critical outages reduce the margins of the reactive power transfer capability of transmission networks; therefore, reactive power should be studied to avoid voltage collapses.

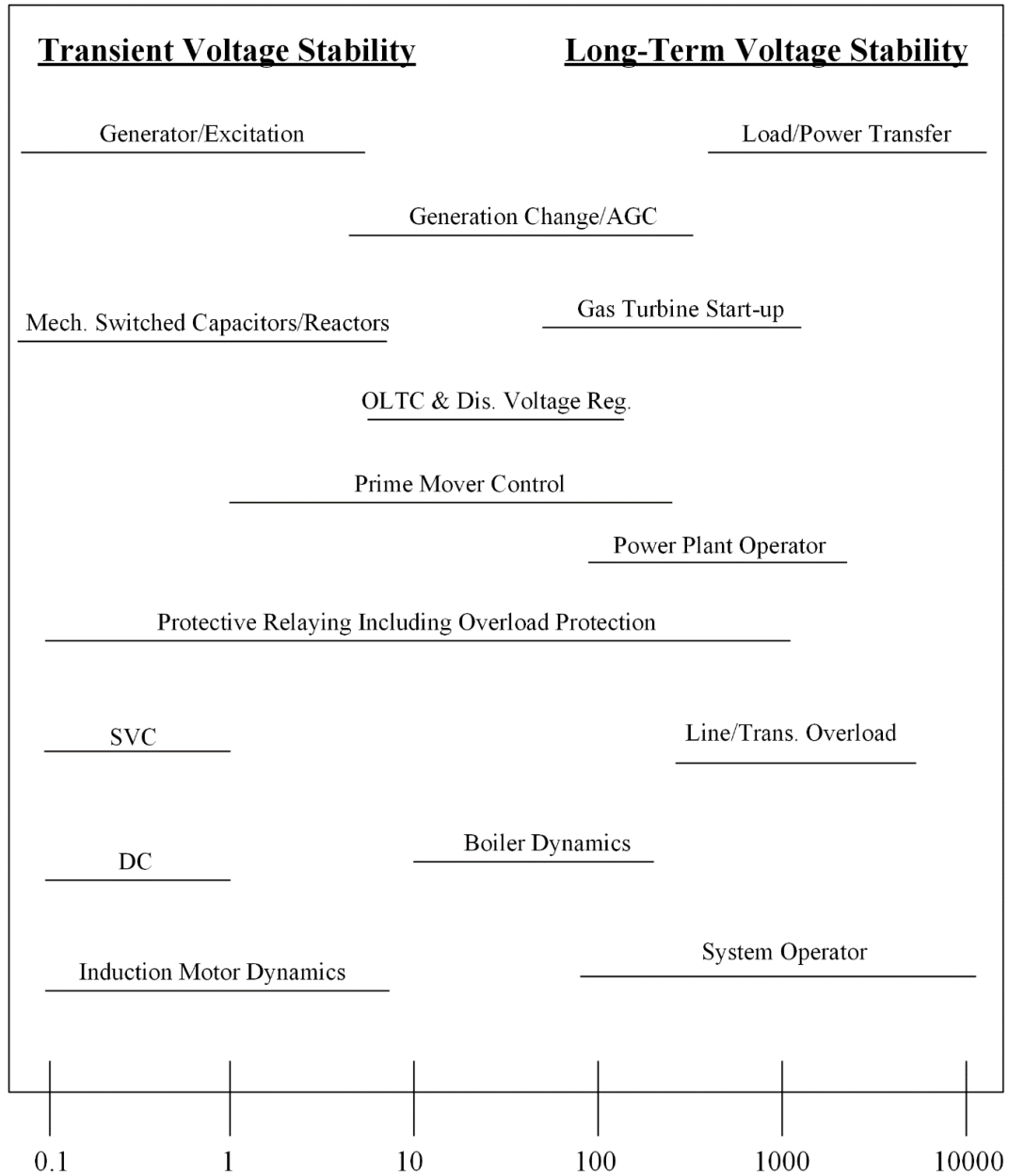


Figure 6.1. Time response of acting equipment in major disturbances [148].

To determine the reactive power margin requirements in the presence of a high penetration of PV in the power system. The Q-V method is used to calculate the reactive power margin at stressed buses. These buses could either have the lowest voltages or highest voltage deviations after a major power system outage. A simple power system is shown in Fig. 6.2 to

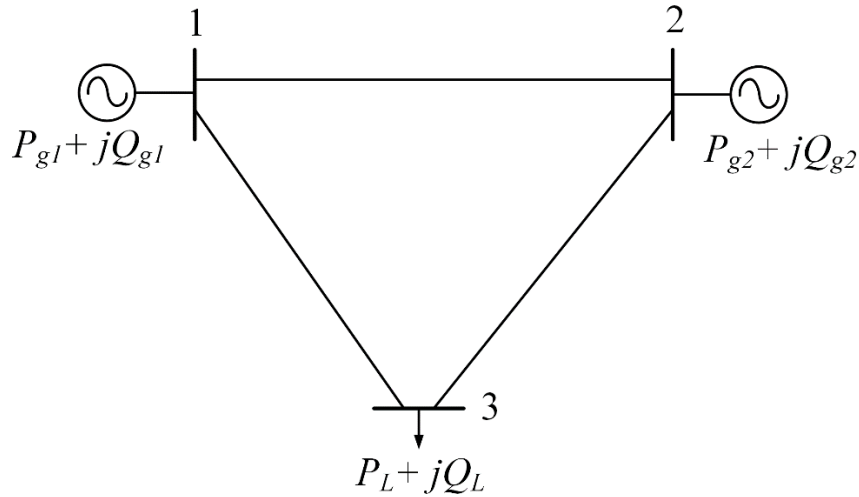


Figure 6.2. A simple power system.

explain the Q-V curve calculation. In the base case, an N-0 contingency is assumed, which means that all system elements are connected. Bus 3 is considered when creating the Q-V curve, by applying a fictitious synchronous condenser. This condenser is used to reduce the schedule voltage at Bus 3 in small steps. The output reactive power of the condenser and the voltage were recorded for each step. The voltage collapse point, $dQ/dV = 0$, represents the voltage stability limit. In addition, the reactive power margin of Bus 3 is defined by the condenser output Q at the collapse point [134]. Developing the Q-V curve for the most critical contingency is required to assess the reduction of the reactive power margin in this case. Fig. 6.3 shows the Q-V curves at Bus 3 for the base case and the most critical case. The reduction of the reactive power margin at Bus 3 is anticipated in the critical case. If the reactive power resources reached their maximum capability during a voltage emergency, voltage collapses might spread in stressed areas of the power system.

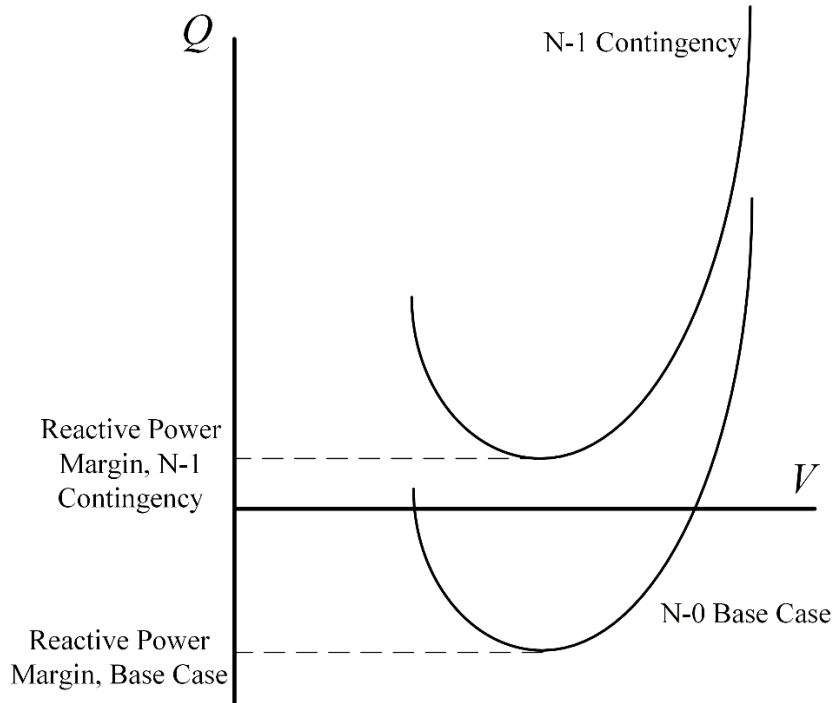


Figure 6.3. Q-V curves for the base case and N-1 contingency.

6.2.2 Dynamic Voltage Stability Analysis

The power system consists of many dynamic elements. To observe the response of the system elements during disturbances, a time-domain simulation can be performed. In time-domain simulations for stability studies, the power system is represented by a set of differential algebraic equations (DAE):

$$0 = g(x, y, u) \quad (6.1)$$

$$\dot{x} = f(x, y, u) \quad (6.2)$$

where x , y , and u represent the dynamic state, algebraic, and control variables, respectively. The modeling for long-term voltage stability includes detailed dynamic representations of synchronous generators, excitation systems, OLTCs, aggregated PV systems, and loads.

6.3 Models in Voltage Stability Analysis

6.3.1 Generator Model

Synchronous machines are represented by two-axis standard models. Hydro and thermal power plants are considered in the case study. GENSAL and GENROU are used to represent hydro and thermal generators respectively [143]. The HYGOV speed governor model is used for all hydro turbines [143].

6.3.2 PV Model

The representation of PV units depends on their size and contribution to the bulk power system. Modeling a large number of distributed PV systems in bulk power system studies is challenging. If the primary interest of the power flow study is to capture the impact of the reactive power support by PV systems, particularly voltage stability, the equivalent aggregated PV model can be used [144]. This PV model is connected to the transmission bus behind the OLTC transformer as well as the equivalent impedance, which represents the impedance of the medium-voltage feeder and secondary network. The WECC-recommended representation of high penetration of PV units in bulk power system studies is shown in Fig. 6.4.

To study the impacts of high PV penetration on voltage stability, the PV model should include converter control dynamic characteristics along with the electrical model. A PV model based on the generic wind turbine model (WT4) is commonly used in large interconnected power system studies and integrated by commercial power system software providers, such as PTI PSS/E, GE PSLF, and Power World Simulator. The second generation of the WT4 model

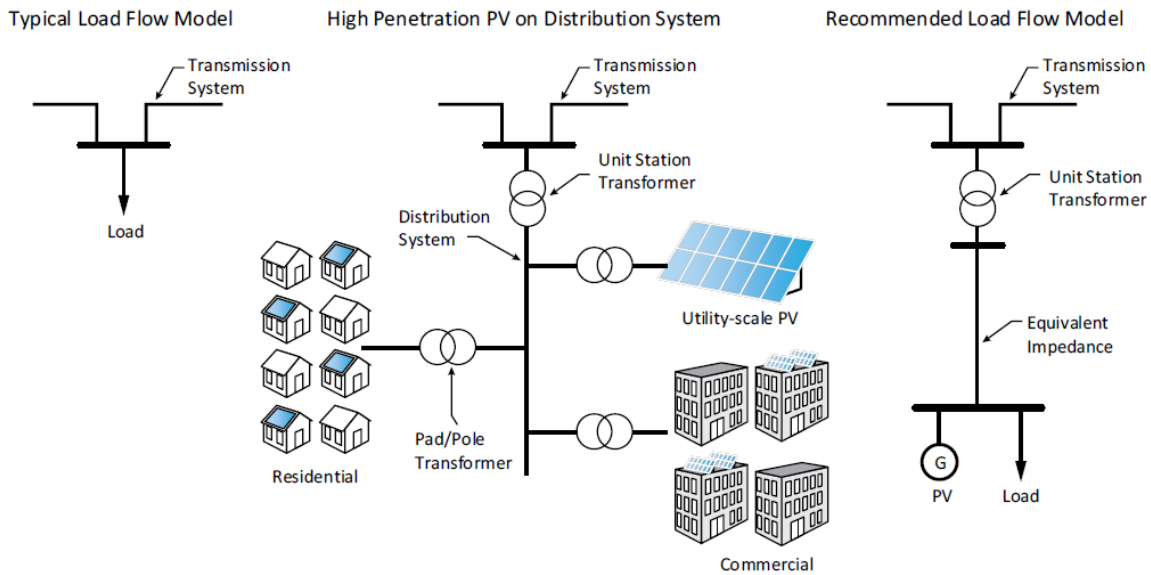


Figure 6.4. WECC-recommended representation of a high penetration of PV units in bulk power system studies [144].

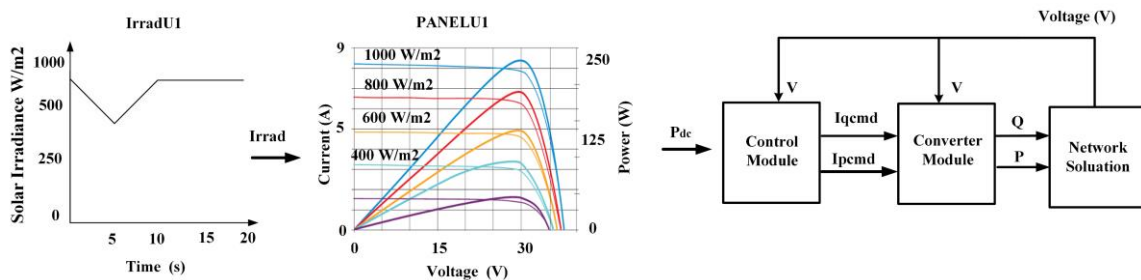


Figure 6.5. PV model diagram in PSS/E [143].

has been validated by the Renewable Energy Modeling Task Force (REMTF) of the WECC to represent PV systems in large-scale power system studies [144].

WT4 deploys a full converter unit that has the capability of controlling the generator output of active and reactive power. Fig. 6.5 shows the PV model diagram in PSS/E. IrradU1 is the solar radiation data, and it can be entered in table form. PANELU1 is the model of the PV array output power that calculates the maximum power tracking point for a given solar

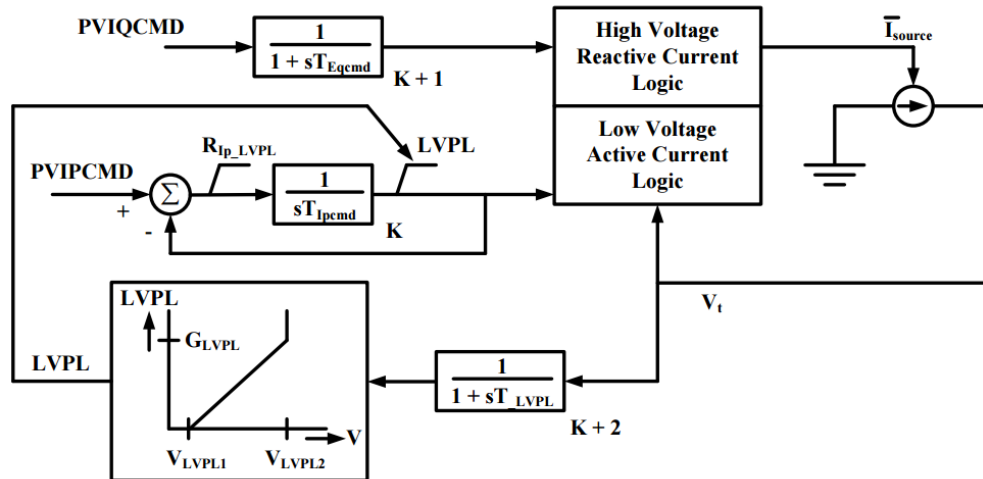


Figure 6.7. Converter module (PVGU) diagram in PSS/E [143].

The PVGU diagram is shown in Fig. 6.7. PVGU incorporates two current regulators to emulate the filtered active and reactive power command before the injection point with the grid. The flowchart of active and reactive current logic blocks is provided and explained in detail in [143].

6.3.3 Excitation System Model

The synchronous generator excitation system is responsible for control voltage and reactive power. It provides the major source of dynamic reactive power in the power system. The excitation system includes four subsystems: exciter, exciter regulator, power system stabilizer (PSS), and over-excitation limiter (OEL). Modeling excitation is the most important aspect of the time-domain simulation for the voltage stability assessment because the exciter control allows for a short-term overload capability of the generator to respond to disturbances.

When the excitation exceeds the limit, which is the rated field current, the OEL switches to decrease the field current to its rated value.

6.3.4 Transformer On-load Tap Changer Model

The dynamic model includes the mechanism of tap movements to regulate the voltage at the distribution bus. The time delay is used to prevent tap movements during transient events. In a stressed power system, excessive OLTC operations contribute to voltage collapses within the system, because each tap movement requires more reactive power from the generators. This can lead to overloaded generators in the automatic excitation mode. If this occurs, the system becomes unable to meet the reactive power demand and suffers from progressive voltage decay, possibly leading to a voltage instability event. This process usually takes up to several minutes and falls under the category of long-term voltage stability. The OLTC1 model in PSS/E is used to represent the OLTC in dynamic simulations.

6.3.5 Load Model

The dynamic response of loads to transient voltage changes is fast. The aggregated loads must represent its dependency on voltage change. Therefore, it is common practice to use exponential load model in dynamics studies [145], which has the following general form:

$$P = P_0 \left(\frac{V}{V_0} \right)^\alpha \quad (6.3)$$

$$Q = Q_0 \left(\frac{V}{V_0} \right)^\beta \quad (6.4)$$

where V_0 is the initial voltage, α and β are load dependent exponents, while P_0 and Q_0 are the initial active and reactive powers.

6.4 Grid Control Architecture

In the classical layout of a power system, the short-term scheduling of generations includes two stages. The first stage is to plan the system for the next day, considering system operation constraints, such as planned outages, load forecast, and transmission system limitations. The second stage includes the real-time control, which is responsible for balancing supply and demand, and also monitoring the adequacy of contingency reserves, while recognizing operational system limits. Given the complexity of scheduling a large-scale penetration of highly variable DERs, the adoption of aggregators can be used to group DERs at the connection points to serve as an interface between DERs and the DSO. The DSO controls and monitors the distribution network to avoid operational violations. The DSO is located at the distribution bus of the main substation and can share the total demand and DERs' capacity as seen by the independent system operator (ISO). Accordingly, the ISO dispatches generation signals based on economic dispatch considerations.

In this work, DERs in the form of PV are considered because their installations take place mostly in the distribution networks. PV systems can exchange reactive power with the grid and provide reactive power reserves to support the grid in contingency conditions. The total PV reactive power reserve in the distribution network at the point of interconnection (POI) with the transmission network can be optimized by the DSO and shared with the ISO. Therefore, the ISO can include the reactive power reserve in the planning and operation of the system.

This research assumed the DERs can provide support to the transmission network by injecting reactive power to the local loads. To prevent voltage instability incidents, the ISO

should assess the adequacy of the reactive power reserves to cover the system demand after major outages, including lines, generators, and Var compensators. Accordingly, contingency analysis in response to North American Electric Reliability Corporation (NERC)/WECC N-1 and N-1-1 criteria must be carried out to identify and rank the most critical buses with the lowest voltage for the selected contingencies [146]. In this study, the Q-V method was applied to assess the reactive power margin required for the critical buses at the collapse point ($dQ/dV = 0$). In addition, the dynamic simulation was performed to assess the long-term voltage stability. If the results would show that the system is unstable, corrective actions must be implemented to prevent widespread voltage collapse. Fig. 6.8 presents a flowchart of the voltage stability assessment related to scheduling PV generation.

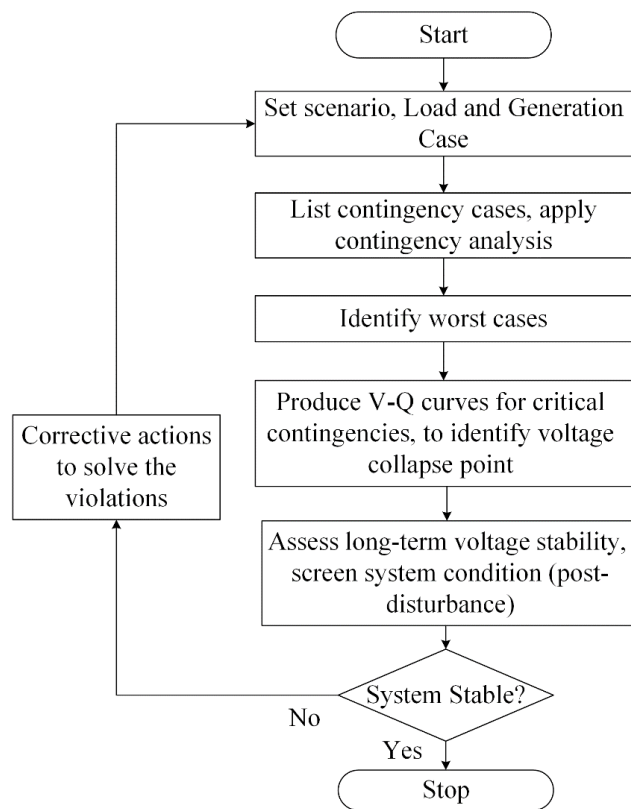


Figure 6.8. Voltage stability assessment flowchart.

6.5 Case Study

To investigate the impact of high PV penetration in the bulk power system, the Nordic network was used as a test system [147]. The test system was modified to integrate a large level of PV penetration, mainly, in the central area, as it is heavily loaded. The 20 kV distribution buses were selected as the location for PV installations. To comply with WECC modeling guidelines in large-scale power flow simulations, aggregated PV systems were represented by equivalent PV generators behind step-down transformers and equivalent feeder impedances, and were connected to medium-voltage buses at transmission substations [144]. Fig. 6.9 shows the modified Nordic32 test system.

6.5.1 Q-V Curve Simulation

The base case starts by lowering the generation output of G15 and G16 by 600 MW because they have the least impact on the central area compared to the remaining generators based on the contingency analysis. The total scheduled PV generation at the selected event was 1300 MW (around 10% of the total generation). In the base case (pre-contingency), the system operated normally, without violations. To screen and locate the most critical outage in the case study, contingency analysis was applied. The loss of G6 was the most critical outage in the central area. Bus 1042 had the most voltage deviation. The reactive power margin of the critical bus was calculated using PSS/E in the five cases, including the base case, as follows:

- Base case (pre-contingency): All elements were in service, and the PV systems operated at unity power factor.

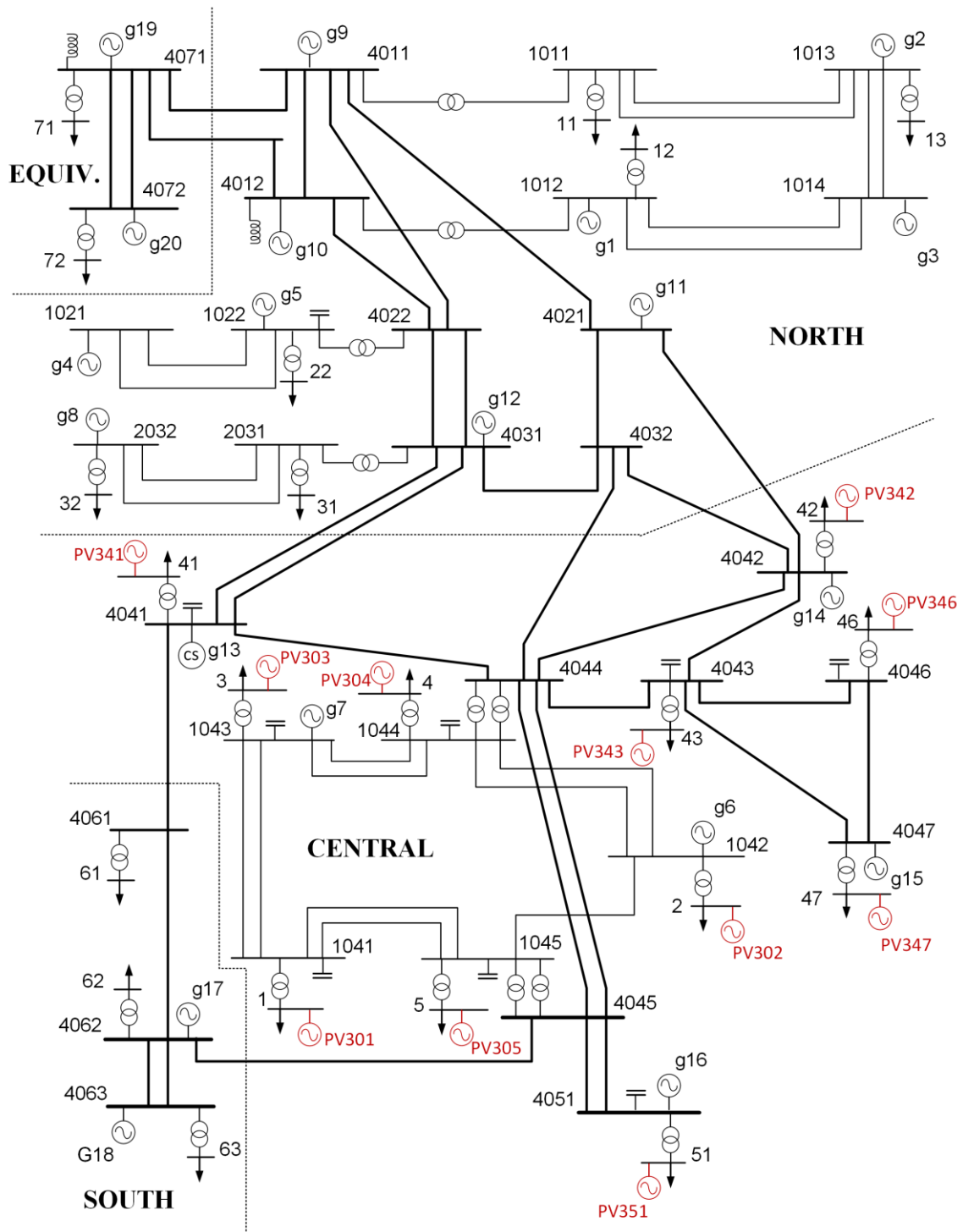


Figure 6.9. Modified Nordic test system.

- Case 1: The system operated with the loss of G6, and PV systems operated at unity power factor.
- Case 2: The system operated with the loss of G6, and PV systems had dispatchable reactive power reserves (Q_d^{res}) of 10% of the installation's capacity.
- Case 3: Similar to Case 2, except Q_d^{res} was 20% of the PV installation's capacity.
- Case 4: Similar to Case 2, except Q_d^{res} was 30% of the PV installation's capacity.

Table 6.1 lists the details of the PV generation data in the considered cases. The Q-V analysis was performed for the base case and post-contingency cases, as shown in Fig. 6.10. Table 6.2 summarizes the reactive power margin at the critical bus in the considered scenarios.

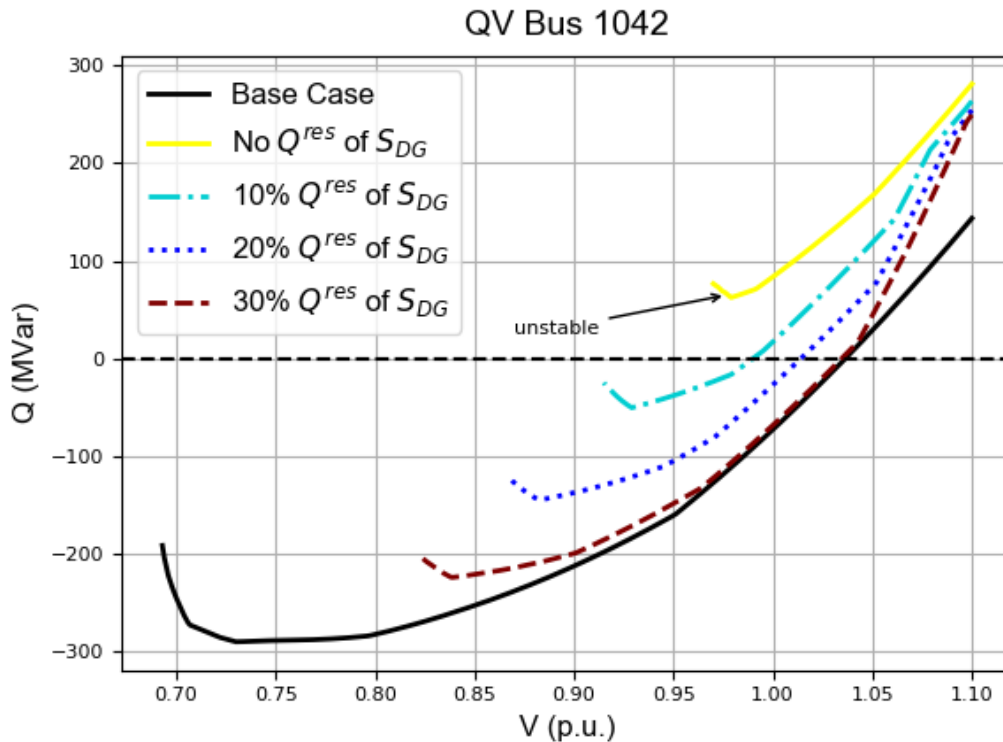


Figure 6.10. Q-V curves at Bus 1042.

In Case 1, the negative reactive power margin was an indication of voltage instability due to a reactive power deficit in the central area. The voltage stability limit can be improved by providing reactive power from local sources. Q-V curves showed that by leveling up the local reactive power reserves, the reactive power margin increased in the considered cases.

Table 6.1. PV Generation Data for 10% Penetration.

PV #	$S_{PV,cap}$ (MVA)	$P_{PV,gen}$ (MW)	$Q_{PV,res}$ (MVar)		
			Case 2	Case 3	Case 4
301	200	150	20	40	60
302	150	100	15	30	45
303	60	40	6	12	18
304	250	200	25	50	75
305	250	200	25	50	75
341	200	150	20	40	60
342	200	150	20	40	60
346	200	150	20	40	60
347	60	40	6	12	18
351	200	150	20	40	60

Table 6.2. Reactive Power Margin at Bus 1042.

Reactive Power Margin (MVar)				
Base Case	Case 1	Case 2	Case 3	Case 4
290	-60	45	130	220

6.5.2 Dynamic Simulation

To monitor the dynamic response of power system elements after being subjected to a disturbance, dynamic simulations were conducted using PSS/E to verify the Q-V results. The dynamic models of the system elements are detailed in [147]. Three cases will be considered in this section. In the first and second cases, reactive power support from DGs was not considered, while in the third case, it was considered.

Case 1: Fig. 6.11 shows two voltage profiles at Buses 2 and 1042 in the case without reactive power support from the DGs. At $t = 10$ s, the voltage dropped due to the loss of G6. The OLTC started to restore the voltage at Bus 2, leading to a progressive decline in the voltage at Bus 1042. Although the voltage at Bus 2 dropped below the permissible level, it was still

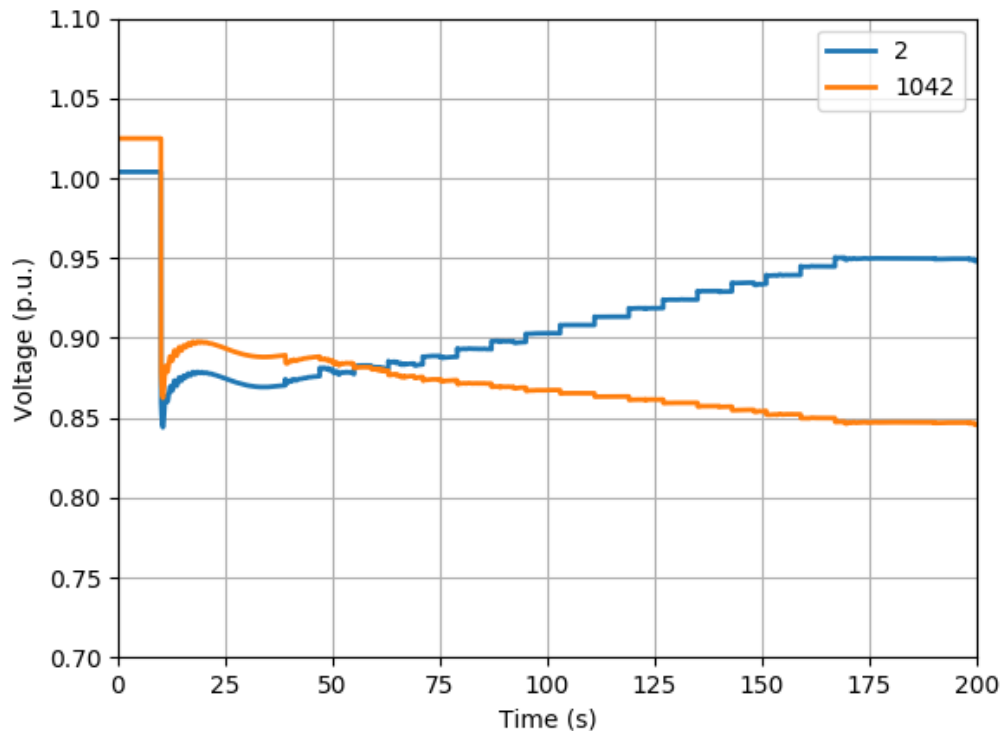


Figure 6.11. Case 1: Voltage at Buses 2 and 1042.

considered to be a local voltage problem and would not have led to a system collapse. This emphasizes the need for a time-domain simulation to indicate the global reactive power compensation compared with the Q-V method, which in this case indicates only the local reactive power compensation. The reactive power support could prevent the progressive voltage drop during this disturbance, which will be presented in the third case.

Case 2: In this case, the disturbance consisted of two generators that tripped off the network. G6 was tripped off at $t = 10$ s, and G14 was tripped off at $t = 30$ s. The OLTC was activated at $t = 50$ s to restore the voltage, leading to a progressive decline, as shown in Fig 6.12. At $t = 110$ s and $t = 178$ s, the OELs at G7 and G15 were activated, respectively, to reduce their

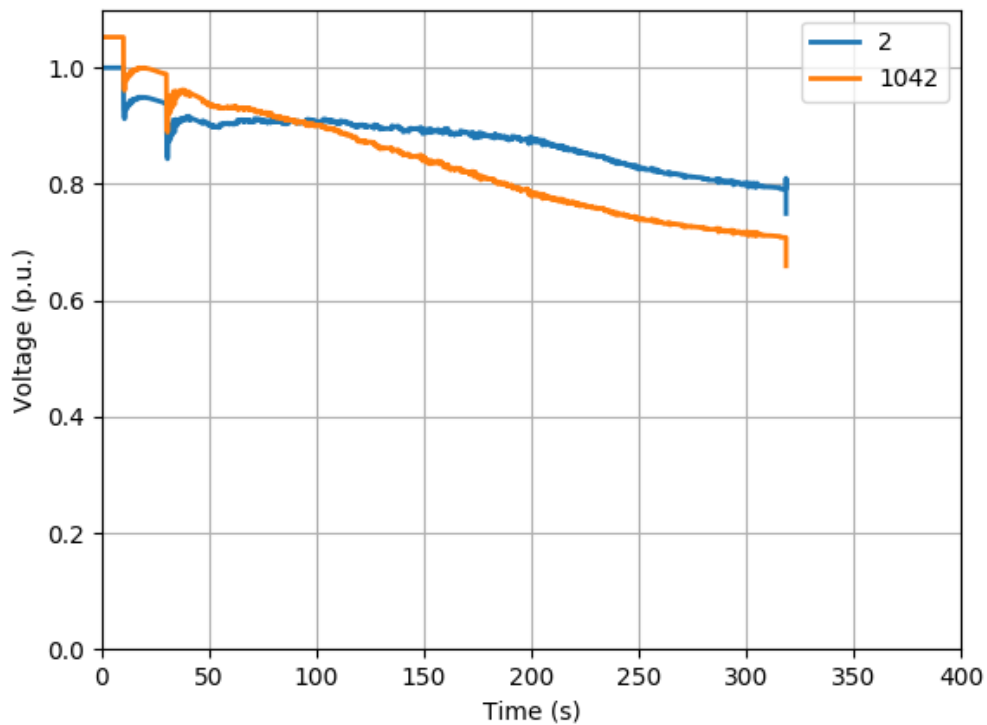


Figure 6.12. Case 2: Voltage at Buses 2 and 1042.

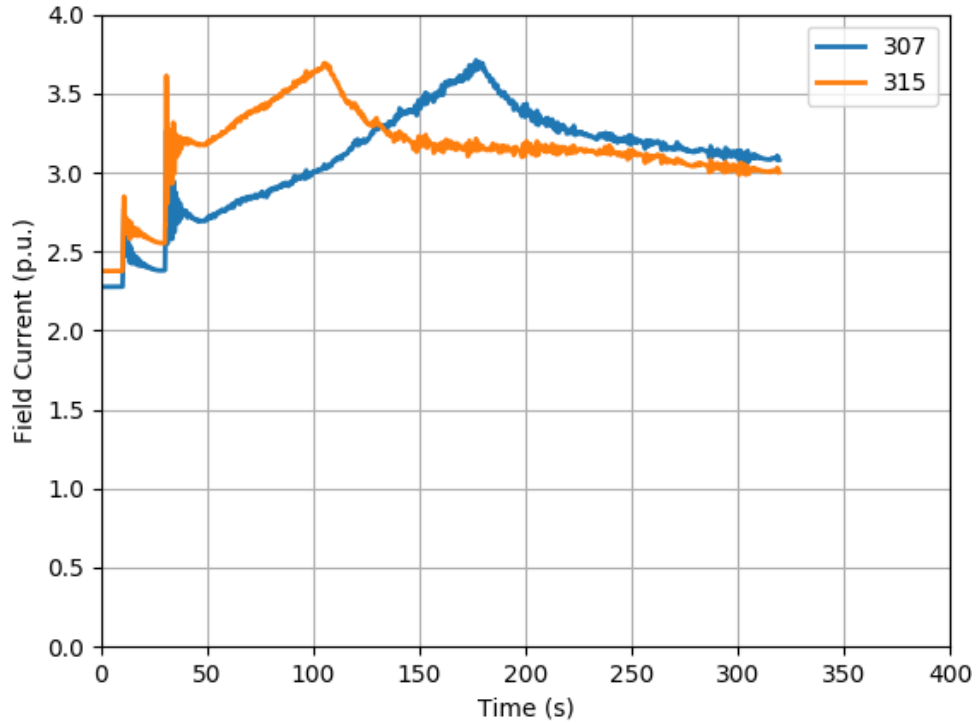


Figure 6.13. Case 2: Field current of G7 and G15.

reactive power outputs, as shown in Fig. 6.13. The system was severely stressed and collapsed at $t = 320$ s.

Case 3: This case considered the reactive power support by the DGs. The voltage profiles at Buses 2 and 1042 are shown in Fig. 6.14. The voltages dropped at $t = 10$ s and at $t = 30$ s, when G6 and G14 were tripped off. The reactive power produced by the equivalent model of PV302 (connected to Bus 2) is shown in Fig. 6.15. It started to inject reactive power in response to the voltage drop to support the grid, and the reactive power output reached the steady-state value (45 MVar) 40 s after the second disturbance. The OLTC was not activated because the reactive power support by the DGs responds rapidly to voltage variation, while the OLTC was delayed by 30 s. In addition, the field current output of G7 and G15 are below the over-excitation limit as shown in Fig. 6.16.

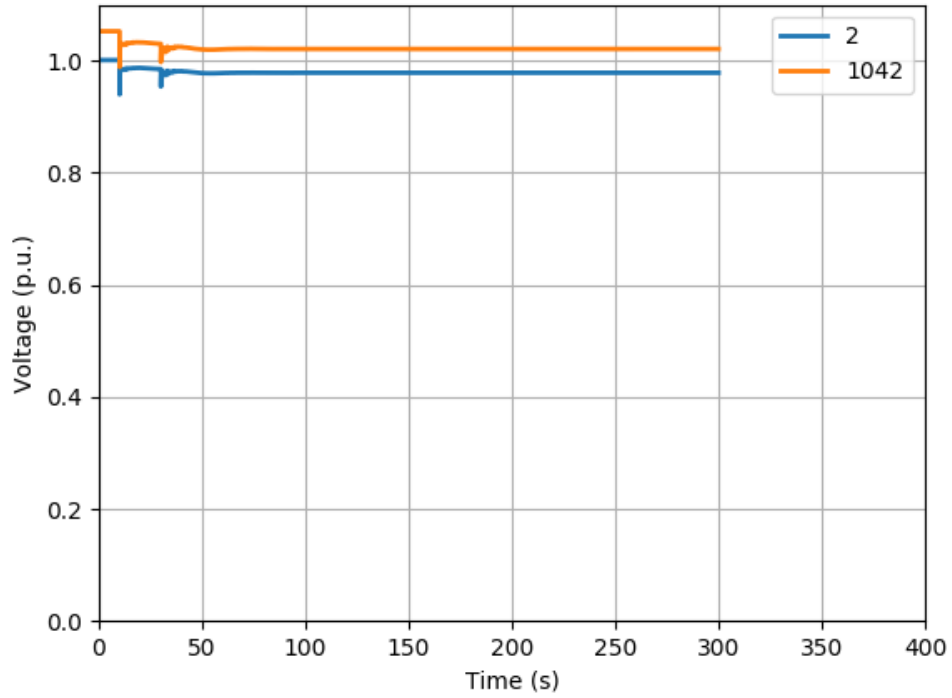


Figure 6.14. Case 3: Voltage at Buses 2 and 1042.

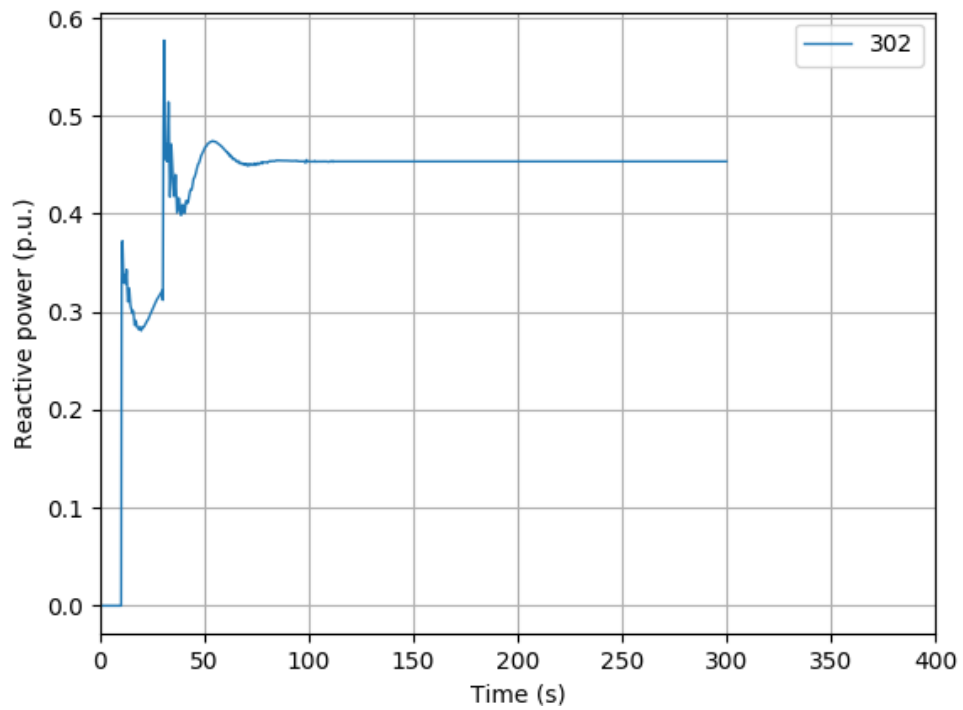


Figure 6.15. Case 3: Reactive power produced by PV302 (System base: 100 MVA).

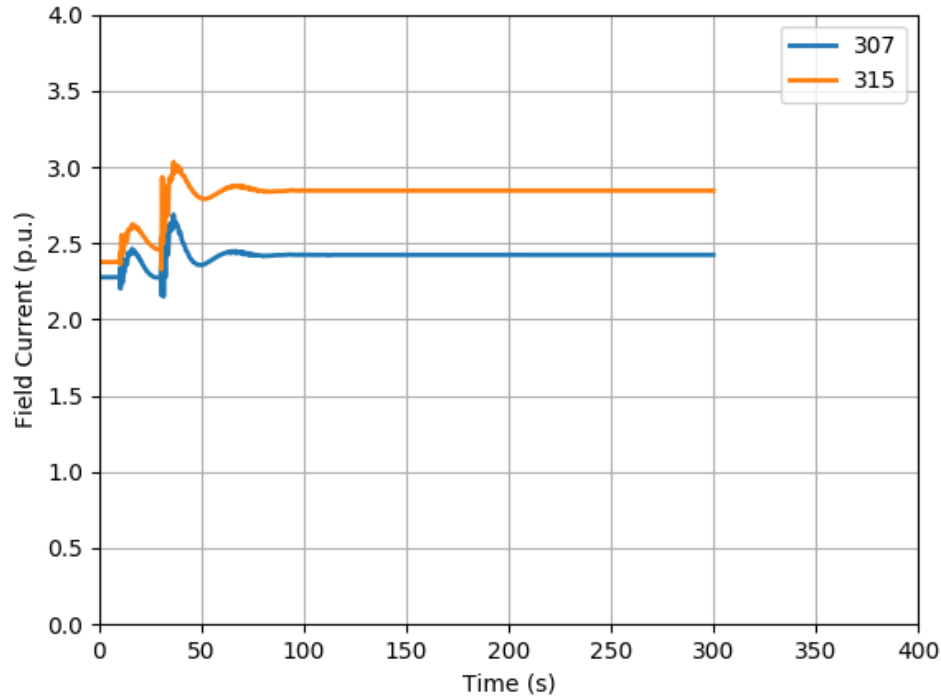


Figure 6.16. Case 3: Field current of G7 and G15.

6.6 Conclusion

This chapter discusses the potential impact of high DG penetration on the operation of the bulk power system, particularly, voltage stability. The ISO is responsible for assessing the reactive power margins throughout the power system. The DSO is assumed to be able to allocate reactive power sharing and dispatch local control parameters among DGs. The DGs can increase their reactive power output to support the transmission network after disturbances to prevent voltage instability.

Contingency analysis was performed on the studied system to identify the most critical bus. To investigate the impact of supplying reactive power by DGs on voltage stability, Q-V analysis was used to determine the reactive power margin at the critical bus for various reactive

power levels of support up to 30% of the total PV capacity. The results showed that when PV systems generate active power at unity power factor, the system was more vulnerable to voltage instability at the critical bus.

To study the impact of providing reactive power support by DGs on the long-term voltage stability of the bulk power system, a time-domain simulation of a severe contingency N-1-1 was carried out using PSS/E. The results show that scheduling reactive power reserves of DGs can mitigate voltage instability in disturbances.

7 Summary and Future Work

7.1 Summary

This section summarizes the work presented in this dissertation, which has addressed the impact of integrating distributed generation in the power grid, especially the study of Volt/Var control in distribution networks with high PV penetration. Six chapters have been presented in this dissertation and are summarized below:

- Chapter 1 provided some background for the research. It identified several operational challenges of distributed generation, which served as the motivation for the research. This chapter contained the research objectives and report outlines.
- Chapter 2 offered a detailed discussion of inverter control, the inverter thermal model, and the rainflow algorithm for inverter lifetime estimation. The inverter control in the grid-connected mode was used widely in this research. This chapter presented a case study that investigated the effect of temperature variations on inverter lifetime.
- Chapter 3 presented a harmonic elimination method for single-phase DG synchronization with a distorted grid. An SDFT-based prefilter was incorporated with the PLL to remove the effect of harmonics from the input voltage. The filter could selectively extract the fundamental frequency component, thereby eliminating the steady-state error and enabling the PLL to operate at a high bandwidth. Therefore, a good dynamic performance could be achieved during disturbances.
- Chapter 4 discussed voltage regulation methods in distribution networks with high DG. A Volt/Var control strategy was proposed to regulate the voltage throughout the

distribution network. It included solving for the optimal power flow to minimize both the distribution system losses and the additional inverter power losses that resulted from exchanging reactive power in voltage regulation so as to relieve the thermal stress on the inverters. Therefore, it allowed for optimal reactive power allocation among DGs because owners of DGs are not compensated for their inverter overutilization. The thermal model of an inverter was applied to estimate the power loss in inverter switches. A radial distribution feeder with high PV penetration was employed as a test system to investigate the effectiveness of the proposed control strategy for long-term mission profiles. The rainflow algorithm was used to count the temperature cycles to analyze the impact of temperature variations on switch lifetime using a reliability-based fatigue model. The simulation results revealed that the proposed control strategy is capable of regulating the voltage, while it also relieves the thermal stress on the inverters, which improves their reliability.

- Chapter 5 examined the impact of PV uncertainty on voltage fluctuations. It was proposed that the reactive power capacity of the DGs be scheduled at two levels: local and central. The central control optimized the set points of the reactive power DGs to keep voltages within allowable limits. To mitigate the production uncertainties of renewables, a scenario-based approach was employed by the central control to optimize the local controllers' parameters. The MCS was incorporated to generate sets of possible scenarios for PV output based on the stochastic model of PV systems. To reduce the computational complexity, the BR algorithm was used to reduce the number of scenarios to a manageable quantity, while maintaining good approximation. The test system discussed in Chapter 4 was also used to examine the effectiveness of the proposed

strategy in mitigating overvoltage issues. Reliability analysis was conducted to estimate the total damage of the inverters that were switched in the obtained thermal profile.

- Chapter 6 focused on long-term voltage stability assessment and enhancement in power systems with a high penetration of distributed PVs. In stressed systems, proper management of reactive power reserves provided by DGs can support the upstream network after a severe disturbance. In this work, Q-V analysis and dynamic time-domain simulation were used to assess the adequacy of reactive reserves in the tested system. The case study was performed on a modified Nordic32 test system.

7.2 Future Work

- The performance of the proposed grid synchronization method in Chapter 3 could be further investigated during over- and under-frequency events. It is necessary to accurately track the frequency amplitude to satisfy the frequency ride-through (FRT) operation requirements for DGs under distorted voltage conditions.
- In conventional distribution networks, OLTCs play the main role in voltage control. However, the presence of intermittent renewable energy sources, such as PV, contributes to high voltage fluctuation in distribution networks, which results in excessive operation of OLTCs. Therefore, in the future, the Volt/Var control strategies discussed in Chapters 4 and 5 should incorporate minimizing the corrective actions by OLTCs.
- Both Volt/Var control strategies presented in Chapters 4 and 5 were applied to a balanced, three-phase distribution system. However, in practice, distribution feeders serve a large numbers of single-phase, residential loads, which often cause the current to be unbalanced throughout the system. Consequently, a case study using an unbalanced

distribution test system can be applied in the future to investigate the effectiveness of these strategies with voltage/current unbalance.

- Most failures in inverters are caused by the simultaneous degradation of more than one element (e.g., IGBTs, capacitors, contactors, etc.). In addition, the causes of the IGBTs degradation can be a combination of two or more failure modes when different stresses are applied to the devices, such as thermal, electrical, mechanical, and external stress (e.g., humidity). However, in the literature, only the effect of thermal stress on power electronics devices from the reactive power supply was considered when modeling the lifetime of a semiconductor. Therefore, a multi-failure mode model can be developed in the future to improve the accuracy of failure prediction.
- In Chapter 6, the aggregated dynamic PV model was used to capture the impact on voltage stability of supplying reactive power by DGs. While this model reduces the computational burden of dynamic power flow studies, it is difficult to approximate the effects of such a large number of distributed PVs scattered throughout the distribution network with the aggregated model. More detailed models of distribution networks should be considered in the future. For example, the aggregated dynamic PV and load models can be replaced by several microgrids.

REFERENCES

- [1] R. Fu, D. Feldman, R. Margolis, M. Woodhouse, and K. Ardani, “U.S. solar photovoltaic system cost benchmark: Q1 2017,” *NREL*, 2017.
- [2] P. Aristidou, G. Valverde, and T. Van Cutsem, “Contribution of distribution network control to voltage stability: A case study,” *IEEE Trans. Smart Grid*, vol. 8, no. 1, pp. 106–116, Jan. 2017.
- [3] X. Wu, J. He, Y. Xu, J. Lu, N. Lu, and X. Wang, “Hierarchical control of residential HVAC units for primary frequency control,” *IEEE Trans. Smart Grid*, pp. 1–1, 2017.
- [4] Task Force on Contribution to Bulk System Control and Stability, *Contribution to Bulk System Control and Stability by Distributed Energy Resources Connected at Distribution Network*. 2017.
- [5] NERC Distributed Energy Resources Task Force, “Distributed energy resources connection modeling and reliability considerations,” Atlanta, 2016.
- [6] J. von Appen, M. Braun, T. Stetz, K. Diwold, and D. Geibel, “Time in the sun: the challenge of high PV penetration in the German electric grid,” *IEEE Power Energy Mag.*, vol. 11, no. 2, pp. 55–64, Mar. 2013.
- [7] Y. F. Wang and Y. W. Li, “Fast harmonic detection based on cascaded delayed signal cancellation PLL,” in *2011 IEEE Energy Conversion Congress and Exposition*, 2011, pp. 1094–1101.
- [8] C. Ma, F. Gao, G. He, and G. Li, “A voltage detection method for the voltage ride-through operation of renewable energy generation systems under grid voltage distortion conditions,” *IEEE Trans. Sustain. Energy*, vol. 6, no. 3, pp. 1131–1139, 2015.
- [9] Y. F. Wang and Y. W. Li, “Three-phase cascaded delayed signal cancellation PLL for fast selective harmonic detection,” *IEEE Trans. Ind. Electron.*, vol. 60, no. 4, pp. 1452–1463, 2013.

- [10] *American National Standard for Electric Power Systems and Equipment—Voltage Ratings (60 Hertz)*. ANSI C84.1-2011, American National Standards Institute, Inc., 2011.
- [11] “IEEE Standard for Interconnecting Distributed Resources with Electric Power Systems - Amendment 1,” *IEEE Std 1547a-2014 (Amendment to IEEE Std 1547-2003)*, pp. 1–16, 2014.
- [12] Y.-K. Wu, J.-H. Lin, and H.-J. Lin, “Standards and guidelines for grid-connected photovoltaic generation systems: A review and comparison,” *IEEE Trans. Ind. Appl.*, vol. 53, no. 4, pp. 3205–3216, Jul. 2017.
- [13] H. G. Yeh, D. F. Gayme, and S. H. Low, “Adaptive VAR control for distribution circuits with photovoltaic generators,” *IEEE Trans. Power Syst.*, vol. 27, no. 3, pp. 1656–1663, Aug. 2012.
- [14] S. Alyami, Y. Wang, C. Wang, J. Zhao, and B. Zhao, “Adaptive real power capping method for fair overvoltage regulation of distribution networks with high penetration of PV systems,” *IEEE Trans. Smart Grid*, vol. 5, no. 6, pp. 2729–2738, Nov. 2014.
- [15] D. Ranamuka, A. P. Agalgaonkar, and K. M. Muttaqi, “Online coordinated voltage control in distribution systems subjected to structural changes and DG availability,” *IEEE Trans. Smart Grid*, pp. 1–12, 2015.
- [16] Z. Wang, J. Wang, B. Chen, M. M. Begovic, and Y. He, “MPC-based voltage/var optimization for distribution circuits with distributed generators and exponential load models,” *IEEE Trans. Smart Grid*, vol. 5, no. 5, pp. 2412–2420, Sep. 2014.
- [17] F. Bai, R. Yan, T. K. Saha, and D. Eghbal, “new remote tap position estimation approach for open-delta step-voltage regulator in a photovoltaic integrated distribution network,” *IEEE Trans. Power Syst.*, pp. 1–1, 2017.
- [18] T. Ding, S. Liu, W. Yuan, Z. Bie, and B. Zeng, “A two-stage robust reactive power optimization considering uncertain wind power integration in active distribution networks,” *IEEE Trans. Sustain. Energy*, vol. 7, no. 1, pp. 301–311, Jan. 2016.

- [19] S. Ghosh, S. Rahman, and M. Pipattanasomporn, "Distribution voltage regulation through active power curtailment with PV inverters and solar generation forecasts," *IEEE Trans. Sustain. Energy*, vol. 8, no. 1, pp. 13–22, Jan. 2017.
- [20] A. Anurag, Y. Yang, and F. Blaabjerg, "Thermal performance and reliability analysis of single-phase PV inverters with reactive power injection outside feed-in operating hours," *IEEE J. Emerg. Sel. Top. Power Electron.*, vol. 3, no. 4, pp. 870–880, Dec. 2015.
- [21] J. von Appen, T. Stetz, M. Braun, and A. Schmiegel, "Local voltage control strategies for PV storage systems in distribution grids," *IEEE Trans. Smart Grid*, vol. 5, no. 2, pp. 1002–1009, Mar. 2014.
- [22] Y. Deng, Y. Tao, G. Chen, G. Li, and X. He, "Enhanced power flow control for grid-connected droop-controlled inverters with improved stability," *IEEE Trans. Ind. Electron.*, vol. 64, no. 7, pp. 5919–5929, Jul. 2017.
- [23] G. Valverde and T. Van Cutsem, "Model predictive control of voltages in active distribution networks," *IEEE Trans. Smart Grid*, vol. 4, no. 4, pp. 2152–2161, Dec. 2013.
- [24] V. Kekatos, G. Wang, A. J. Conejo, and G. B. Giannakis, "Stochastic reactive power management in microgrids with renewables," *IEEE Trans. Power Syst.*, vol. 30, no. 6, pp. 3386–3395, Nov. 2015.
- [25] B. Tamimi, C. Canizares, and K. Bhattacharya, "Modeling and performance analysis of large solar photo-voltaic generation on voltage stability and inter-area oscillations," in *2011 IEEE Power and Energy Society General Meeting*, 2011, pp. 1–6.
- [26] S. Eftekharnejad, V. Vittal, G. T. Heydt, B. Keel, and J. Loehr, "Small signal stability assessment of power systems with increased penetration of photovoltaic generation: A case study," *IEEE Trans. Sustain. Energy*, vol. 4, no. 4, pp. 960–967, 2013.
- [27] K. Kawabe and K. Tanaka, "Impact of dynamic behavior of photovoltaic power generation systems on short-term voltage stability," *IEEE Trans. Power Syst.*, vol. 30, no. 6, pp. 3416–3424, Nov. 2015.

- [28] F. Famoso, R. Lanzafame, S. Maenza, and P. F. Scandura, "Performance comparison between micro-inverter and string-inverter photovoltaic systems," *Energy Procedia*, vol. 81, pp. 526–539, Dec. 2015.
- [29] A. Ristow, M. Begovic, A. Pregelj, and A. Rohatgi, "Development of a methodology for improving photovoltaic inverter reliability," *IEEE Trans. Ind. Electron.*, vol. 55, no. 7, pp. 2581–2592, Jul. 2008.
- [30] A. M. Noman, A. A. Al-Shamma'a, K. E. Addoweesh, A. A. Alabduljabbar, and A. I. Alolah, "A survey on two level and cascaded multilevel inverter topologies for grid connected PV system," in *IECON 2017 - 43rd Annual Conference of the IEEE Industrial Electronics Society*, 2017, pp. 2369–2376.
- [31] H. Choi, W. Zhao, M. Ciobotaru, and V. G. Agelidis, "Large-scale PV system based on the multiphase isolated DC/DC converter," in *Proceedings - 2012 3rd IEEE International Symposium on Power Electronics for Distributed Generation Systems, PEDG 2012*, 2012, pp. 801–807.
- [32] F. Filho, Y. Cao, and L. M. Tolbert, "11-level cascaded H-bridge grid-tied inverter interface with solar panels," in *Conference Proceedings - IEEE Applied Power Electronics Conference and Exposition - APEC*, 2010, pp. 968–972.
- [33] Z. Malekjamshidi, M. Jafari, M. R. Islam, and J. Zhu, "A comparative study on characteristics of major topologies of voltage source multilevel inverters," in *2014 IEEE Innovative Smart Grid Technologies - Asia (ISGT ASIA)*, 2014, pp. 612–617.
- [34] S. Fukuda and T. Yoda, "A novel current-tracking method for active filters based on a sinusoidal internal model," *IEEE Trans. Ind. Appl.*, vol. 37, no. 3, pp. 888–895, 2001.
- [35] X. Yuan, W. Merk, H. Stemmler, and J. Allmeling, "Stationary-frame generalized integrators for current control of active power filters with zero steady-state error for current harmonics of concern under unbalanced and distorted operating conditions," in *IEEE Transactions on Industry Applications*, 2002, vol. 38, no. 2, pp. 523–532.

- [36] Q. Yao and D. G. Holmes, "A simple, novel method for variable-hysteresis-band current control of a three phase inverter with constant switching frequency," *Conf. Rec. 1993 IEEE Ind. Appl. Conf. Twenty-Eighth IAS Annu. Meet.*, pp. 1122–1129, 1993.
- [37] P. Rodríguez, J. Pou, J. Bergas, J. I. Candela, R. P. Burgos, and D. Boroyevich, "Decoupled double synchronous reference frame PLL for power converters control," *IEEE Trans. Power Electron.*, vol. 22, no. 2, pp. 584–592, 2007.
- [38] L. Malesani and P. Tenti, "A novel hysteresis control method for current-controlled voltage-source PWM inverters with constant modulation frequency," *IEEE Trans. Ind. Appl.*, vol. 26, no. 1, pp. 88–92, 1990.
- [39] S. R. Bowes and S. Grewal, "Three-level hysteresis band modulation strategy for single-phase PWM inverters," *Electr. Power Appl. IEE Proc. -*, vol. 146, no. 6, pp. 695–706, 1999.
- [40] B. Li, W. Yao, L. Hang, and L. M. Tolbert, "Robust proportional resonant regulator for grid-connected voltage source inverter (VSI) using direct pole placement design method," *IET Power Electron.*, vol. 5, no. 8, p. 1367, 2012.
- [41] K. H. Ahmed, A. M. Massoud, S. J. Finney, and B. W. Williams, "A modified stationary reference frame-based predictive current control with zero steady-state error for LCL coupled inverter-based distributed generation systems," *IEEE Trans. Ind. Electron.*, vol. 58, no. 4, pp. 1359–1370, Apr. 2011.
- [42] T. Hornik and Q. C. Zhong, "A current-control strategy for voltage-source inverters in microgrids based on H_∞ and Repetitive Control," *IEEE Trans. Power Electron.*, vol. 26, no. 3, pp. 943–952, 2011.
- [43] Y. Sozer and D. A. Torrey, "Modeling and control of utility interactive inverters," *IEEE Trans. Power Electron.*, vol. 24, no. 11, pp. 2475–2483, 2009.
- [44] F. Blaabjerg, R. Teodorescu, M. Liserre, and A. V. Timbus, "Overview of control and grid synchronization for distributed power generation systems," *IEEE Transactions on Industrial Electronics*, vol. 53, no. 5, pp. 1398–1409, 2006.

- [45] D. C. Jordan and S. R. Kurtz, "Photovoltaic degradation rates - an analytical review," *NREL*, 2012.
- [46] A. Golnas, "PV system reliability: An operator's perspective," *IEEE J. Photovoltaics*, vol. 3, no. 1, pp. 416–421, 2013.
- [47] H. Wang, M. Liserre, and F. Blaabjerg, "Toward reliable power electronics: Challenges, design tools, and opportunities," *IEEE Ind. Electron. Mag.*, vol. 7, no. 2, pp. 17–26, 2013.
- [48] S. H. Ali, S. Dusmez, and B. Akin, "A comprehensive study on variations of discrete IGBT characteristics due to package degradation triggered by thermal stress," in *2016 IEEE Energy Conversion Congress and Exposition (ECCE)*, 2016, pp. 1–6.
- [49] F. Renken *et al.*, "Reliability of High Temperature Inverters for HEV," in *2007 Power Conversion Conference - Nagoya*, 2007, pp. 563–568.
- [50] P. D. Reigosa, H. Wang, Y. Yang, and F. Blaabjerg, "Prediction of bond wire fatigue of IGBTs in a PV inverter under a long-term operation," *IEEE Trans. Power Electron.*, vol. 31, no. 10, pp. 7171–7182, 2016.
- [51] A. Syed, "Predicting solder joint reliability for thermal, power, and bend cycle within 25% accuracy," in *2001 Proceedings. 51st Electronic Components and Technology Conference (Cat. No.01CH37220)*, pp. 255–263.
- [52] S. J. Ham, M. S. Cho, and S. B. Lee, "Thermal deformations of CSP assembly during temperature cycling and power cycling," in *International Symposium on Electronic Materials and Packaging (EMAP2000) (Cat. No.00EX458)*, pp. 350–357.
- [53] A. Ammous, S. Ghedira, B. Allard, H. Morel, and D. Renault, "Choosing a thermal model for electrothermal simulation of power semiconductor devices," *IEEE Trans. Power Electron.*, vol. 14, no. 2, pp. 300–307, Mar. 1999.
- [54] J. L. Hudgins, E. Santi, A. T. Bryant, P. R. Palmer, and H. A. Mantooth, "Transient electrothermal simulation of power semiconductor devices," *IEEE Trans. Power Electron.*, vol. 25, no. 1, pp. 237–248, 2010.

- [55] T. Gradinger and G. Riedel, "Thermal networks for time-variant cooling systems: modeling approach and accuracy requirements for lifetime prediction," *Integr. Power Electron. Syst. (CIPS), 2012 7th Int. Conf.*, vol. 9, pp. 1–6, 2012.
- [56] J. Sigg, P. Turkes, and R. Kraus, "Parameter extraction methodology and validation for an electro-thermal physics-based NPT IGBT model," *IAS '97. Conf. Rec. 1997 IEEE Ind. Appl. Conf. Thirty-Second IAS Annu. Meet.*, vol. 2, pp. 1166–1173 vol.2, 1997.
- [57] "FGH20N60UFD Datasheet." [Online]. Available: <https://www.fairchildsemi.com/datasheets/FG/FGH20N60UFD.pdf>. [Accessed: 29-Dec-2017].
- [58] A. Marinov and V. Valchev, "Power loss reduction in electronic inverters through IGBT-MOSFET combination," *Procedia Earth Planet. Sci.*, vol. 1, pp. 1539–1543, 2009.
- [59] M. Held, P. Jacob, G. Nicoletti, P. Scacco, and M. H. Poech, "Fast power cycling test for insulated gate bipolar transistor modules in traction application," *Int. J. Electron.*, vol. 86, no. 10, pp. 1193–1204, 1999.
- [60] K. L. Singh and V. R. Ranganath, "Cycle counting using rainflow algorithm for fatigue analysis," in *15th National Conference on Aerospace Structures*, 2007, pp. 1–6.
- [61] M. Musallam and C. M. Johnson, "An efficient implementation of the rainflow counting algorithm for life consumption estimation," *IEEE Trans. Reliab.*, vol. 61, no. 4, pp. 978–986, 2012.
- [62] L. R. GopiReddy, L. M. Tolbert, B. Ozpineci, and J. O. P. Pinto, "Rainflow algorithm-based lifetime estimation of power semiconductors in utility applications," *IEEE Trans. Ind. Appl.*, vol. 51, no. 4, pp. 3368–3375, Jul. 2015.
- [63] M. Matsuishi and T. Endo, "Fatigue of metals subjected to varying stress," *Japan Soc. Mech. Eng.*, 1968.
- [64] ASTM E1049-85, *Standard practices for cycle counting in fatigue analysis*. 2011.
- [65] J. A. Bannantine, J. J. Comer, and J. L. Handrock, *Fundamentals of metal fatigue analysis*. Prentice Hall, 1990.

- [66] "Solar resources and meteorological assessment project." [Online]. Available: <https://www.nrel.gov/midc/ssrp/>. [Accessed: 29-Dec-2017].
- [67] X. Guo, W. Wu, and Z. Chen, "Multiple-complex coefficient-filter-based phase-locked loop and synchronization technique for three-phase grid-interfaced converters in distributed utility networks," *IEEE Trans. Ind. Electron.*, vol. 58, no. 4, pp. 1194–1204, 2011.
- [68] H. Awad, J. Svensson, and M. J. Bollen, "Tuning software phase-locked loop for series-connected converters," *IEEE Trans. Power Deliv.*, vol. 20, no. 1, pp. 300–308, 2005.
- [69] L. Xiong, F. Zhuo, X. Liu, F. Wang, and Y. Chen, "Optimal design of moving average filter and its application in distorted grid synchronization," in *2015 IEEE Energy Conversion Congress and Exposition (ECCE)*, 2015, pp. 3449–3454.
- [70] K.-J. Lee, J.-P. Lee, D. Shin, D.-W. Yoo, and H.-J. Kim, "A novel grid synchronization PLL method based on adaptive low-pass notch filter for grid-connected PCS," *IEEE Trans. Ind. Electron.*, vol. 61, no. 1, pp. 292–301, Jan. 2014.
- [71] S. K. Chung, "A phase tracking system for three phase utility interface inverters," *IEEE Trans. Power Electron.*, vol. 15, no. 3, pp. 431–438, 2000.
- [72] T. A. Youssef and O. Mohammed, "Adaptive SRF-PLL with reconfigurable controller for Microgrid in grid-connected and stand-alone modes," in *2013 IEEE Power & Energy Society General Meeting*, 2013, pp. 1–5.
- [73] H. A. Hamed, A. F. Abdou, E. H. E. Bayoumi, and E. E. EL-Kholy, "Frequency adaptive CDSC-PLL using axis drift control under adverse grid condition," *IEEE Trans. Ind. Electron.*, vol. 64, no. 4, pp. 2671–2682, Apr. 2017.
- [74] J. Jo, B.-M. Han, and H. Cha, "FPGA based DSC-PLL for grid harmonics and voltage unbalance effect elimination," in *2015 IEEE Applied Power Electronics Conference and Exposition (APEC)*, 2015, pp. 2212–2216.
- [75] F. Xiao, L. Dong, L. Li, and X. Liao, "Fast voltage detection method for grid-tied renewable energy generation systems under distorted grid voltage conditions," *IET Power Electron.*, vol. 10, no. 12, pp. 1487–1493, Oct. 2017.

- [76] F. A. S. Neves, M. C. Cavalcanti, H. E. P. De Souza, F. C. Bradaschia, E. J. Bueno, and M. Rizo, "A generalized delayed signal cancellation method for detecting fundamental-frequency positive-sequence three-phase signals," *IEEE Trans. Power Deliv.*, vol. 25, no. 3, pp. 1816–1825, 2010.
- [77] B. P. McGrath, D. G. Holmes, and J. J. H. Galloway, "Power converter line synchronization using a discrete Fourier transform (DFT) based on a variable sample rate," *IEEE Trans. Power Electron.*, vol. 20, no. 4, pp. 877–884, 2005.
- [78] E. Jacobsen and R. Lyons, "The sliding DFT," *IEEE Signal Processing Magazine*, vol. 20, no. 2, pp. 74–80, 2003.
- [79] D. Dong, B. Wen, D. Boroyevich, P. Mattavelli, and Y. Xue, "Analysis of phase-locked loop low-frequency stability in three-phase grid-connected power converters considering impedance interactions," *IEEE Trans. Ind. Electron.*, vol. 62, no. 1, pp. 310–321, 2015.
- [80] S. Golestan, J. M. Guerrero, and J. C. Vasquez, "Three-phase PLLs: A review of recent advances," *IEEE Transactions on Power Electronics*, vol. 32, no. 3, pp. 1897–1907, 2017.
- [81] S. Mishra, D. Das, R. Kumar, and P. Sumathi, "A power-line interference canceler based on sliding DFT phase locking scheme for ECG signals," *IEEE Trans. Instrum. Meas.*, vol. 64, no. 1, pp. 132–142, 2015.
- [82] F. A. Viawan and D. Karlsson, "Combined local and remote voltage and reactive power control in the presence of induction machine distributed generation," *IEEE Trans. Power Syst.*, vol. 22, no. 4, pp. 2003–2012, 2007.
- [83] F. A. Viawan and D. Karlsson, "Voltage and reactive power control in systems with synchronous machine-based distributed generation," *IEEE Trans. Power Deliv.*, vol. 23, no. 2, pp. 1079–1087, Apr. 2008.
- [84] X. Liu, A. Aichhorn, L. Liu, and H. Li, "Coordinated control of distributed energy storage system with tap changer transformers for voltage rise mitigation under high photovoltaic penetration," *IEEE Trans. Smart Grid*, vol. 3, no. 2, pp. 897–906, 2012.

- [85] J. W. Lamont and J. Fu, "Cost analysis of reactive power support," *IEEE Trans. Power Syst.*, vol. 14, no. 3, pp. 890–898, 1999.
- [86] D. J. Rogers and T. C. Green, "An active-shunt diverter for onload tap changers," *IEEE Trans. Power Deliv.*, vol. 28, no. 2, pp. 649–657, 2013.
- [87] C. L. Masters, "Voltage rise: the big issue when connecting embedded generation to long 11 kV overhead lines," *Power Eng. J.*, vol. 16, no. 1, pp. 5–12, 2002.
- [88] J.-C. Kim, S.-M. Cho, and H.-S. Shin, "Advanced power distribution system configuration for smart grid," *IEEE Trans. Smart Grid*, vol. 4, no. 1, pp. 353–358, 2013.
- [89] J. M. Bloemink and T. C. Green, "Benefits of distribution-level power electronics for supporting distributed generation growth," *IEEE Trans. Power Deliv.*, vol. 28, no. 2, pp. 911–919, 2013.
- [90] E. Demirok, P. C. González, K. H. B. Frederiksen, D. Sera, P. Rodriguez, and R. Teodorescu, "Local reactive power control methods for overvoltage prevention of distributed solar inverters in low-voltage grids," *IEEE J. Photovoltaics*, vol. 1, no. 2, pp. 174–182, Oct. 2011.
- [91] R. Tonkoski, L. A. C. Lopes, and T. H. M. El-Fouly, "Coordinated active power curtailment of grid connected PV inverters for overvoltage prevention," *IEEE Trans. Sustain. Energy*, vol. 2, no. 2, pp. 139–147, Apr. 2011.
- [92] S. X. Chen, Y. S. F. Eddy, H. B. Gooi, M. Q. Wang, and S. F. Lu, "A centralized reactive power compensation system for LV distribution networks," *IEEE Trans. Power Syst.*, vol. 30, no. 1, pp. 274–284, 2015.
- [93] Y. Yang, H. Li, A. Aichhorn, J. Zheng, and M. Greenleaf, "Sizing strategy of distributed battery storage system with high penetration of photovoltaic for voltage regulation and peak load shaving," *IEEE Trans. Smart Grid*, vol. 5, no. 2, pp. 982–991, 2014.
- [94] A. Sangwongwanich, Y. Yang, D. Sera, and F. Blaabjerg, "Lifetime evaluation of grid-connected PV inverters considering panel degradation rates and installation sites," *IEEE Trans. Power Electron.*, vol. 33, no. 2, pp. 1225–1236, Feb. 2018.

- [95] M. E. Baran and F. F. Wu, "Network reconfiguration in distribution systems for loss reduction and load balancing," *IEEE Trans. Power Deliv.*, vol. 4, no. 2, pp. 1401–1407, 1989.
- [96] A. Alkuhayli, F. Hafiz, and I. Husain, "Volt/Var control in distribution networks with high penetration of PV considering inverter utilization," in *2017 IEEE Power & Energy Society General Meeting*, 2017, pp. 1–5.
- [97] J. Kennedy and R. Eberhart, "Particle swarm optimization," *Neural Networks, 1995. Proceedings., IEEE Int. Conf.*, vol. 4, pp. 1942–1948 vol.4, 1995.
- [98] S. Frank, I. Steponavice, and S. Rebennack, "Optimal power flow: A bibliographic survey II non-deterministic and hybrid methods," *Energy Syst.*, vol. 3, no. 3, pp. 259–289, 2012.
- [99] F. Cingoz, A. Elrayyah, and Y. Sozer, "Optimized settings of droop parameters using stochastic load modeling for effective DC microgrids operation," *IEEE Trans. Ind. Appl.*, vol. 53, no. 2, pp. 1358–1371, Mar. 2017.
- [100] J. G. Vlachogiannis and K. Y. Lee, "A comparative study on particle swarm optimization for optimal steady-state performance of power systems," *IEEE Trans. Power Syst.*, vol. 21, no. 4, pp. 1718–1728, 2006.
- [101] K. Prakash and M. Sydulu, "Particle swarm optimization based capacitor placement on radial distribution systems," in *2007 IEEE Power Engineering Society General Meeting*, 2007, pp. 1–5.
- [102] "U.S. Department of Energy open data." [Online]. Available: <https://openei.org/doi-10.2172/1120900>. [Accessed: 31-Dec-2017].
- [103] J. Tukey, "Mathematics and the picturing of data," *Proc. Int. Congr. Math.*, pp. 523–532, 1975.
- [104] D.-L. Duan, X.-D. Ling, X.-Y. Wu, and B. Zhong, "Reconfiguration of distribution network for loss reduction and reliability improvement based on an enhanced genetic algorithm," *Int. J. Electr. Power Energy Syst.*, vol. 64, pp. 88–95, Jan. 2015.

- [105] H. Xing and X. Sun, "Distributed Generation Locating and Sizing in Active Distribution Network Considering Network Reconfiguration," *IEEE Access*, vol. 5, pp. 14768–14774, 2017.
- [106] J. M. Bloemink and T. C. Green, "Increasing distributed generation penetration using soft normally-open points," in *IEEE PES General Meeting*, 2010, pp. 1–8.
- [107] M. Dzamarija and A. Keane, "Autonomous curtailment control in distributed generation planning," *IEEE Trans. Smart Grid*, vol. 7, no. 3, pp. 1337–1345, May 2016.
- [108] A. R. Di Fazio, G. Fusco, and M. Russo, "Decentralized control of distributed generation for voltage profile optimization in smart feeders," *IEEE Trans. Smart Grid*, vol. 4, no. 3, pp. 1586–1596, Sep. 2013.
- [109] V. Calderaro, G. Conio, V. Galdi, G. Massa, and A. Piccolo, "Optimal decentralized voltage control for distribution systems with inverter-based distributed generators," *IEEE Trans. Power Syst.*, vol. 29, no. 1, pp. 230–241, Jan. 2014.
- [110] Y. Li, Z. Xu, J. Zhang, and K. Meng, "Variable droop voltage control for wind farm," *IEEE Trans. Sustain. Energy*, pp. 1–1, 2017.
- [111] Y. Han, H. Li, P. Shen, E. A. A. Coelho, and J. M. Guerrero, "Review of active and reactive power sharing strategies in hierarchical controlled microgrids," *IEEE Trans. Power Electron.*, vol. 32, no. 3, pp. 2427–2451, Mar. 2017.
- [112] H. Mahmood, D. Michaelson, and J. Jiang, "Reactive power sharing in islanded microgrids using adaptive voltage droop control," *IEEE Trans. Smart Grid*, vol. 6, no. 6, pp. 3052–3060, Nov. 2015.
- [113] V. Nasirian, Q. Shafiee, J. M. Guerrero, F. L. Lewis, and A. Davoudi, "Droop-free distributed control for AC microgrids," *IEEE Trans. Power Electron.*, vol. 31, no. 2, pp. 1600–1617, Feb. 2016.
- [114] Y. Mohamed and E. F. El-Saadany, "Adaptive decentralized droop controller to preserve power sharing stability of paralleled inverters in distributed generation microgrids," *IEEE Trans. Power Electron.*, vol. 23, no. 6, pp. 2806–2816, Nov. 2008.

- [115] E. Demirok, D. Sera, R. Teodorescu, P. Rodriguez, and U. Borup, "Evaluation of the voltage support strategies for the low voltage grid connected PV generators," in *2010 IEEE Energy Conversion Congress and Exposition*, 2010, pp. 710–717.
- [116] A. Bonfiglio, M. Brignone, F. Delfino, and R. Procopio, "Optimal control and operation of grid-connected photovoltaic production units for voltage support in medium-voltage networks," *IEEE Trans. Sustain. Energy*, vol. 5, no. 1, pp. 254–263, Jan. 2014.
- [117] T. Ding, C. Li, Y. Yang, J. Jiang, Z. Bie, and F. Blaabjerg, "A two-stage robust optimization for centralized-optimal dispatch of photovoltaic inverters in active distribution networks," *IEEE Trans. Sustain. Energy*, vol. 8, no. 2, pp. 744–754, Apr. 2017.
- [118] Z. Ziadi *et al.*, "Optimal voltage control using inverters interfaced with PV systems considering forecast error in a distribution system," *IEEE Trans. Sustain. Energy*, vol. 5, no. 2, pp. 682–690, Apr. 2014.
- [119] S. Weckx, C. Gonzalez, and J. Driesen, "Combined central and local active and reactive power control of PV inverters," *IEEE Trans. Sustain. Energy*, vol. 5, no. 3, pp. 776–784, Jul. 2014.
- [120] H. Soleimani Bidgoli and T. H. Van Cutsem, "Combined local and centralized voltage control in active distribution networks," *IEEE Trans. Power Syst.*, vol. 8950, no. c, pp. 1–10, 2017.
- [121] Y. Chistyakov, E. Kholodova, K. Natreba, A. Szabo, and M. Metzger, "Combined central and local control of reactive power in electrical grids with distributed generation," *2012 IEEE Int. Energy Conf. Exhib. ENERGYCON 2012*, pp. 325–330, 2012.
- [122] S. Weckx and J. Driesen, "Optimal local reactive power control by PV inverters," *IEEE Trans. Sustain. Energy*, vol. 7, no. 4, pp. 1624–1633, Oct. 2016.
- [123] M. E. Baran and I. M. El-Markabi, "A multiagent-based dispatching scheme for distributed generators for voltage support on distribution feeders," *IEEE Trans. Power Syst.*, vol. 22, no. 1, pp. 52–59, Feb. 2007.

- [124] M. Brenna, E. De Berardinis, F. Foiadelli, G. Sapienza, and D. Zaninelli, "Voltage control in smart grids: An approach based on sensitivity theory," *J. Electromagn. Anal. Appl.*, vol. 2, pp. 467–474, 2010.
- [125] M. Brenna *et al.*, "Automatic distributed voltage control algorithm in smart grids applications," *IEEE Trans. Smart Grid*, vol. 4, no. 2, pp. 877–885, Jun. 2013.
- [126] A. A. Alkuhayli, S. Raghavan, and B. H. Chowdhury, "Reliability evaluation of distribution systems containing renewable distributed generations," in *2012 North American Power Symposium (NAPS)*, 2012, pp. 1–6.
- [127] T. Niknam, M. Zare, and J. Aghaei, "Scenario-based multiobjective volt/var control in distribution networks including renewable energy sources," *IEEE Trans. Power Deliv.*, vol. 27, no. 4, pp. 2004–2019, Oct. 2012.
- [128] W. Römisch, "Scenario reduction techniques in stochastic programming," in *Stochastic Algorithms: Foundations and Applications: 5th International Symposium, SAGA 2009, Sapporo, Japan, October 26-28, 2009. Proceedings*, O. Watanabe and T. Zeugmann, Eds. Berlin, Heidelberg: Springer Berlin Heidelberg, 2009, pp. 1–14.
- [129] N. Gröwe-Kuska, H. Heitsch, and W. Römisch, "Scenario reduction and scenario tree construction for power management problems," in *2003 IEEE Bologna PowerTech - Conference Proceedings*, 2003, vol. 3, pp. 152–158.
- [130] W. L. de Oliveira, C. Sagastizábal, D. D. J. Penna, M. E. P. Maceira, and J. M. Damázio, "Optimal scenario tree reduction for stochastic streamflows in power generation planning problems," *Optim. Methods Softw.*, vol. 25, no. 6, pp. 917–936, Dec. 2010.
- [131] N. M. M. Razali and A. H. Hashim, "Backward reduction application for minimizing wind power scenarios in stochastic programming," in *2010 4th International Power Engineering and Optimization Conference (PEOCO)*, 2010, pp. 430–434.
- [132] J. Li, F. Lan, and H. Wei, "A scenario optimal reduction method for wind power time series," *IEEE Trans. Power Syst.*, vol. 31, no. 2, pp. 1657–1658, Mar. 2016.

- [133] Z. H. Rather, Z. Chen, P. Thogersen, and P. Lund, "Dynamic reactive power compensation of large-scale wind integrated power system," *IEEE Trans. Power Syst.*, vol. 30, no. 5, pp. 2516–2526, 2014.
- [134] P. Kundur, *Power System Stability and Control*, vol. 23. 2006.
- [135] A. M. Abed, "WSCC voltage stability criteria, undervoltage load shedding strategy, and reactive power reserve monitoring methodology," in *1999 IEEE Power Engineering Society Summer Meeting. Conference Proceedings*, vol. 1, pp. 191–197.
- [136] Western Electric Coordinating Council, "Guide to WECC/NERC Planning Standards I.D: Voltage Support and Reactive Power," 2006.
- [137] B. H. Chowdhury and C. W. Taylor, "Voltage stability analysis : V – Q power flow simulation versus dynamic simulation," *IEEE Trans. Power Syst.*, vol. 15, no. 4, pp. 1354–1359, 2000.
- [138] F. Dong, B. H. Chowdhury, M. L. Crow, and L. Acar, "Improving voltage stability by reactive power reserve management," *IEEE Trans. Power Syst.*, vol. 20, no. 1, pp. 338–345, 2005.
- [139] D. Marujo, A. C. Z. De Souza, B. I. L. Lopes, M. V. Santos, and K. L. Lo, "On control actions effects by using QV curves," *IEEE Trans. Power Syst.*, vol. 30, no. 3, pp. 1298–1305, 2015.
- [140] C. Vournas, C. Lambrou, I. Anagnostopoulos, G. Christoforidis, and J. Kabouris, "Distributed reactive support and voltage stability limits: The example of Peloponnese in the Hellenic interconnected system," in *2015 IEEE Power & Energy Society General Meeting*, 2015, pp. 1–5.
- [141] P. Kundur *et al.*, "Definition and classification of power system stability," *IEEE Trans. Power Syst.*, vol. 19, pp. 1387–1401, 2004.
- [142] C. Vournas and M. Karystianos, "Load Tap Changers in Emergency and Preventive Voltage Stability Control," *IEEE Trans. Power Syst.*, vol. 19, no. 1, pp. 492–498, Feb. 2004.

- [143] *PSS®E 34 PROGRAM APPLICATION GUIDE*. Siemens Industry, Inc., 2015.
- [144] WECC Renewable Energy Modeling Task Force, *WECC Guide for Representation of Photovoltaic Systems In Large-Scale Load Flow Simulations*. 2010.
- [145] T. V. Cutsem and C. Vournas, *Voltage stability of electric power systems*. Springer, 1998.
- [146] D. Chatterjee, J. Webb, Q. Gao, M. Y. Vaiman, M. M. Vaiman, and M. Povolotskiy, “N-1-1 AC contingency analysis as a part of NERC compliance studies at midwest ISO,” in *IEEE PES T&D 2010*, 2010, pp. 1–7.
- [147] IEEE PES Task Force, “Test Systems for Voltage Stability Analysis and Security Assessment,” 2015.
- [148] C. W. Taylor, *Power System Voltage Stability*. McGraw-Hill, 1994.
- [149] “Reliability Data for FGH20N60UFDTU.” [Online]. Available: <http://www.onsemi.com/PowerSolutions/reliability.do?device=FGH20N60UFD> [Accessed: 20-Jan-2018].
- [150] “Quality & Reliability Handbook.” [Online]. Available: <https://www.onsemi.com/pub/Collateral/HBD851-D.pdf> [Accessed: 20-Jan-2018].